A Measurement of Beauty Production in High–Energy Positron–Proton Scattering

Dissertation

zur

Erlangung der naturwissenschaftlichen Doktorwürde

(Dr. sc. nat.)

vorgelegt der

Mathematisch-naturwissenschaftlichen Fakultät

der

Universität Zürich

von

Jürgen Kroseberg

aus

Deutschland

Begutachtet von

Prof. Dr. Peter Truöl

Dr. Felix Sefkow

Zürich 2002

Die vorliegende Arbeit wurde von der Mathematisch-naturwissenschaftlichen Fakultät der Universität Zürich auf Antrag von Prof. Dr. Peter Truöl und Prof. Dr. Ulrich Straumann als Dissertation angenommen.

Abstract

A measurement of open beauty production in positron–proton scattering at a centre–of–mass energy of 300 GeV is presented. The data were recorded with the H1 detector at the HERA collider and correspond to an integrated luminosity of 11 pb^{-1}. Beauty–flavoured hadrons are observed through their semi–muonic decay. The signal contribution in the selected data is extracted on a statistical basis from the distributions of the muon impact parameter and of the transverse momentum of the muon relative to an associated jet. Cross sections are determined for muon polar angles $35^\circ < \theta^\mu < 130^\circ$ and transverse momenta $p_t^\mu > 2$ GeV in the kinematic regions of photoproduction ($Q^2 < 1$ GeV^2, $0.1 < y < 0.8$) and deep inelastic scattering (2 GeV$^2 < Q^2 < 100$ GeV^2, $0.05 < y < 0.7$). This measurement is the first at HERA to apply an impact parameter technique, thus making use of the beauty lifetime signature. The method is established in the photoproduction region and then used to measure beauty production in the previously unaccessed DIS regime. The measured cross sections are found to be above NLO QCD predictions.

Zusammenfassung

Die vorliegende Arbeit beschreibt eine Messung von Beauty–Produktion in Positron–Proton–Streuprozessen bei einer Schwerpunktsenergie von 300 GeV. Die verwendeten Daten wurden mit dem H1–Detektor am Speicherring HERA aufgezeichnet und entsprechen einer integrierten Luminosität von 11 pb^{-1}. Beauty–Hadronen werden im semi–myonischen Zerfallskanal nachgewiesen. Der Signalanteil im selektierten Datensatz wird auf statistischer Basis aus Spektren des Myon–Impaktparameters und des Myon–Transversalimpulses relativ zu einem assoziierten Jet bestimmt. Für Myon–Polarwinkel $35^\circ < \theta^\mu < 130^\circ$ und Myon–Transversalimpulse $p_t^\mu > 2$ GeV werden Wirkungsquerschnitte in den kinematischen Regionen der Photoproduktion ($Q^2 < 1$ GeV^2, $0.1 < y < 0.8$) und der tiefunelastischen Streuung (2 GeV$^2 < Q^2 < 100$ GeV^2, $0.05 < y < 0.7$) gemessen. Die Impaktparametermethode, die hier erstmals bei HERA zur Anwendung kommt, wird zunächst in der Photoproduktionsanalyse etabliert und nachfolgend für die erste Messung von Beauty–Produktion in tiefunelastischer Streuung benutzt. Die gemessenen Wirkungsquerschnitte liegen oberhalb der Vorhersagen von QCD–Rechnungen in nächstführender Ordnung.

Contents

Introduction

In the Standard Model of particle physics, the fundamental constituents of matter are *quarks* and *leptons*. Whereas leptons, e.g. electrons e and muons μ, can be observed experimentally as free particles, quarks are considered to be confined by a strong force within composite *hadrons*, e.g. protons p. This *strong interaction* is described in *quantum chromodynamics* (QCD) as a coupling of massless *gluons* to colour charges carried by the quarks and the gluons themselves. Perturbative QCD calculations are expected to be reliable if a hard scale is present in the process, for example if the masses of the interacting quarks are large. Measuring the production of heavy quarks is, therefore, an excellent testing ground for the theoretical understanding of the strong interaction.

At the ep collider HERA, where the measurement presented in this thesis was performed, *heavy flavour production* refers to processes which involve hadrons containing charm and beauty quarks. The experimental study of these processes provides valuable information on the mechanisms of the quark–level subprocesses underlying ep interactions as in the *hadronisation* the heavy hadrons are expected to take over a large part of the momentum of the original heavy quarks.

While present QCD calculations provide an acceptable description of charm production, the first beauty production measurement at HERA, using data recorded with the H1 detector in 1996, yielded a cross section significantly above the theoretical expectation. Similar discrepancies between data and QCD predictions have been observed in proton–antiproton and, more recently, in photon–photon interactions. This is rather surprising because the beauty quark is considerably heavier than the charm quark and perturbative QCD calculations of beauty production are thus expected to be even more reliable than in the charm case.

The aim of the work presented in this thesis is to further investigate beauty production at HERA using new data and improved experimental tools which have become available since the first measurement. Such measurements are experimentally challenging because at HERA energies beauty production is heavily suppressed, the cross section being two and three orders of magnitude below charm and total cross sections respectively. Fortunately, there are two characteristic properties of beauty hadrons which can be used to enrich and extract the signal, namely the large mass and the long lifetime between production and decay.

This thesis presents a measurement of beauty production with subsequent semi–muonic decay in high–energy ep scattering based on data recorded with the H1 detector in 1997. The signal content of an inclusive muon sample is determined on a statistical basis using the shape of the distributions for two different beauty–sensitive observables: the transverse muon momentum relative to an associated hadronic jet, $p_t^{\rm rel}$, and the signed muon impact parameter δ. While $p_t^{\rm rel}$, which exploits the large beauty mass, was already used previously, this analysis is the first at HERA to apply an impact parameter technique thus making use of the beauty lifetime signature. The crucial experimental device for the impact parameter analysis is the H1 central silicon tracker (CST), which was fully commissioned early in 1997.

The beauty production cross section is measured in two different phase space regions, photoproduction (γp) and deep inelastic scattering (DIS) respectively. In photoproduction, the kinematic range is chosen according to the earlier analysis and the impact parameter is established as a new observable by measuring beauty production using only the δ spectrum. A combination of δ and $p_t^{\rm rel}$ results in an improved γp cross section measurement. Finally, this improved method is used to perform the first measurement of the beauty production cross section in DIS. Preliminary results from these measurements have already been presented to the public. This thesis presents an updated status of the analysis, including additional systematic studies.

The thesis is organised as follows: The first chapter discusses the theoretical concepts to describe high–energy ep collisions as well as the production and semi–muonic decay of beauty hadrons. This is followed in Chapter 2 by a brief description of the H1 detector at HERA. Chapter 3 provides a general overview of the analysis including a discussion of the expected experimental signature of semi–muonic beauty decays and potential background processes, the definition of observables and an outline of the analysis strategy. A thorough description of the event reconstruction and selection procedure is given in Chapter 4. The resulting event samples are used to measure the beauty production cross section in photoproduction and DIS, which is detailed in Chapter 5. Chapter 6 compares the measured cross sections to theoretical predictions and other experimental results. Conclusions and some comments on possible future steps to improve and extend the experimental information on beauty production at HERA are given in Chapter 7.

A Note on Units

In this thesis a system of natural units will be used in which

$$c = \hbar = 1 \quad ,$$

where c is the velocity of light and $\hbar = h/2\pi$, h denoting Planck's constant. In this convention, energy, mass, reciprocal length and reciprocal time are of the same dimension, and the electron Volt,

$$1 \text{ eV} \approx 1.6 \cdot 10^{-19} \text{ Nm} \quad ,$$

is chosen as the corresponding unit. Particle interaction cross sections are given in barn,

$$1 \text{ b} = 10^{-28} \text{ m}^2 \quad .$$

Chapter 1

Theoretical Framework

This chapter presents theoretical and phenomenological concepts to describe beauty production in positron–proton collisions and the semi–muonic decay of beauty–flavoured hadrons. Some basic features of the present model of particle physics, which is commonly referred to as the *Standard Model*, are sketched, putting emphasis on the theory of strong interactions. This is followed by an outline of the theoretical description of high–energy *ep* scattering processes. Finally, issues specific to beauty production and decay are discussed.

1.1 The Standard Model

In the framework of the Standard Model [1, 2, 3], the fundamental constituents of matter are spin-1/2 fermions (*leptons*, *quarks* and their anti–particles), which are grouped into three *generations*, see Table 1.1. In quantum field theories, the fermions are described as complex field quanta governed by a Lagrangian density. The requirement that certain transformations do not change the form of the Lagrangian (*gauge invariance*) implies the existence of additional fields. The corresponding quanta have spin 1 and are denoted *gauge bosons*.

generation	lepton	c_{em}	mass/MeV	quark	c_{em}	mass/GeV
1	e^-, e^+	∓ 1	0.511	u, $\bar{u}$	$\pm 2/3$	$(1.5 - 4.5) \cdot 10^{-3}$
	ν_e, $\bar{\nu}_e$	0	$< 3 \cdot 10^{-6}$	d, $\bar{d}$	$\mp 1/3$	$(5.0 - 8.5) \cdot 10^{-3}$
2	μ^-, μ^+	∓ 1	105.7	c, $\bar{c}$	$\pm 2/3$	$1.0 - 1.4$
	ν_μ, $\bar{\nu}_\mu$	0	< 0.19	s, $\bar{s}$	$\mp 1/3$	$0.08 - 0.16$
3	τ^-, τ^+	∓ 1	1777	t, $\bar{t}$	$\pm 2/3$	174.3 ± 5.1
	ν_τ, $\bar{\nu}_\tau$	0	< 18.2	b, $\bar{b}$	$\mp 1/3$	$4.0 - 4.5$

Table 1.1: *Fundamental fermions [4]. Here, c_{em} denotes the electromagnetic charge in units of the positron charge. For the definition of neutrino mass limits and quark masses see [4].*

Virtual gauge bosons mediate the fundamental particle interactions. An overview is given in Table 1.2.[1] The *electroweak interaction* is described by *quantum flavourdynamics* (QFD) as exchange of massless photons, which exclusively couple to particles with non–zero electromagnetic charge (*electromagnetic interaction*), and heavy bosons, Z and W, accounting for *weak interactions*. The *strong interaction* is mediated by massless *gluons* and the corresponding field theory is *quantum chromodynamics*. While all particles except gluons are subject to the electroweak interaction, only quarks and gluons participate in strong interactions.

Particle masses are generated through the coupling to an additional scalar field. The corresponding *Higgs boson*, however, has not been observed experimentally.

	strong interaction	electroweak interaction		
source	3 colour charges	electroweak hypercharge		
char. coupling	$\alpha_s(M_Z)$ $= 0.1172(20)$	$\alpha(0\ \mathrm{GeV}^2)$ $1/137.03599976(50)$	$G_F = G_F\,(\alpha, M_Z, M_W)$ $1.16639(1) \cdot 10^{-5}\ \mathrm{GeV}^{-2}$	
gauge bosons	8 gluons g	photon γ	Z	$W^{\pm}$
c_{em}	0	0	0	± 1
mass/GeV	0	$< 2 \cdot 10^{-25}$	91.1876(22)	80.423(39)

Table 1.2: *Fundamental interactions and gauge bosons [4]. The Fermi constant G_F is the effective coupling strength for W exchange for energies much below the W mass.*

1.2 Quantum Chromodynamics

Quantum chromodynamics (QCD)[2] is a non–Abelian renormalisable gauge theory describing the strong interaction as a coupling of gluons g to *colour charges* carried by the strongly interacting fermions (quarks q) and the gluons themselves. For a given quark flavour there are three different colour states and three corresponding anti–colour states. The eight gluons correspond to the linear independent colour–anticolour combinations. The underlying symmetry group is SU(3).

In *perturbative* QCD (pQCD), particle scattering cross sections are calculated as power series in the *strong coupling constant* α_s. Beyond leading order (LO), some of the corresponding Feynman graphs include internal quark and gluon *loops*. Two simple examples are given in Figure 1.1. The computation involves an integration over the entire phase space of virtual and real quarks and gluons and results in *ultraviolet divergences*, which correspond to infinite values of the momenta of the internal particles. In order to get meaningful results, these divergences have to be removed in a well–defined way. A first *regularisation* step effectively introduces an upper momentum cut–off in the integration.

[1] *Gravitation* is negligible at presently accessible energies due to the small particle masses.
[2] An introduction to QCD can be found, for example, in [5].

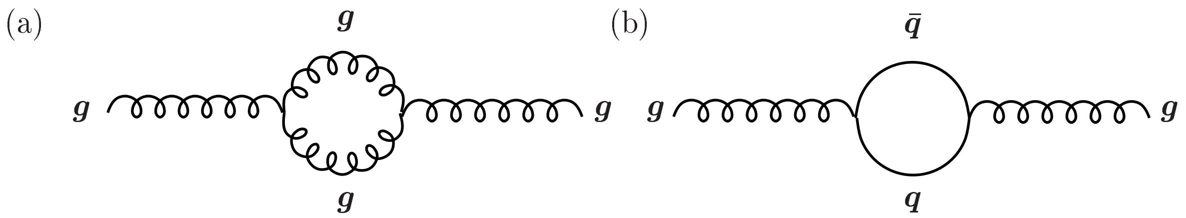

Figure 1.1: *One–loop corrections to the gluon propagator: (a) gluon and (b) quark loop.*

The resulting regularised integrals only contain simple pole divergences. These pole terms are subtracted in a second *renormalisation* step. This procedure introduces a *renormalisation scale* μ corresponding to the momentum at which the subtraction of the ultraviolet divergences is performed. The requirement that all measurable quantities (*observables*) are independent of the arbitrary choice[3] of μ, formally expressed by the *renormalisation group equation*, leads to an *effective coupling constant* $\alpha_s(\mu^2)$ with

$$\mu^2 \frac{\partial \alpha_s(\mu^2)}{\partial \mu^2} = \beta(\alpha_s) \quad . \tag{1.1}$$

Here, the *β-function* is a perturbative expansion in α_s describing the dependence of the strong coupling on the renormalisation scale (*running coupling*). The $\mathcal{O}(\alpha_s)$ solution is

$$\alpha_s(\mu^2) = \frac{12\pi}{(33 - 2n_f)\ln(\mu^2/\Lambda^2_{QCD})} \quad , \tag{1.2}$$

where Λ_{QCD} is a free parameter to be determined experimentally and n_f is the number of quark flavours with mass below μ. Thus, if α_s is known for a certain value of μ, the effective coupling can be obtained for any (sufficiently large) scale.

The strong coupling gets large for small μ values, which correspond to soft interactions and large distances. It should, therefore, be impossible to completely separate colour charged particles. Indeed, free quarks and gluons have never been observed experimentally. They are confined in colour–neutral *hadrons*. In the static quark model of hadrons, *baryons* are composed of three quarks (or three anti–quarks) and *mesons* consist of quark–antiquark pairs. The proton, for example, is a baryon with valence quark composition *uud*. It should be noted that in the absence of a hard scale pQCD is not applicable. As the predictive power of non–perturbative methods, e.g. *lattice QCD*, is still very limited, one presently relies to a large extend on phenomenological models. At large scales, however, α_s is small and perturbative methods can be applied. As $\alpha_s \to 0$ for $\mu \to \infty$, quarks can be treated as free particles in the asymptotic limit.

Thus, the scale dependence of the strong coupling constant implies *colour confinement* and *asymptotic freedom*. While asymptotic freedom has been strictly proven within QCD, colour confinement rests on less rigorous arguments.

[3]In practice, in order to obtain a stable perturbative expansion, μ needs to be chosen close to the physical scales characterising the process under study.

1.3 High–Energy *ep* Collisions

In a simple picture, positron–proton scattering processes[4]

$$ep \rightarrow lX \tag{1.3}$$

are described by the exchange of a single virtual gauge boson (γ, Z or W) as illustrated in Figure 1.2. Here X denotes the hadronic final state and l the scattered lepton. According to the boson charge one distinguishes *neutral current* (NC) processes, $ep \rightarrow eX$, and *charged current* (CC) interactions, $ep \rightarrow \nu_e X$.

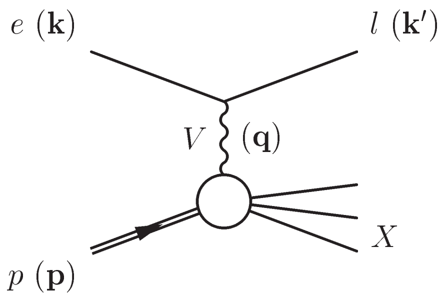

e :	positron, four–momentum $\mathbf{k}$
p :	proton, four–momentum $\mathbf{p}$
l :	scattered lepton (e or ν_e), four–momentum $\mathbf{k}'$
V :	exchange boson (γ, Z or W), four–momentum $\mathbf{q}$
X :	hadronic final state

Figure 1.2: *Positron–proton scattering in the single boson exchange picture. In NC processes, the exchanged boson V is a photon γ or a Z boson and the scattered lepton l is a positron. In the CC case, a W boson is exchanged resulting in an outgoing anti–neutrino.*

The transfered momentum is given by the gauge boson's *virtuality*

$$Q^2 = -\mathbf{q}^2 = -(\mathbf{k} - \mathbf{k}')^2 \;\;,\;\; Q^2 \geq 0 \;\;, \tag{1.4}$$

and

$$s = (\mathbf{p} + \mathbf{k})^2 \tag{1.5}$$

is the squared centre–of–mass energy of the reaction. The quantity

$$y = \frac{\mathbf{p} \cdot \mathbf{q}}{\mathbf{p} \cdot \mathbf{k}} \;\;,\;\; 0 \leq y \leq 1 \;\;, \tag{1.6}$$

describes the relative energy transfer at the positron–boson vertex in the proton rest frame. Further, one defines the *Bjørken scaling variable* as

$$x = \frac{Q^2}{2\,\mathbf{p} \cdot \mathbf{q}} \;\;,\;\; 0 \leq x \leq 1 \;\;. \tag{1.7}$$

[4]In the following, positrons and anti–neutrinos are referred to as e and ν_e respectively in order to simplify the notation.

Within the quark–parton model (see below) the Bjørken scaling variable x is interpreted as the fraction of the proton's momentum carried by the interacting parton.

If the centre–of–mass energy $\sqrt{s}$ is much larger than the masses of the interacting particles, these Lorentz invariants, which are also referred to as *kinematic variables*, fulfil

$$Q^2 = xys \quad . \tag{1.8}$$

Defining a Cartesian laboratory coordinate system by

$$\begin{aligned} &\mathbf{k} = (E_e, 0, 0, -E_e)\,, \\ &\mathbf{k}' = (E'_e, E'_e \sin\theta_e \cos\varphi_e, E'_e \sin\theta_e \sin\varphi_e, -E'_e \cos\theta_e) \quad \text{and} \\ &\mathbf{p} = (E_p, 0, 0, E_p) \quad , \end{aligned} \tag{1.9}$$

and keeping the above approximations, the kinematic variables can be calculated from particle energies and angles via [6]

$$\begin{aligned} Q^2 &= 2E_e E'_e(1+\cos\theta_e) \quad , \quad s = 4E_p E_e, \\ y &= 1 - \tfrac{E'_e}{2E_e}(1-\cos\theta_e) \quad , \quad x = \tfrac{Q^2}{4yE_eE_p}. \end{aligned} \tag{1.10}$$

Collisions at Q^2 above a few GeV are termed *deep inelastic scattering* (DIS). In the phase space region of very small momentum transfer ($Q^2 \approx 0$) the *ep* interaction is mediated by quasi–real photons. Consequently, this class of processes is referred to as *photoproduction* (γp).

1.3.1 DIS Processes and Proton Structure

As has been discussed in Section 1.2, within the Standard Model the proton is not considered an elementary particle. A quantitative model of the proton substructure is, therefore, a necessary ingredient to the theoretical treatment of *ep* processes. On the other hand, the experimental study of deep inelastic *ep* scattering provides equal insight into proton structure.

Inclusive DIS Cross Sections and Proton Structure Functions

In the *Born approximation* [7] the dependence of the inclusive positron–proton NC DIS cross section on the kinematic variables x and Q^2 can be expressed in the following form:[5]

$$\frac{d^2\sigma^{NC}}{dx\,dQ^2} = \frac{2\pi\alpha^2}{xQ^4}\left[\tilde{F}_2^p\left(1+(1-y)^2\right) + x\tilde{F}_3^p\left(1-(1-y)^2\right) + y^2\tilde{F}_L^p\right] \quad . \tag{1.11}$$

$\tilde{F}_2^p(x,Q^2)$, $\tilde{F}_3^p(x,Q^2)$ and $\tilde{F}_L^p(x,Q^2)$ are *generalised structure functions*, which include coupling constants, propagator terms and *structure functions* for γ exchange, Z exchange

[5]similar expressions can be derived for the CC case.

and γZ interference respectively. The structure functions in general depend on both x and Q^2 and reflect the fact that the proton does not enter the interaction as a point–like particle but as a composite object.

Z exchange gives rise to terms proportional to $Q^2/\left(Q^2+M_Z^2\right)$. For $Q^2 \ll M_Z^2$, therefore, NC ep interactions are dominantly photon mediated. In the approximation of pure photon exchange the contribution from $x\tilde{F}_3^p$ vanishes and $\tilde{F}_2^p(x,Q^2)$ reduces to an electromagnetic structure function $F_2^p(x,Q^2)$. If the small contributions from longitudinally polarised photons are also neglected ($y^2\tilde{F}_L^p = 0$), the double differential NC cross section becomes

$$\frac{d^2\sigma^{NC}}{dx\,dQ^2} = \frac{2\pi\alpha^2}{xQ^4}\left(1+(1-y)^2\right)F_2^p(x,Q^2) \quad . \tag{1.12}$$

Quark–Parton Model

If ep DIS processes are considered in a reference frame where the (three–)momentum of the proton is large, $|\vec{p}\,|^2 \gg m_p^2$, the proton can, to good approximation, be described as a parallel stream of independent constituents (*partons*). Identifying these partons with quarks results in the *quark–parton model* (QPM) [8, 9]. In the QPM, deep inelastic scattering ep processes are interpreted as elastic positron scattering from a single quark. The other partons, which form the *proton remnant*, do not participate in the hard interaction and therefore are referred to as *spectator partons*. The cross section for the ep process is obtained by calculating perturbatively the transition amplitudes for the elastic scattering of the positron from free quarks and summing incoherently the contributions from all quark flavours. The structure function F_2^p reads

$$F_2^p(x,Q^2) = x\sum_q c_q^2\left(f_q^p(x,Q^2)+f_{\bar{q}}^p(x,Q^2)\right) \quad . \tag{1.13}$$

The sum runs over all quark flavours q; c_q are the quark charges, and the functions f_q^p ($f_{\bar{q}}^p$) describe the quark (anti–quark) densities in the proton. If only the *valence quarks* u and d, which build up the proton in the static quark model of hadrons, are taken into account, F_2^p depends only on x. This prediction is known as *scaling*. However, from the observation of *scaling violation* in experimental F_2^p data it follows that also gluons and gluon–induced pairs of quarks and anti–quarks have to be considered as proton constituents.

Factorisation Theorem and Parton Density Functions

The concept of proton parton densities introduced in the previous section is theoretically justified by the *factorisation theorem* which states that the inclusive description of the ep process can be divided into two independent parts: a *short distance part*, which describes the interaction of high–energy partons (*hard subprocess*) and can be calculated within pQCD, and a *long distance part* corresponding to low energy processes not accessible by perturbative calculations.

In this framework, the proton structure function F_2^p takes the form of a convolution of perturbatively calculable *coefficient functions* C_2^i and *parton density functions* (PDFs)

$f_i^p(\xi)$ which give the probability of finding a parton of type i carrying a fraction ξ of the proton's (longitudinal) momentum:

$$F_2^p = \sum_{i=q,\bar{q},g} \int_x^1 d\xi C_2^i \left(\frac{x}{\xi}, \frac{Q^2}{\mu^2}, \frac{\mu_f^2}{\mu^2}, \alpha_s(\mu^2) \right) f_i^p(\xi, \mu_f, \mu) \tag{1.14}$$

Here, μ denotes the renormalisation scale (see Section 1.2). The factorisation procedure introduces an *factorisation scale* μ_F defining the boundary between the perturbative and non–perturbative regions. Formally, the μ_F dependence arises from the absorption of collinear divergences into the PDFs according to a certain *factorisation scheme*.

The form of the resulting re–defined parton densities is not independent of the used scheme. However, for a given choice of factorisation scheme and scale, the proton PDFs are considered *universal*, i.e. independent of the actual reaction the proton takes part in.

Parton Evolution Models

Using the structure function (1.14), the inclusive DIS cross section σ_{ep} factorises into parton–level cross sections $\hat{\sigma}_{ei}$ and parton density functions f_i^p, symbolically:

$$\sigma_{ep} = \sum_{i=q,\bar{q},g} \left[\hat{\sigma}_{ei}(\mu_F) \otimes f_i^p(\mu_F) \right] \quad . \tag{1.15}$$

In contrast to the hard subprocess cross sections, which are accessible within pQCD, the PDFs cannot be calculated from first principles. However, as the observable cross section σ_{ep} must not depend on the unphysical parameter μ_F and the $\hat{\sigma}_{ei}$ are perturbatively calculable for different μ_F values, the dependence of the PDFs on the factorisation scale can also be studied within pQCD. The result are *parton evolution equations*, which can be used to extract the PDFs from experimental structure function data.

While the underlying concept is universal, in practical calculations approximations have to be applied, resulting in different *parton evolution models*, which are expected to be valid only in certain regions of phase space. For the discussion of examples it is useful to choose a combination of reference frame and gauge for which the individual contributions to $\hat{\sigma}$ can be represented by *ladder diagrams* formed from n parton emissions from partons with transverse momenta $k_{t,i}$ and longitudinal momenta x_i ($x_i > x_{i+1}$) as sketched in Figure 1.3. The transverse momenta of the emitted partons are labelled $p_{t,i}$, z_i denotes the longitudinal momentum fraction in the branching $(i-1) \rightarrow i$. The evaluation of these diagrams involves nested integrations over the internal momenta. The calculation simplifies considerably if a certain kinematical *ordering* of the emission processes is assumed.

In this analysis, two different parton evolution models are used:

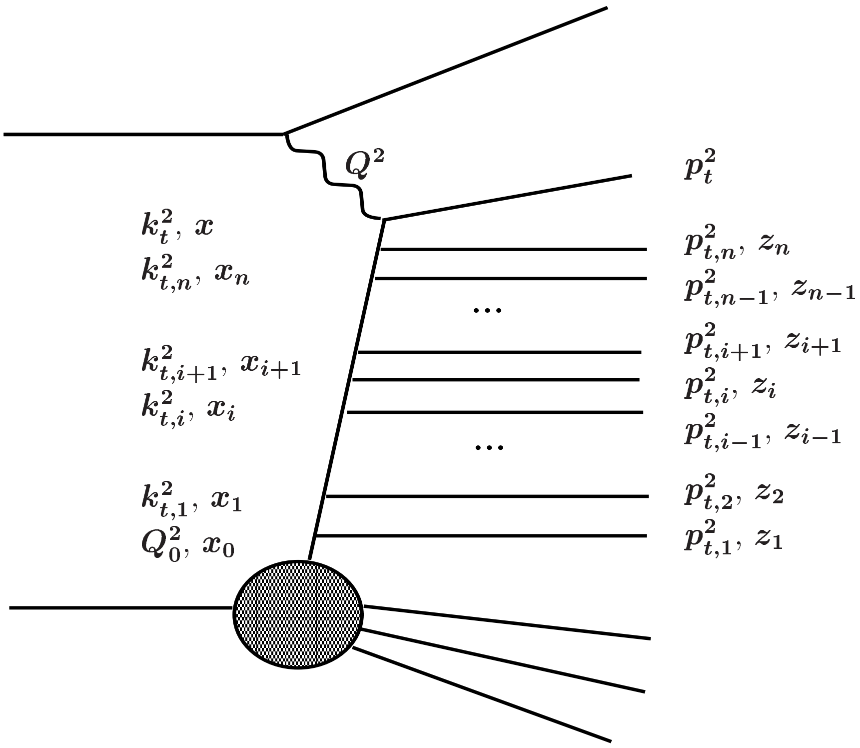

Figure 1.3: *Ladder diagram illustrating parton evolution.*

- *DGLAP* [10, 11, 12]: If *strong ordering* of the transverse momenta $k_{t,i}$ is assumed, i. e.

$$Q_O^2 \ll \cdots \ll k_{t,i} \ll k_{t,i+1} \ll \cdots \ll k_{t,n} \ll Q^2 \quad , \tag{1.16}$$

where Q_O^2 is a suitable chosen starting scale, the integration over the $k_{t,i}$ and x_i can be carried out. Considering all important diagrams up to $n \to \infty$ corresponds to summing expressions proportional to $(\alpha_s^2)^n(\ln(Q^2/Q_O^2))^n$. This *leading log approximation* (LLA) is expected to be valid in the region where Q^2 is large and x is not too small and therefore

$$\alpha_s^2(Q^2)\ln\frac{1}{x} \ll \alpha_s^2(Q^2)\ln\frac{Q^2}{Q_O^2} < 1 \quad . \tag{1.17}$$

In LLA, the dependence of the proton quark and gluon density functions $f_{q_i}^p$ and f_g^p on the factorisation scale (chosen as $\mu_F^2 = Q^2$) is given by the Dokshitzer–Gribov–Lipatov–Altarelli–Paresi (DGLAP) equations, which in leading order read

$$\begin{aligned}
\frac{df_{q_i}^p(x,Q^2)}{d\ln(Q^2)} &= \frac{\alpha_s(Q^2)}{2\pi}\int_x^1 \frac{d\xi}{\xi}\left[P_{qq}(\frac{x}{\xi})f_{q_i}^p(\xi,Q^2) + P_{qg}(\frac{x}{\xi})f_g^p(\xi,Q^2)\right] \\
\frac{df_g^p(x,Q^2)}{d\ln(Q^2)} &= \frac{\alpha_s(Q^2)}{2\pi}\int_x^1 \sum_i \frac{d\xi}{\xi}\left[P_{gq}(\frac{x}{\xi})f_{q_i}^p(\xi,Q^2) + P_{gg}(\frac{x}{\xi})f_g^p(\xi,Q^2)\right] \quad .
\end{aligned} \tag{1.18}$$

The perturbatively calculable *splitting functions* $P_{ab}(z)$ are related to the probability of a parton a emitting a parton b with a momentum fraction z.

- *CCFM* [13, 14, 15]: The more recent parton evolution model by Ciafaloni, Catani, Fiorani and Marchesini (CCFM) is based on gluon emission with ordering in the angles of the emitted gluons with respect to the incoming proton. Defining rescaled transverse momenta of the emitted gluons by

$$\vec{\zeta_i} = \frac{\vec{p}_{t,i}}{1 - z_i} \quad , \tag{1.19}$$

strong *angular ordering* translates into

$$Q_0 \ll \cdots \ll \zeta_i \ll \zeta_{i+1} \ll \cdots \ll \zeta_n \ll \bar{\zeta} \quad , \tag{1.20}$$

where $\zeta_i = |\vec{\zeta_i}|$. The additional scale $\bar{\zeta}$ is related to the maximum allowed emission angle. The CCFM equation describes the $\bar{\zeta}$ dependence of the *unintegrated gluon density* $\hat{f}_g^p(x, k_t, \bar{\zeta})$:

$$\bar{\zeta}^2 \frac{d}{d\bar{\zeta}} \frac{x\hat{f}_g^p(x, k_t^2, \bar{\zeta})}{\Delta_s(\bar{\zeta}, Q^0)} = \int_0^{2\pi} \frac{d\varphi}{2\pi} \int_x^1 dz \frac{\tilde{P}(z, \bar{\zeta}/z, k_t)}{\Delta_s(\bar{\zeta}, Q^0)} x' \hat{f}_g^p(x', k'^2_t, \bar{\zeta}) \quad , \tag{1.21}$$

where $x' = x/z$, $\vec{k}'_t = [(1-z)/z]\vec{\zeta} + \vec{k}_t$ and $\vec{\zeta}$ is at an azimuthal angle φ. In this particular form, the CCFM equation relates the values of the gluon density $\hat{f}_g^p$ at two different points in phase space connected by the emission of a gluon with momentum fraction $(1-z)$. $\tilde{P}(z, \bar{\zeta}/z, k_t)$ is the corresponding splitting function, $\Delta_s(\bar{\zeta}, Q^0)$ denotes the *Sudakov form factor* (see [16]).

The usual gluon density f_g^p can be obtained from $\hat{f}_g^p$ by integrating over k_t:

$$f_g^p(x, Q^2) = \frac{1}{x} \int_0^{Q^2} \frac{dk_t^2}{k_t^2} \hat{f}_g^p(x, k_t^2) \quad . \tag{1.22}$$

The CCFM evolution can be formulated also for quarks and is valid also for small x, at larger x giving predictions for inclusive proton structure similar to DGLAP.

The parton evolution equations can be used to extract the proton PDFs from experimental data. In the case of DGLAP, the x dependence of the PDFs is parametrised at a certain starting scale Q_0 (usually a few GeV). Using Equation (1.18), the PDFs are evolved into a Q^2 region, where the corresponding predictions for the structure functions can be compared to structure function data measured in DIS experiments. In an iterative fit procedure, which in general uses a combination of data from different processes and experiments, the best parameter values are determined.

As can be seen in Figure 1.4, DGLAP based next–to–leading order QCD fits are found to be in excellent agreement with inclusive F_2^p measurements at HERA. However, for some exclusive processes in certain regions of phase space the mechanisms modelled in CCFM might well be relevant for the description of the HERA data. This open question is studied in recent and ongoing analyses.

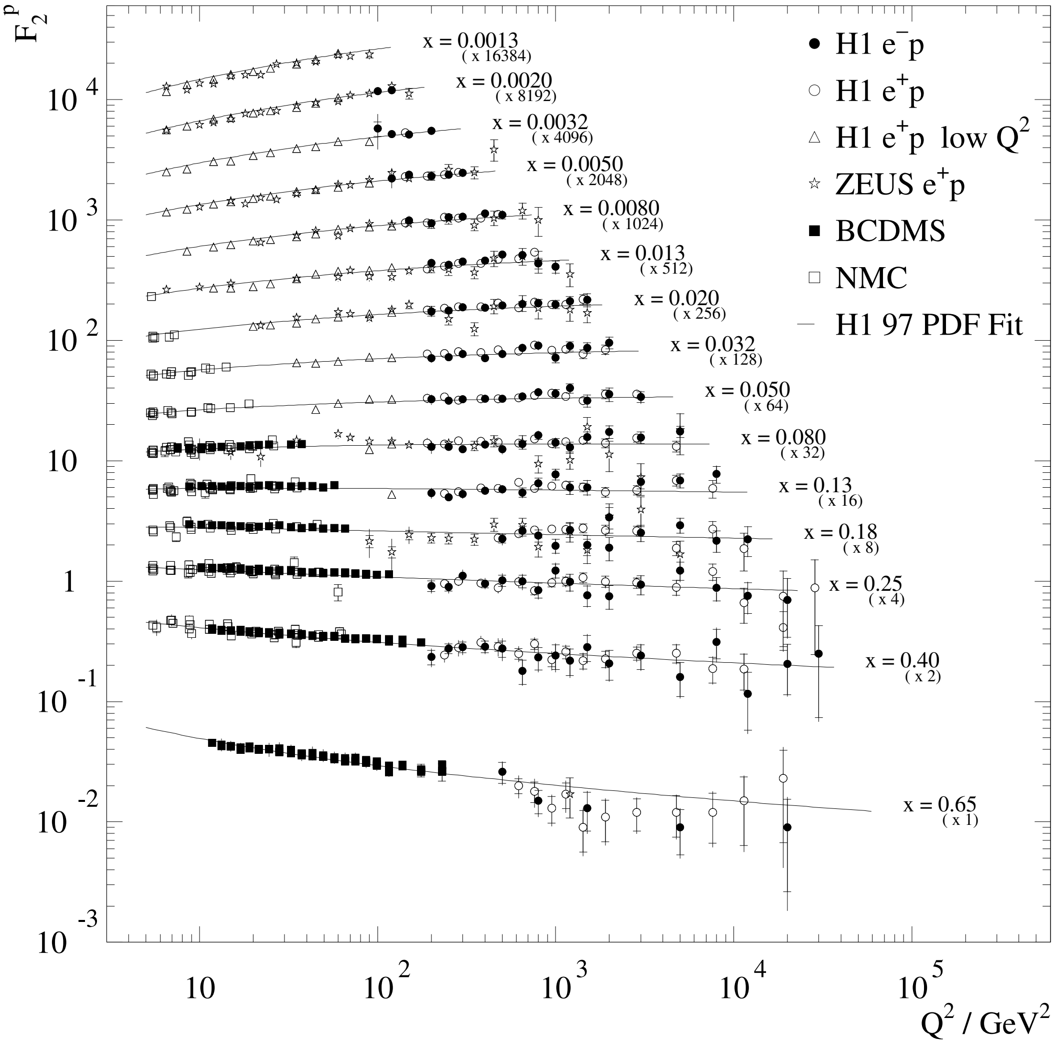

Figure 1.4: *Measured proton structure function $F_2(x, Q^2)$ as a function of Q^2 for different x, together with a DGLAP–based QCD fit. [17]*

1.3.2 Photoproduction Processes and Photon Structure

As the photon propagator enters as a factor $1/Q^4$ (cf. Equation 1.11), the inclusive ep cross section is dominated by photoproduction. In γp processes the positron is only slightly scattered out of its original direction. In the Cartesian laboratory coordinate frame (1.9), this corresponds to scattering angles θ_e close to 180° and the kinematic variable y is given to good approximation by $y = 1 - E'_e/E_e$. Alternatively, the interaction kinematics can be described using the photon–proton centre–of–mass energy $W = \sqrt{(\mathbf{q}+\mathbf{p})^2}$, which, neglecting positron and proton masses, is related to y via

$$W = \sqrt{ys - Q^2} \approx \sqrt{ys} \quad . \tag{1.23}$$

Referring to Equation (1.7), $Q^2 \rightarrow 0$ implies $x \rightarrow 0$. The Bjørken scaling variable, therefore, has no physical meaning in the photoproduction domain.

Weizsäcker–Williams Approximation

The Weizsäcker–Williams approximation (WWA) [18, 19] describes the photoproduction process as the interaction of a (quasi–)real photon with the proton. Neglecting the small contributions from longitudinal polarised photons, the differential cross section factorises into two contributions:

$$\frac{d^2\sigma^{PhPr}(y,Q^2)}{dy\,dQ^2} = P_{\gamma/e}(y,Q^2)\cdot\sigma_{\gamma p\to eX}(y) \quad . \tag{1.24}$$

Here, $\sigma_{\gamma p\to eX}$ denotes the cross section for the scattering of a real photon from a proton. The (extended) *Weizsäcker–Williams splitting function* [20]

$$P_{\gamma/e}(y,Q^2) = \frac{\alpha}{2\pi y Q^2}\left(1+(1-y)^2 - \frac{2m_e^2y^2}{Q^2}\right) \tag{1.25}$$

gives the probability that the positron (mass m_e) emits a photon with energy fraction y and virtuality Q^2.

Photon Structure

Despite its classification within the Standard Model as an elementary, colour–neutral particle, the photon can indirectly participate in strong interactions via a fluctuation into a $q\bar{q}$ pair. In this sense the photon shows partonic substructure, which is potentially relevant especially in the photoproduction domain.

Most of the experimental information on photon structure comes from studies of $\gamma\gamma$ processes in e^+e^- scattering. In the case that one of the photons is (quasi–)real and the other photon's virtuality Q^2 is large, the interaction can be treated as deep inelastic $e\gamma$ scattering. In analogy to ep DIS (see Section 1.3.1), one can define structure functions which relate the $e\gamma$ cross section to the parton content of the photon. For $x_\gamma y^2 \ll 1$ a single structure function F_2^γ dominates with (see Equation (1.12) for the ep case)

$$\frac{d^2\sigma^{e\gamma}}{dx_\gamma\,dQ^2} = \frac{2\pi\alpha^2}{x_\gamma Q^4}\left(1+(1-y)^2\right)F_2^\gamma(x_\gamma,Q^2) \quad , \tag{1.26}$$

Here, x_γ denotes the fraction of the photon's (longitudinal) momentum carried by the interacting parton.

Again, parton densities f_i^γ can be extracted from experimental structure function data using parton evolution equations. The LO DGLAP equations for the photon are

$$\begin{aligned}
\frac{df_{q_i}^\gamma(x,Q^2)}{d\ln(Q^2)} &= \frac{\alpha c_q^2}{2\pi}P_{\gamma q}(x_\gamma) + \frac{\alpha_s(Q^2)}{2\pi}\int_{x_\gamma}^1 \frac{d\xi}{\xi}\left[P_{qq}(\frac{x}{\xi})f_{q_i}^\gamma(\xi,Q^2) + P_{qg}(\frac{x}{\xi})f_g^\gamma(\xi,Q^2)\right] \\
\frac{df_g^\gamma(x,Q^2)}{d\ln(Q^2)} &= \frac{\alpha_s(Q^2)}{2\pi}\int_{x_\gamma}^1 \sum_i \frac{d\xi}{\xi}\left[P_{gq}(\frac{x}{\xi})f_{q_i}^\gamma(\xi,Q^2) + P_{gg}(\frac{x}{\xi})f_g^\gamma(\xi,Q^2)\right] \quad .
\end{aligned} \tag{1.27}$$

In contrast to the proton case, the equations for the quark densities are inhomogeneous due to an additional term $\sim P_{\gamma q}(x_\gamma) = x_\gamma^2 + (1 - x_\gamma)^2$ which accounts for the splitting of the photon into a $q\bar{q}$ pair and is sometimes referred to as the *point–like* part of the photon structure.

A different approach to the description of strong photon interactions is provided by the *vector meson dominance model* (VDM) [21, 22, 23]. Here, the photon is assumed to fluctuate into a vector meson V ($V = \rho,\omega,\varphi,\ldots$), i. e. a bound hadronic $q\bar{q}$ state carrying the same quantum numbers as the photon, which then interacts with a target particle. In this framework, the γp cross section takes the form of an incoherent sum over meson-proton cross sections σ_{Vp}:

$$\sigma_{\gamma p} = \sum_{V=\rho,\omega,\varphi,\ldots} \frac{\pi\alpha}{\Gamma_V^2}\sigma_{Vp}, \tag{1.28}$$

where the Γ_V are photon–meson coupling constants to be determined in independent experiments.

Parametrisations of the photon structure in general include both a VDM–like component and an *anomalous* part corresponding to interacting partons propagating without forming an hadronic state.

Resolved Photon Processes

Processes for which only a fraction $x_\gamma < 1$ of the photon's momentum enters the hard subprocess signal the partonic substructure of the photon and are, therefore, called *resolved photon interactions*, in contrast to *direct processes* where the photon interacts directly with the proton and consequently $x_\gamma = 1$.

1.4 Parton Hadronisation and Hadron Jets

In experiment free quarks or free gluons have never been observed. In the framework of QCD this is a consequence of colour confinement (see Section 1.2). Instead, the strongly interacting outgoing partons are detected only indirectly via colour–neutral hadrons resulting from *parton hadronisation* (also referred to as *fragmentation*). For a large variety of processes it is possible to translate certain results of perturbative fixed–order calculations into hadron level observables accessible by experiment, e.g. by applying *power corrections*. These models, however, in general fail to describe the detailed structure of the hadronic final state.

In an alternative approach, which forms the basis of *event generators* (see Section 1.7), the transition from partons to an observable hadronic final state is modelled explicitly. In a first step, starting from a partonic final state corresponding to a fixed order description of the hard subprocess, perturbatively calculable QCD processes lead to a production of additional partons (*parton cascades*). From these, hadrons are formed in a second non–perturbative phase, which is described by phenomenological *hadronisation* (or *fragmentation*) *models*.

Parton Cascades

In this analysis, the parton cascades are modelled as *parton showers* which approximate multiple emission processes by a series of successive parton splittings. The probability for each of these branching processes depends on the corresponding splitting function (see Section 1.3.1) and the virtuality of the initial parton. The *initial state parton shower* starts from a parton coming from the proton, which via emissions of time-like or real partons, evolves to increasingly negative virtuality and finally enters the hard subprocess.[6] Any outgoing parton with positive virtuality is a potential starting point for a time–like *final state parton shower*.

The cascade is stopped when the virtuality of the outgoing partons reaches a minimum value, which is usually chosen around 1 GeV. In the kinematic region below this scale pQCD becomes unreliable and non–perturbative phenomenological models have to be used.

Hadronisation Models

Currently there is no fundamental understanding of the mechanisms transforming partons into hadrons. Phenomenological hadronisation models are therefore used, which predict the hadronic final state on the basis of a given parton configuration. Two approaches are relevant for this analysis:

- *Independent fragmentation*: In this model, all outgoing partons hadronise independently, see Figure 1.5(a). *Fragmentation functions* $D_i^h(z)$ describe the transition probability from a parton i to a hadron h carrying a fraction z of the parton's longitudinal momentum. The distribution of the hadron's transverse momentum with respect to the original quark direction is assumed to be Gaussian. The additional quarks (anti–quarks) needed to form the hadron h are taken from $q\bar{q}$ pairs, with the remaining anti–quark (quark) continuing hadronisation. The branching is repeated until the available energy is used up.

- *String fragmentation*: In this model, $q\bar{q}$ pairs and the colour field between them form *strings*. Gluons are represented by kinks in the strings. If the potential energy stored in a string, which at large $q\bar{q}$ separation r rises proportional to r, becomes large enough it breaks up into two string pieces via the formation of a new $q\bar{q}$ pair, cf. Figure 1.5(b). When no energy for further $q\bar{q}$ production is left, the process stops and the resulting string fragments are combined into hadrons, again using a fragmentation function.

[6] In event generators the initial state parton shower is implemented in *backward evolution* starting from the hard subprocess and evolving towards the incoming proton.

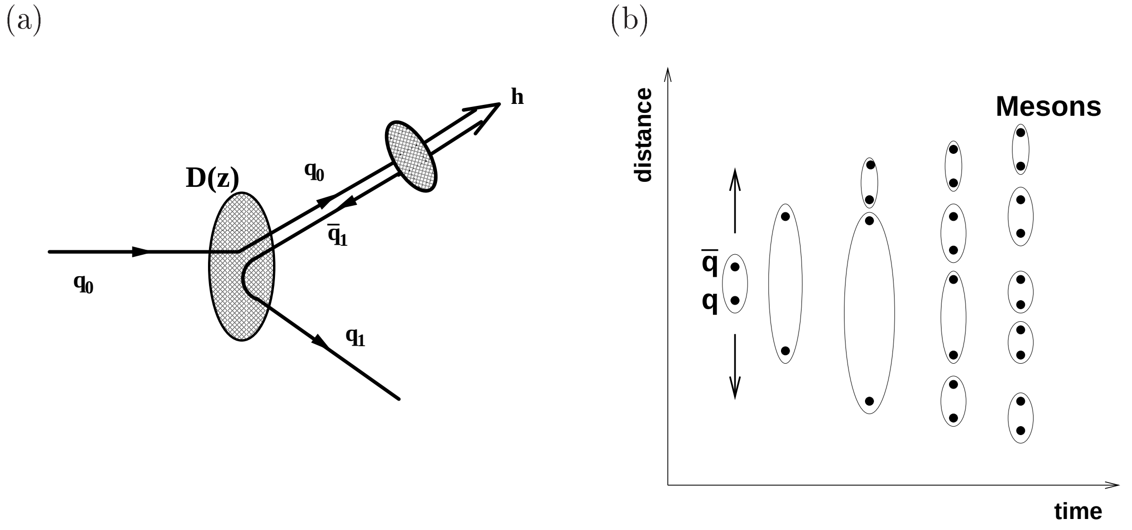

Figure 1.5: *Parton hadronisation in (a) independent fragmentation and (b) the cluster model.*

Jets

According to the above discussion on hadronisation, each strongly interacting final state parton from the hard subprocess produces a group of outgoing hadrons. In high–energy processes, where the momentum of the original parton is sufficiently high, these hadrons in general form a collimated *jet*, which is geometrically well–separated from the other final state particles.

Although a strict one–to–one correspondence of partons and jets is in general spoiled by higher order QCD processes connecting also particles originating from different partons, the jet topology is expected to reflect important properties of the underlying partonic process. In order to exploit this feature by using jet–based observables within a quantitative theory, it is necessary to have a well–defined procedure to group final state particles into jets (*jet algorithm*). In addition, a prescription (*recombination scheme*) has to be given to construct a jet momentum from the corresponding set of particle momenta.

Jets are not considered fundamental QCD objects and, obviously, the jet topology will depend on the construction method used. In order to be able to use jet observables for comparison with pQCD, certain theoretical aspects need to be considered. Results based on jet observables should be *collinear safe* and *infra–red safe*, i. e. not affected by collinear or soft parton radiation. The jet topology should be closely correlated to the partonic final state, and *hadronisation corrections* connecting observables on hadron level with corresponding parton level quantities are preferred to be small. Also, it is desirable not to destroy QCD factorisation. These requirements are met, for example, by the *longitudinally invariant k_t algorithm* [24], which is used in this analysis (see Section 4.5.2).

1.5 Beauty Production

All aspects which have been described up to this point are relevant for positron–proton scattering processes in general, irrespective of the actual final state configuration emerging from the *ep* interaction. Now, the discussion turns to issues specific to the production of beauty–flavoured particles.

Beauty and charm are commonly referred to as *heavy* flavours, because the b and c quark masses ($m_b \approx 4.5$ GeV and $m_c \approx 1.5$ GeV respectively) are considerably larger than the masses of the *light* quarks u, d and s, cf. Section 1.1.[7] This is reflected also in the relatively larger masses of charm and beauty hadrons (see below) and sets heavy flavour production apart from other processes.

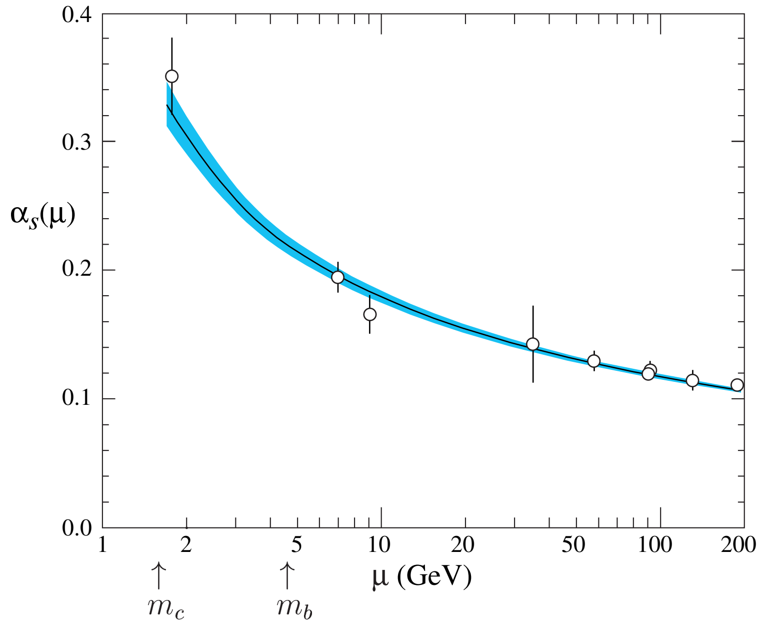

Figure 1.6: *The scale dependence of the strong coupling constant α_s [4]. The data are obtained from measurements of particle decay widths (τ, Υ, Z) as well as event shape analyses in e^+e^- collisions at different energies. For details see [4] and references therein.*

Heavy flavour production is considered an excellent testing ground for quantum chromodynamics. Even for soft processes, i. e. in the absence of any other hard scale, the heavy quark mass makes it possible to use perturbative methods. Due to the large b mass, pQCD calculations are expected to be particularly reliable in the beauty case. This is illustrated by the scale dependence of the effective strong coupling constant (see Section 1.2) in Figure 1.6, showing a significant decrease of α_s between scales corresponding to m_c and m_b.[8]

[7] On–shell top production is outside the kinematic range accessible to present *ep* experiments.

[8] In practice, the scale for the perturbative expansion is in general not defined by the quark mass alone. Rather, a combination with some other characteristic quantity, e.g. Q^2 or the quark transverse momentum, is chosen.

By comparing the theoretical predictions with experimental results, the mechanisms of heavy flavour production and, more generally, the hard subprocesses underlying *ep* interactions can be investigated. Due to a hard fragmentation of heavy quarks, the parton and hadron levels are considered to be closely related. Also, heavy flavour measurements provide information on the gluon content of the proton, because the cross section is dominated by gluon–induced processes.

It should be noted that, at the HERA *ep* centre–of–mass energy of about 300 GeV, beauty production is a relatively rare process with a cross section two and three orders of magnitude below charm and total cross sections respectively. For this reason, most of the experimental information on heavy flavour production has so far been obtained from charm measurements. Due to the advantages in the theoretical treatment, however, there is a strong motivation to repeat (and possibly extend) these studies to the beauty sector.

After these introductory remarks, in the following sections a more detailed description of beauty production, fragmentation and decay is given. The discussion is restricted to *open* beauty processes, where the heavy quark and anti–quark resulting from the hard subprocess hadronise independently from each other. A possible formation of a $b\bar{b}$ vector meson state, which is colour–neutral and is thus "hiding" its beauty content, turns out to be irrelevant for this analysis and, therefore, is not considered here. As the description of charm and beauty production follow similar concepts, most of the following discussion holds also for charm.

1.5.1 Production of *b* Quarks

Beauty production is dominated by gluon–induced photoproduction processes. In the calculation of the parton–level cross section, the photon–gluon cross section is, therefore, of particular relevance.

Boson–Gluon Fusion

In leading order, i. e. $\mathcal{O}(\alpha\alpha_s)$, the dominant contribution to the beauty production cross section arises from *boson–gluon fusion* (BGF), where the photon from the positron and a gluon coming from the proton form a $b\bar{b}$ pair, see Figure 1.7(a). The cross section can be calculated according to [25]

$$\hat{\sigma}_{BGF} = \frac{\pi e_b^2 \alpha\alpha_s}{\hat{s}} \left\{ \left(2 + 2\omega - \omega^2\right) \ln\frac{1+\chi}{1-\chi} - 2\chi(1+\chi) \right\} \quad . \tag{1.29}$$

Here, $\hat{s} = (\mathbf{p}_b + \mathbf{p}_{\bar{b}})^2$ is the squared centre–of–mass energy of the $b\bar{b}$ pair, e_b denotes the b quark's electromagnetic charge and ω and χ are given by $\omega = 4m_b^2/\hat{s}$ and $\chi = \sqrt{1-\omega}$ respectively. The charm BGF cross section is obtained by replacing m_b and e_b in Equation (1.29) with the corresponding charm quark values m_c and e_c. Due to the relatively larger mass and smaller charge of the b quark, the factor $e^2/\hat{s}$ is typically much smaller in the beauty case. Beauty production is, therefore, heavily suppressed with respect to charm production. The kinematic region close to the beauty production threshold is strongly favoured, which is reflected in typically small b quark transverse momenta p_t with respect to the beam axis.

Both the dominance of close–to–threshold production and the suppression with respect to charm remain valid when including resolved photon and higher order QCD processes.

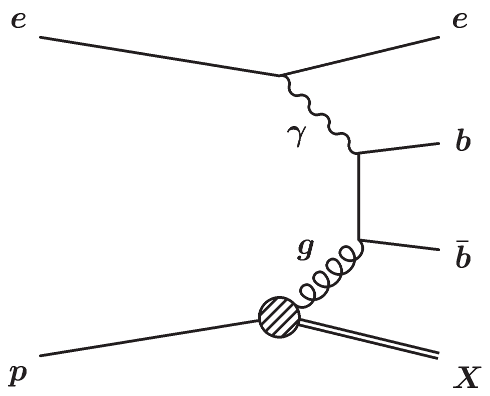

Figure 1.7: *b production in LO QCD: Boson–gluon fusion diagram.*

Resolved Photon Processes

In addition to direct photon interactions, i. e. BGF, also resolved photon processes may have to be considered, see Section 1.3.2. Two example diagrams are shown in Figure 1.8. For light quark photoproduction the resolved photon component is dominant, and there is also strong experimental indication for a significant resolved contribution to charm production. In the case of beauty production, however, the situation has not been clarified yet. It should be noted that the separation of the direct and resolved components is only unambiguous in the LO picture.

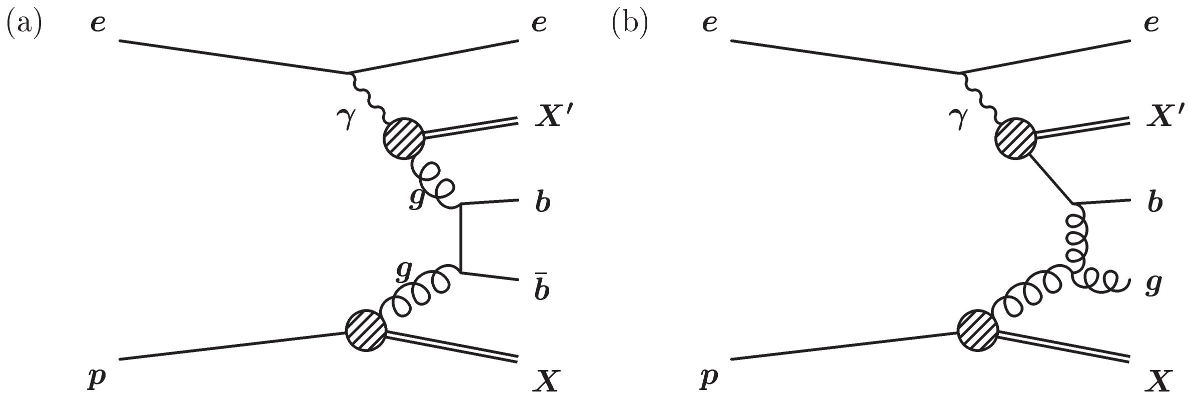

Figure 1.8: *Resolved b production in LO QCD: Diagrams for (a) gluon–gluon fusion and (b) b excitation in the photon.*

Next–to–Leading Order Contributions

Perturbative QCD calculations of beauty production are available also in next–to–leading order (NLO). The NLO contributions to the cross section are found to be significant. Some of the corresponding Feynman graphs are given in Figure 1.9. In the calculations, two conceptually different approaches can be distinguished:[9]

- In the *massive scheme*, only light quarks and gluons are considered as active initial state partons. In the perturbative expansion of the hard scattering cross section $\hat{\sigma}$ all terms up to $\mathcal{O}(\alpha_s^2)$ are taken into account (*fixed order* approach). This method is reliably applicable in the phase space region where the transverse momentum p_t of the heavy quark is less than or similar to its mass.
- For $p_t \gg m_q$, large terms proportional to $\ln(p_t^2/m_q^2)$, accounting for collinear gluon emission from a heavy quark and gluon or photon splitting into a heavy $q\bar{q}$ pair, might spoil the convergence of the perturbation series. In *resummed calculations*, these contributions are included also beyond $\mathcal{O}(\alpha_s^2)$. Technically, this can be achieved by absorbing the heavy quark associated collinear singularities into fragmentation functions and PDFs. As this requires setting the quark mass to zero, this approach is denoted the *massless scheme* In contrast to the massive scheme, where the heavy flavours can only be produced dynamically in the hard subprocess, the massless approach treats the heavy quarks as intrinsic photon and proton constituents, which can appear in the final state through heavy quark excitation processes.

For the kinematic range relevant to this analysis the massive scheme is considered the appropriate approach. The production cross section decreases rapidly with increasing p_t and only minor contributions from the region $p_t \gg m_b$ are expected.

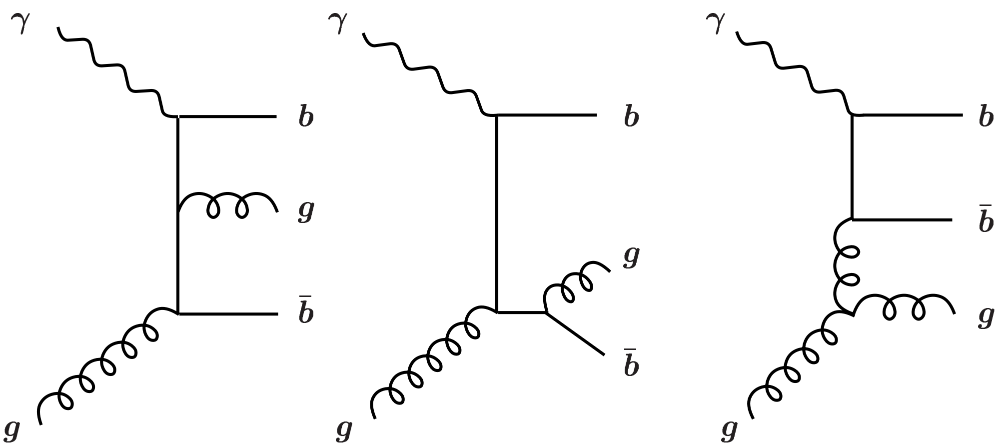

Figure 1.9: *Examples for NLO QCD processes contributing to heavy flavour production.*

[9]See [26] for a more profound discussion.

1.5.2 Beauty–Flavoured Hadrons

Due to colour confinement, a measurement of b quark production can only be performed indirectly. Only hadron–level observables are accessible by experiment. Some relevant features of b quark fragmentation and the resulting beauty hadrons are sketched in the following.

Fragmentation of b Quarks

A simple and widely used model for the formation of heavy hadrons is independent fragmentation (see Section 1.4) according to the *Peterson fragmentation function* [27]

$$\mathcal{D}_q^h(z) \sim \frac{1/z}{\left(1 - 1/z - \epsilon_q/(1-z)\right)^2} \quad . \tag{1.30}$$

Again, z denotes the fraction of the quark momentum carried by the hadron. The free parameter ϵ_q is to be determined experimentally.

An extraction of ϵ_q needs independent information from both the parton and the hadron levels. At ep colliders this is difficult because the parton level centre–of–mass energy is a priori not known and, therefore, the reaction kinematics are not sufficiently constrained. Instead, measurements at e^+e^- colliders are used as experimental input to the fragmentation model. These measurements yield significantly lower ϵ values for

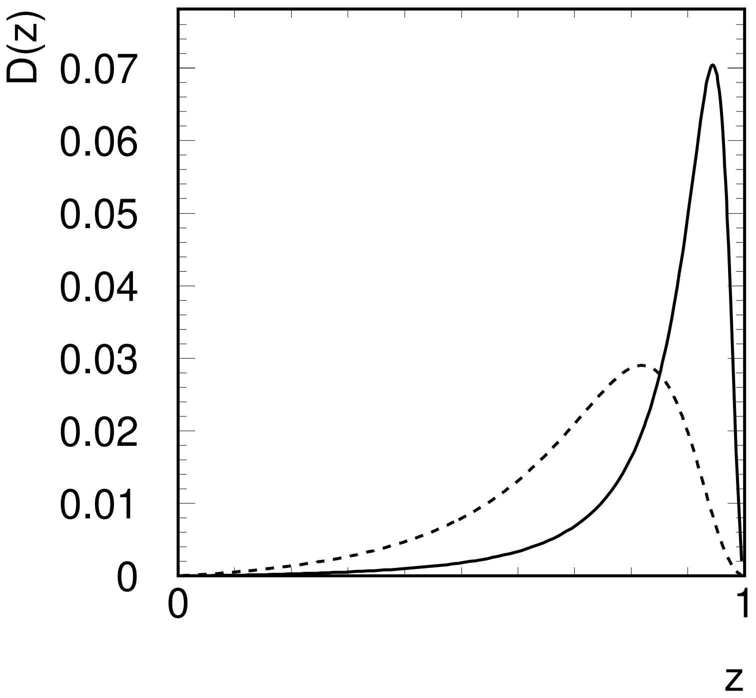

Figure 1.10: *Peterson fragmentation function for beauty (full line) and charm (dashed line), where the values for the fragmentation parameter ϵ have been chosen according to [28].*

beauty compared to charm, e.g. [28] $\epsilon_b = 0.0033$ and $\epsilon_c = 0.040$.[10] This means that $\mathcal{D}_b^h(z)$ peaks at higher z values than $\mathcal{D}_c^h(z)$ (see Figure 1.10), i. e. the fragmentation is *harder* for b quarks than in the charm case.

This observation is also valid for other fragmentation models, e.g. the *Lund string model* which combines string fragmentation (see Section 1.4) with the *Lund fragmentation function* [29] and is used in this analysis within the framework of Monte Carlo event generators, cf. Section 1.7.

Beauty–Flavoured Hadrons

Reflecting the difference in quark masses, see Section 1.1, beauty–flavoured hadrons are considerably heavier than hadrons with only light valence quarks u, d and s. There is also a sizeable mass difference between charm and beauty hadrons. The masses of beauty mesons are typically around 5.3 GeV (see Table 1.3). This can be compared to, e.g., the D^0 charm meson with a mass of 1.8 GeV and the light meson π^0 with $m_\pi \approx 0.135$ GeV.

The second characteristic property of beauty particles is their long lifetime. While beauty meson lifetimes are of the order of 1.5 ps (cf. Table 1.3), the lifetime of for example the D^0 meson is 0.4 ps, which translate into proper decay lengths $c\tau$ of 450 μm and 120 μm respectively. This reflects the different sizes of the Cabbibo–Kobayashi–Maskawa (CKM) matrix elements $|V_{ij}|$ corresponding to the dominant decays $b \to cW^-$ and $c \to sW^+$:

$$|V_{cb}| = 0.0412 \pm 0.0020 \;\; [4] \quad \text{and} \quad |V_{cs}| = 0.224 \pm 0.016 \;\; [4] \;\; . \tag{1.31}$$

Both the mass and the lifetime signature of beauty hadrons are exploited in this analysis to separate the beauty signal from background processes (including charm production) on a statistical basis, see Chapter 3.

hadron	quark content	mass/MeV	lifetime τ /ps	proper decay length $c\tau$/ μm
B^0	bd	5279.4 ± 0.7	1.542 ± 0.016	462 μm
$B^\pm$	bu	5279.1 ± 0.5	1.674 ± 0.018	502 μm
B_s^0	bs	5369.6 ± 2.4	1.461 ± 0.057	438 μm
Λ_b^0	bdu	5624 ± 9	1.229 ± 0.080	368 μm
D^0	cu	1864.1 ± 1.0	0.4117 ± 0.0027	123 μm
$D^\pm$	cd	1869.3 ± 0.5	1.051 ± 0.013	315 μm
$D_s^\pm$	cs	1968.5 ± 0.6	0.490 ± 0.009	147 μm
Λ_c^+	cud	2284.9 ± 0.6	0.200 ± 0.006	60 μm

Table 1.3: *Examples for beauty and charm–flavoured hadrons.*

[10]These ϵ_q values result from a fixed order (α_s^2) QCD fit to heavy hadron spectra measured at the LEP e^+e^- collider.

1.5.3 Semi–Muonic Beauty Decays

Although beauty–flavoured hadrons are long–lived compared to other strongly decaying particles, the time–scale of the decay, which is of the order of 10^{-12} s, is too short to observe beauty hadrons directly. Only the decay products are accessible experimentally.

Beauty production in *ep* collisions is a relatively rare process. A clean experimental signature is, therefore, highly desirable. Such a signature is provided by high–energy leptons from the decay of beauty–flavoured hadrons. For this analysis, the semi–muonic decay mode is chosen.

Since $|V_{ub}| = 0.0036 \pm 0.0007$ [4] is much smaller than $|V_{cb}|$, see Equation (1.31), b quarks predominantly decay into c quarks via the emission of a virtual W. The W produces two fermions $f\bar{f}'$; with a $(10.57 \pm 0.22)\%$ probability [4] these are a muon μ and a muon–neutrino ν_μ, cf. Figure 1.11(a). In addition to these direct (*prompt*) decays there is also muon production from b decays through *cascade processes* as shown in Figure 1.11(b), where the charm quark resulting from the b decay decays muonically.

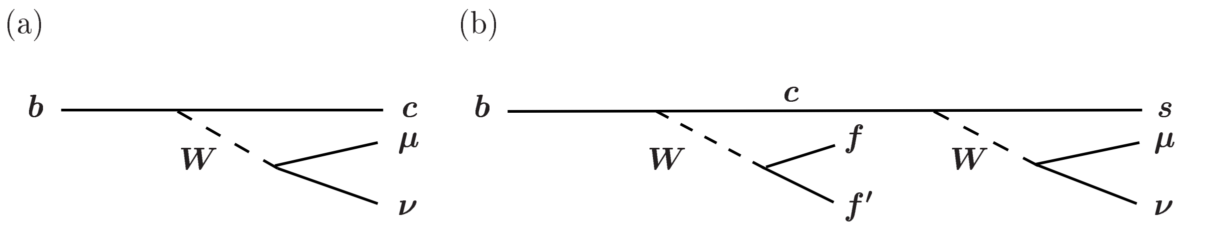

Figure 1.11: *Muonic b quark decay: (a) prompt, (b) charm cascade.*

The most simple picture for the decay of beauty hadrons is the *spectator model.* Going effectively back to a parton level description, the hadron decay is treated as the decay of a free b quark, the other partons within the hadron playing no role in the decay. Figure 1.12 shows the semi–muonic decay of a B^+ meson viewed in the spectator model.

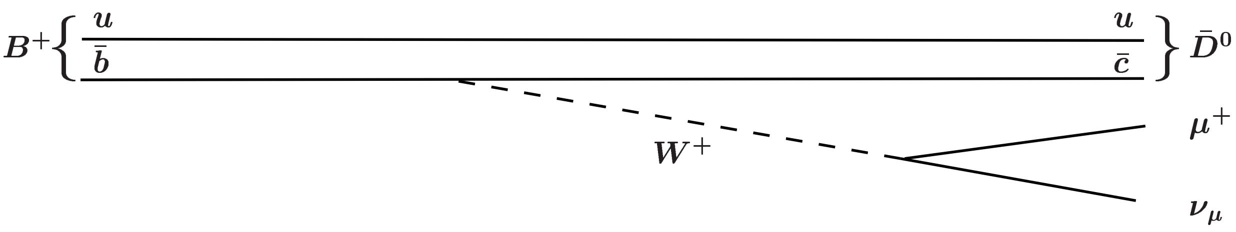

Figure 1.12: *The semi–muonic decay $B^+ \to \mu^+\nu_\mu\bar{D}^0$ in the spectator model.*

1.6 Monte Carlo Integration Programs

As stated in Section 1.5.2, perturbative QCD calculations of beauty production are available in next–to–leading order. Examples relevant for this thesis are the calculation [30, 31] of Frixione et al. for the photoproduction domain (considering also resolved photon processes) and the calculation of DIS processes by Harris and Smith [32, 33]. In both cases the calculations are performed in the massive scheme, cf. Section 1.5.1, and are implemented in integration programs (in the following denoted FMNR and HVQDIS respectively) based on Monte Carlo (MC) methods. The errors on the predictions are dominated by the b quark mass uncertainty and the choice of the factorisation and renormalisation scales.

HVQDIS cross section results in NLO and LO for heavy quark production in low Q^2 DIS processes at the HERA ep centre–of–mass energy of 300 GeV are given in Table 1.4. Here, in addition to cuts on the kinematic variables Q^2 and y, the phase space has been restricted to heavy quark pseudorapidities $|\eta^q| < 1.5$ and transverse momenta $p_t^q > 5$ GeV, in some analogy to jet selection criteria applied in the later cross section measurement. This results in a considerable enrichment of beauty with respect to charm but still the NLO charm production cross section exceeds the beauty production cross section by a factor ~ 14. The corrections with respect to the LO cross sections are found to be large in both cases (51% and 37% for charm and beauty respectively).

	$\sigma^{vis}(ep \to qX)$ [nb] $(2 < Q^2 < 100,\ 0.05 < y < 0.7,\ \|\eta^q\| < 1.5,\ p_t^q > 5\text{ GeV})$	
	charm ($q = c$)	beauty ($q = b$)
NLO	2.71 ± 0.19	0.197 ± 0.002
LO	1.79	0.144

Table 1.4: *Charm and beauty production cross sections in low Q^2 DIS as obtained from HVQDIS for an ep centre–of–mass energy of* 300 GeV *and heavy quark pseudorapidities* $|\eta^q| < 1.5$ *and transverse momenta* $p_t^q > 5$ GeV.

The FMNR and HVQDIS output includes the heavy quark four–vectors, which can be evolved to hadron level using fragmentation functions. Here, the Peterson fragmentation function (1.30) is used. The decay of the heavy hadrons are also modelled, so that the kinematics of the decay products can be included in the definition of differential and visible cross sections. For the purposes of this (inclusive muon) analysis, the hadron spectrum is folded with a beauty decay muon momentum distribution obtained from the LO Monte Carlo event generator AROMA (see below).

1.7 Monte Carlo Event Generators

In order to compare theoretical models with experimental data, in general details of the event topology and detector effects have to be considered. This requires an event–by–event prediction for the complete hadronic final state, which is beyond the scope of the

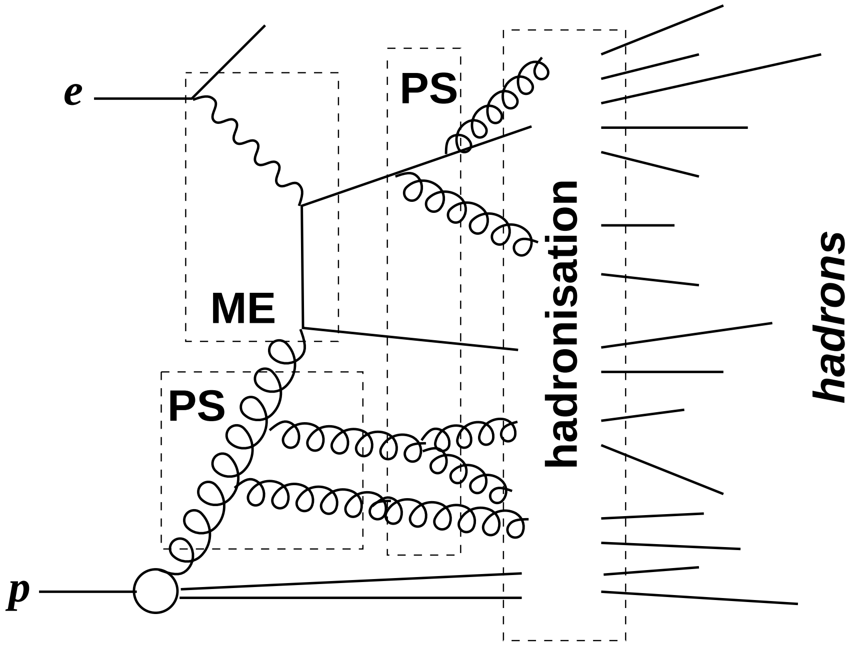

Figure 1.13: *Elements of an ep event generator.*

QCD programs discussed in the previous section. *Event generators*, also based on Monte Carlo techniques, are used for this purpose.

Taking the boson–gluon fusion process as an example, the elements of an event generator are sketched in Figure 1.13. The starting point is the hard partonic subprocess described by a matrix element (ME), which in present MC generators is implemented in LO only. Initial and final state parton showers (PS) produce additional partons which subsequently hadronise, see Section 1.4. Within all MC generators relevant for this analysis, the hadronisation is performed in the framework of the JETSET [34] program using the string fragmentation model in combination with the Lund fragmentation function.

Beauty and charm production events are simulated for this analysis using the AROMA program [35]. AROMA provides a description of heavy flavour production in both γp and DIS. It should be noted, however, that only direct photoproduction is included here.

In order to model background to semi–muonic beauty decays from mis–identified hadrons (see Chapter 3), an inclusive event sample is needed. For the photoproduction analysis this is obtained from the PYTHIA program [34], in which it is possible to include also resolved photon processes. A corresponding DIS sample is produced with the event generator DJANGO [36]. For systematic studies, direct and resolved beauty photoproduction events are obtained from the RAPGAP [37] program.

Each of the event generators mentioned above are based on DGLAP parton evolution (see Section 1.3.1). The alternative CCFM ansatz, cf. Equation (1.21), is implemented in the CASCADE [38] program. The unintegrated (k_t–dependent) gluon density has been extracted from a fit to the inclusive proton structure function F_2. Resolved photon processes are not included explicitly.

Chapter 2

The H1 Experiment at HERA

The *ep* collider HERA (*Hadron–Elektron–Ring–Anlage*) at DESY (*Deutsches Elektronen–Synchrotron*) in Hamburg consists of two separate storage rings located in a single tunnel of about 6300 m length. A schematic overview of HERA, including the injectors and the chain of pre–accelerators, is shown in Figure 2.1. In 1997, the data–taking period relevant for this analysis, HERA collided positrons and protons at energies of 27.5 GeV and 820 GeV respectively, which corresponds to a centre–of–mass energy of about 300 GeV. The accelerated particles do not form a continuous beam but are stored in up to $\sim$ 200 *bunches*. In two interaction regions proton and positron bunches collide at a rate of 10.4 MHz corresponding to a separation in time of 96 ns. The achieved luminosity is of the order of 10^{31} cm^{-2}s^{-1}.

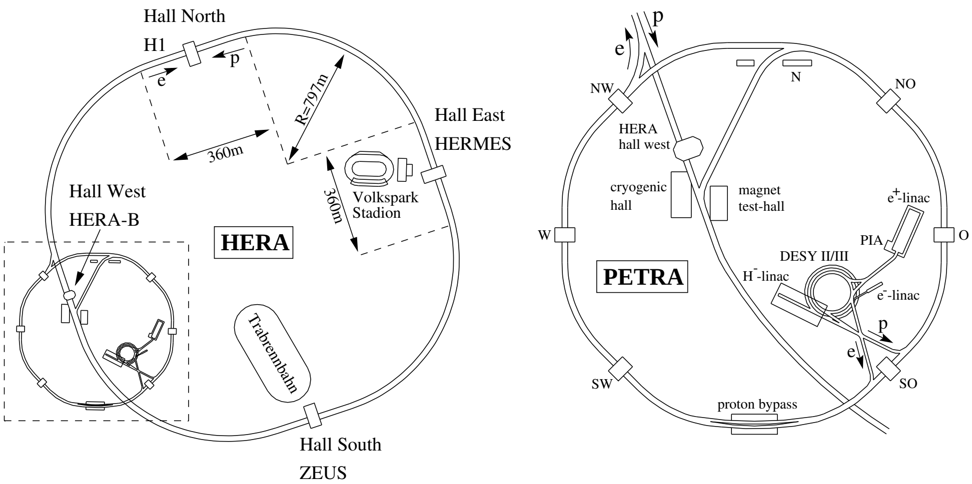

Figure 2.1: *The ep collider HERA at DESY. In the right part the injectors and pre-accelerators are shown, on the left HERA itself.*

In order to study the physics of *ep* scattering, two multi–purpose detectors have been built around the two interaction regions: H1 (interaction region north) and ZEUS (interaction region south). In the HERMES detector (east hall) the positron beam is guided through a polarised gas target to investigate nucleon spin structure. The west hall hosts the most recent experiment, HERA–B. Here, the HERA proton beam halo is used on a wire target. The physics program focuses on heavy flavour production and decay processes, aiming in particular at measuring CP violation in B meson systems.

The analysis presented in this thesis was performed using data obtained by the H1 experiment. Figure 2.2 shows a schematic view of the H1 detector. The asymmetric arrangement of the components along the beam axis is due to the large energy difference of the HERA beams resulting in a large boost of the final state particles along the direction of the incoming proton. In standard H1 convention, the direction of the proton beam, which is also referred to as the *forward direction*, defines the z–axis of a right–handed coordinate system. A detailed description of the H1 detector can be found in [39]. In the following, the detector components relevant for this measurement are discussed briefly.

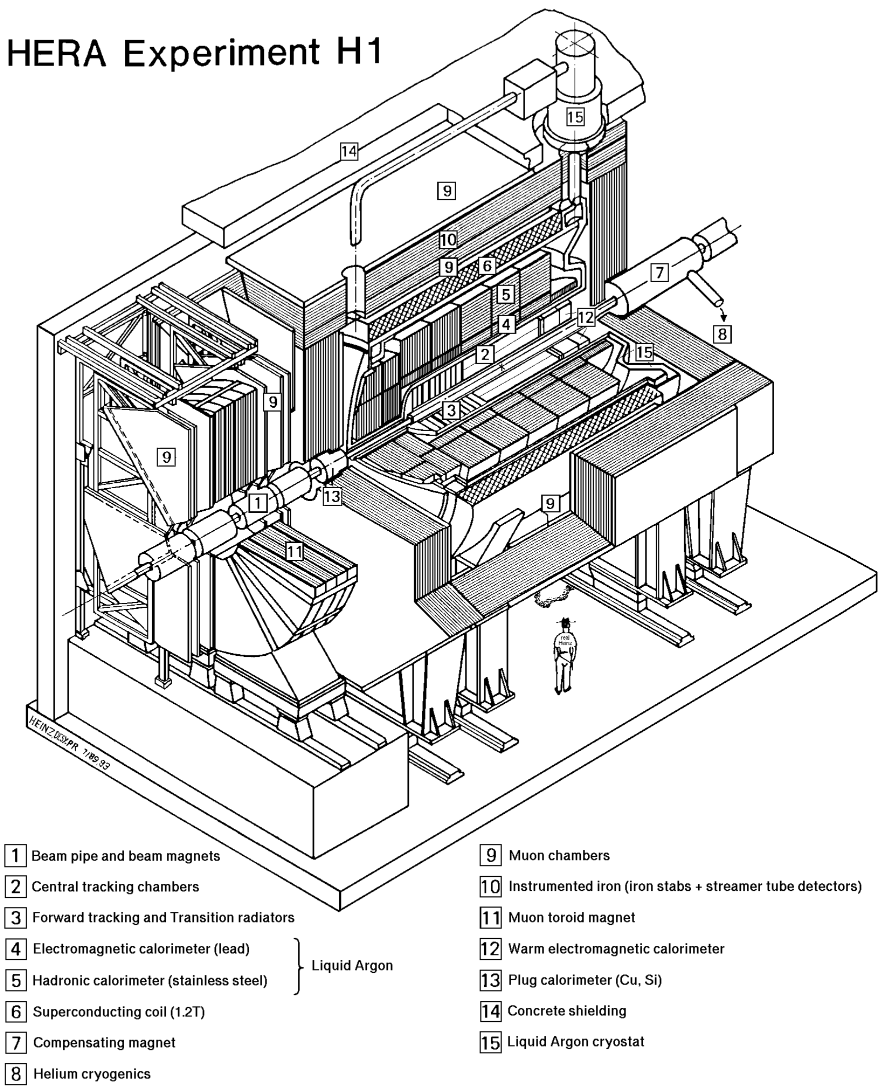

Figure 2.2: *A schematic view of the H1 detector.*

2.1 Tracking Devices

The purpose of the tracking chambers is the reconstruction of charged particle trajectories. With a strong magnetic field (1.15 T) parallel to the z axis, provided by a superconducting coil located between the main calorimeter and the muon system, a momentum measurement is also possible. In addition, information on event *vertices*, marking the position of the ep interaction (*primary vertex*) and decays of long–lived particles (*secondary vertices*), is obtained by extrapolating the reconstructed tracks back to the beam axis.

The asymmetric structure of the H1 detector is also reflected in the arrangement of the tracking devices (see Figure 2.3). The *central tracking system* surrounds the beam pipe in a polar angular region from about 15° to 165°. The *forward tracking chambers* cover the region $5° \lesssim \theta \lesssim 25°$. *Backward tracking* information is provided by the *backward drift chamber* BDC and the *backward silicon tracker* BST. The largest volume in the central tracking system is filled by the two–part *central jet chamber* CJC. Two additional drift chambers, the *central inner* and *central outer z chambers* (CIZ,COZ), have been installed to improve the z and θ resolution. The system is complemented by two *multi–wire proportional chambers* (MWPC), used for triggering purposes, and the *central silicon tracker* (CST) providing precise tracking and vertexing close to the beam. The forward tracking system consists of three identical sub–units arranged along the beam line. Each of these *super modules* contains two drift chambers, which are called *planar* and *radial* chambers according to the different wire orientations. Between the drift chamber modules there is a MWPC (forward proportional chamber, FPC), which provides trigger signals, and two transition radiation detectors.

In the following, the CJC and the CST, which are of particular relevance for this analysis, are discussed in more detail.

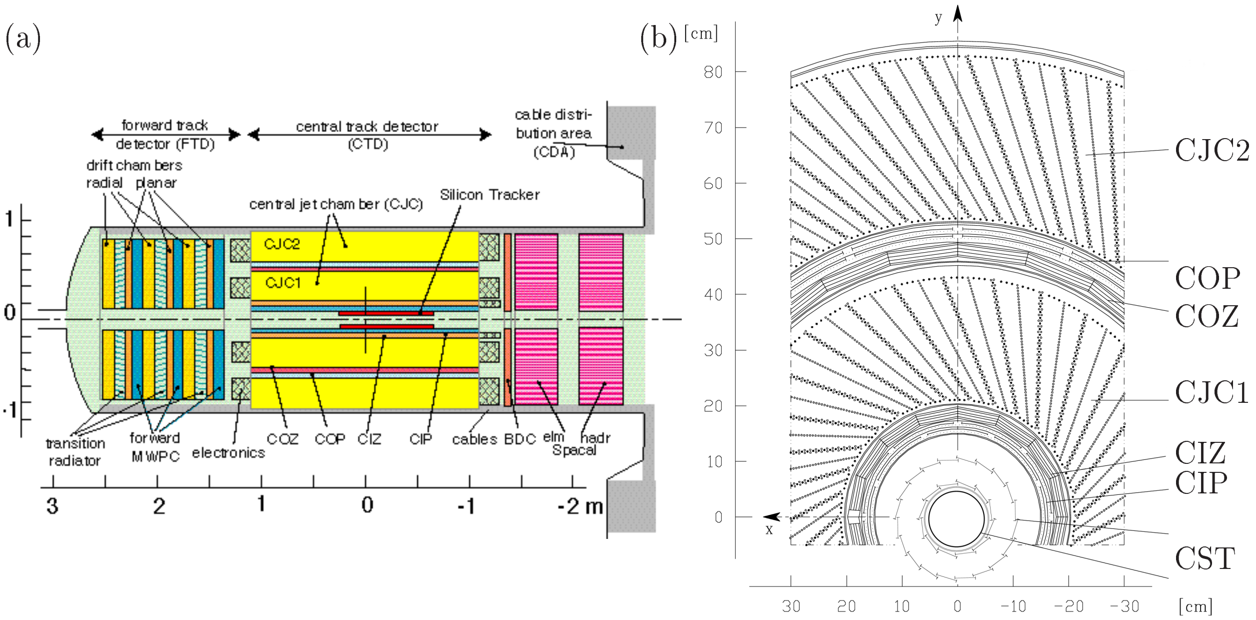

Figure 2.3: *(a) Side view of the H1 tracking systems, (b) radial view of the central tracking chambers.*

2.1.1 Central Jet Chamber CJC

The central jet chamber consists of two separate coaxial cylinders CJC1 and CJC2. The active region, -112.5 cm $\leq z \leq$ 107.5 cm, corresponds to a polar acceptance of $11° \lesssim \theta \lesssim 170°$ and $26° \lesssim \theta \lesssim 155°$ for CJC1 and CJC2 respectively. Anode sense wires and drift field shaping cathode wires running parallel to the beam axis are arranged in planes subdividing the CJC1 (CJC2) volume into 30 (60) identical *cells*. The wire planes are tilted by about 30° to account for the non–zero Lorentz angle due to the presence of the magnetic field. The position of a crossing particle in the transverse plane can be measured with an accuracy of about 140 μm with a high time resolution of $\approx$ 0.5 ns. A transverse momentum resolution of $\sigma(p_t)/p_t^2 \approx 0.5\%$ GeV^{-1} [40] is achieved. As the sense wires are read out at both ends, the particle's position along the beam axis can also be determined via charge division. The intrinsic resolution in z is significantly worse ($\gtrsim$ 22 mm), however, than in the transverse plane. In order to improve this, information from the z chambers, which have a single hit z resolution of about 380 μm, is included in the track reconstruction. A more detailed description of the the CJC, including an outline of the track reconstruction procedure can be found in [40, 41].

2.1.2 Central Vertex Detector CST

The central silicon tracker CST consists of two cylindrical layers of double sided silicon strip detectors arranged symmetrically around the beam axis at radii of 5.7 cm and 9.7 cm, cf. Figure 2.4. Its active length of 35.6 cm covers polar angles in the range $30° \lesssim \theta \lesssim 150°$.[1]

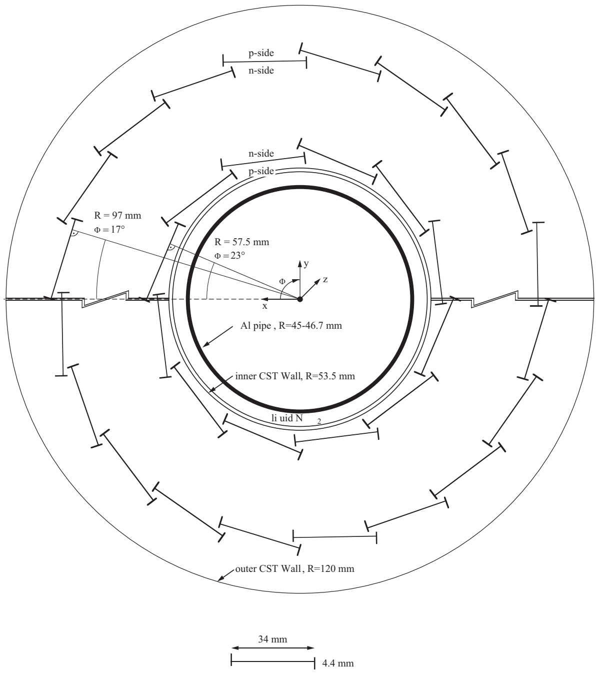

Figure 2.4: *Schematic $r\varphi$ view of the CST.*

[1] This is the two–layer acceptance for particles originating from the nominal interaction point.

The inner (outer) CST layer contains 12 (20) identical and slightly overlapping *ladders*, each composed of two identical *half ladders* of 22.1 cm length and 3.4 cm width (see Figure 2.5). Each half–ladder consists of three silicon sensors and a hybrid structure carrying the readout electronics.

On the outer face (*p–side*) of each sensor there are 1280 p^+–acceptor strip implants running parallel to the z–axis with a pitch of 25 μm. Every second strip is read out, resulting in a single hit resolution in the $r\varphi$ projection of 12 μm [42]. The opposite (n-) side is used to determine the z–position of incident particles. Here, n^+–donator strip implants of 88 μm pitch are oriented perpendicular to the z–axis. Every n–side strip is read out via an additional metal layer. However, the readout lines of the three sensors within a half ladder are daisy–chained, which produces a three–fold ambiguity in the z–coordinate to be resolved within the reconstruction procedure. The readout layer gives rise to a non–negligible capacity, which affects the hit signal–to–noise ratio. Due to the larger pitch, the intrinsic hit z–resolution σ_z is significantly worse than the corresponding $r\varphi$ value. σ_z depends on the incident angle, with a minimum of 22 μm for $\theta \approx 90° \pm 15°$ [43].

The hit–finding algorithm is described in [44]. In a first step, which is performed independently for the p and n–side, neighbouring strip signals are combined into *clusters*. The association of p and n–side clusters in a second step results in three-dimensional *space points*.

For further information on the CST detector design, readout and reconstruction see [42, 43, 44].

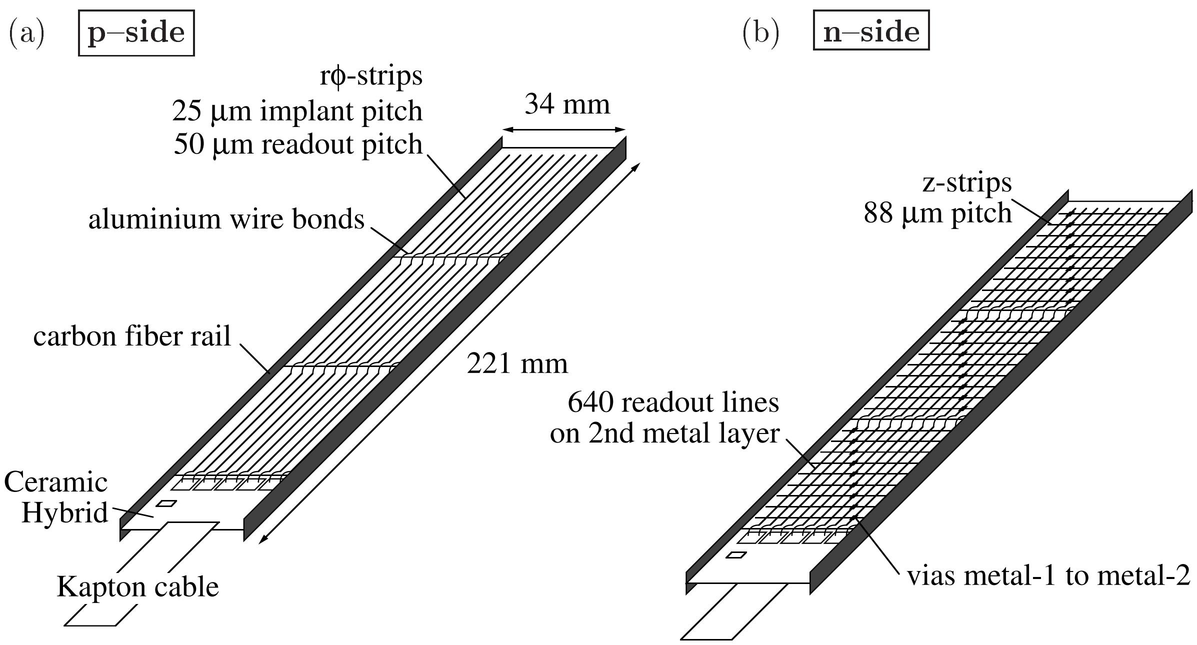

Figure 2.5: *CST half ladders; (a) p–side, (b) n–side.*

2.2 Calorimeters

For particle energy measurement the H1 detector is equipped almost hermetically with several calorimeters. Relevant for this analysis are the *liquid argon calorimeter* LArC and the backward calorimeter SpaCal. While the LArC is important for the reconstruction of the hadronic final state, the SpaCal is used mainly to detect and measure the scattered positron in the low Q^2 DIS regime.

2.2.1 The Liquid Argon Calorimeter LArC

The LArC encloses the central tracking system in the region $4^\circ \lesssim \theta \lesssim 153^\circ$. Absorbing and readout plates form a cell structure containing liquid argon as active material. The inner *electromagnetic* region with high granularity and lead absorber plates is optimised for the detection of electrons and photons. In contrast, the outer part (*hadronic section*) is designed for the measurement of hadronic energy deposits; the cells are larger and the absorber material is stainless steel. The LArC is a non–compensating calorimeter, i.e. for the same primary energy an electromagnetically interacting particle leads to a larger signal than a hadron. In the energy reconstruction this has to be considered by a suitable signal weighting procedure. The energy resolution was determined in a test beam to be $\sigma(E)/E \approx 12\%/\sqrt{E[\mathrm{GeV}]}$ for electrons in the electromagnetic section and $\sigma(E)/E \approx 50\%/\sqrt{E}$ for single pions in the hadronic part.

(a) (b)

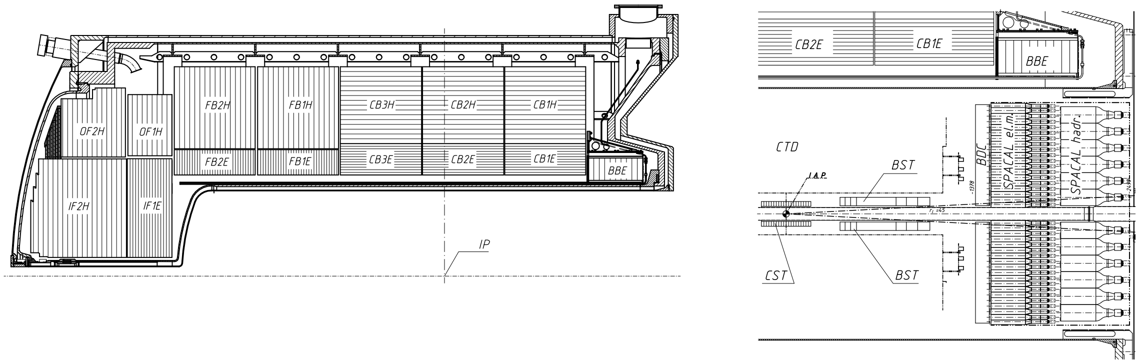

Figure 2.6: *Side view of (a) the LArC and (b) the backward detector region with the SpaCal. In (b) the backward tracking devices BDC and BST are also shown (see Section 2.1).*

2.2.2 The Backward Calorimeter SpaCal

The cells of the backward calorimeter, which covers the polar angle region $153^\circ \lesssim \theta \lesssim 178^\circ$, consist of scintillating fibres embedded in lead. This structure is called a *spaghetti calorimeter* (SpaCal). This device is also divided into an electromagnetic section (1192 cells with a transverse cross section of 4.5 cm $\times$ 4.5 cm) and a hadronic section (136 cells, 11.93 cm × 11.90 cm). Energies are measured with $\sigma(E)/E \approx 8\%/\sqrt{E[\text{GeV}]}$ and $30\%/\sqrt{E[\text{GeV}]}$ respectively. High resolution in both space and time is achieved, the latter being used for triggering based on time–of–flight methods.

2.3 Central Muon System

While other particles in general are stopped within the inner detector region, the energy loss of muons is typically quite small. The muon systems are, therefore, located outside the central calorimeters. The iron yoke, which encloses the main H1 detector in order to guide the magnetic flux produced by the superconducting coil outside the tracking detectors, is instrumented with detectors which together form the *central muon system*. The central muon system is used in this analysis to identify the beauty decay muons. As the analysis method relies on the reconstruction of the muon track within the CST, only the central (*barrel*) part of the instrumented iron yoke is of relevance here.

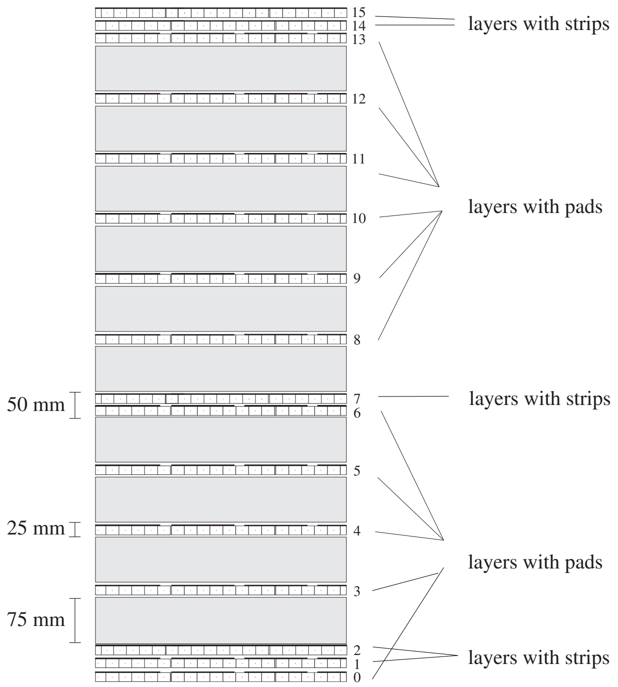

Figure 2.7: *Cross section view of the instrumented iron. The streamer tube layers 3, 4, 5, 8 and 12 are used for trigger purposes.*

Figure 2.7 illustrates the internal structure of the instrumented iron. It consists of ten 7.5 cm layers of iron plates equipped on both sides with streamer tubes. Eight tubes form one *profile* and two profiles are combined into a gas tight *element*. In total there are sixteen element layers for muon detection. In addition there are strip and pad electrodes mounted on top of the streamer elements. Combining the information from the different parts of the system, three–dimensional particle tracks can be reconstructed. Details of the reconstruction algorithm can be found in [45].

2.4 Luminosity System

The luminosity measurement is based on the electromagnetic *Bethe–Heitler process* $ep \to ep\gamma$, which has a high cross section, is theoretically very well understood and, therefore, precisely calculable. The experimental signature is an $e\gamma$ coincidence in two dedicated devices, which are located in the backward HERA tunnel outside the main detector: a *photon detector* at $z \approx -107$ m and an *electron tagger* (ET33) at $z \approx -33$ m.

These detectors have also proved useful for the study of photoproduction processes, where the beam positron is scattered under very small angles. Two additional electron taggers are available for this purpose at $z \approx -7$ m (ET8) and $z \approx -44$ m (ET44). For this class of measurements the photon detector is used as a veto counter to suppress the background from Bethe–Heitler processes.

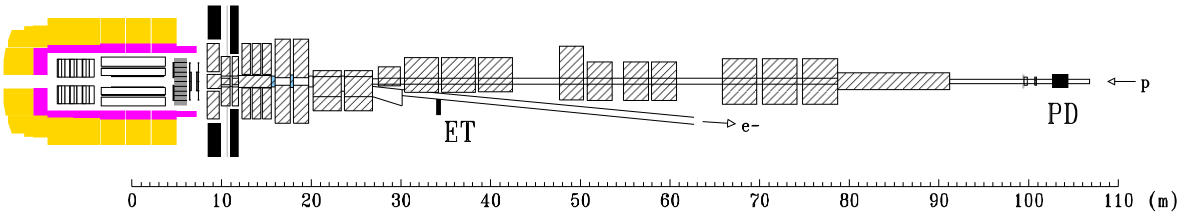

Figure 2.8: *The luminosity system, consisting of an electron tagger at $z = -33\,m$ and a photon detector at $z = -103$ m.*

2.5 Data Acquisition and Trigger

As mentioned earlier, the crossing frequency of the particle bunches of the HERA beams is 10.4 MHz. Only in a small fraction of cases, however, does this lead to an ep reaction. The ep event rate is several orders of magnitudes lower than the rate for background processes, which arise mainly from collisions of the beam protons with rest gas atoms within the beam pipe (*beam–gas interactions*). In addition there is *beam-wall background* from off-orbit protons hitting accelerator or detector components. Also muons from cosmic rays penetrating the outer detector shielding have to be considered. In order to account for the limited bandwidth for the data transfer to mass storage devices (*data logging*) and to avoid a high experimental dead time, the event rate of typically 100 kHz has to be reduced to a logging rate of about 10 Hz. This is the task of the *trigger system* providing a fast selection of ep processes and background rejection. The rate is reduced in several steps (*levels*). The chain of trigger levels is sketched in Figure 2.9 indicating for each step typical input and output rates as well as the time scale on which a decision is made.

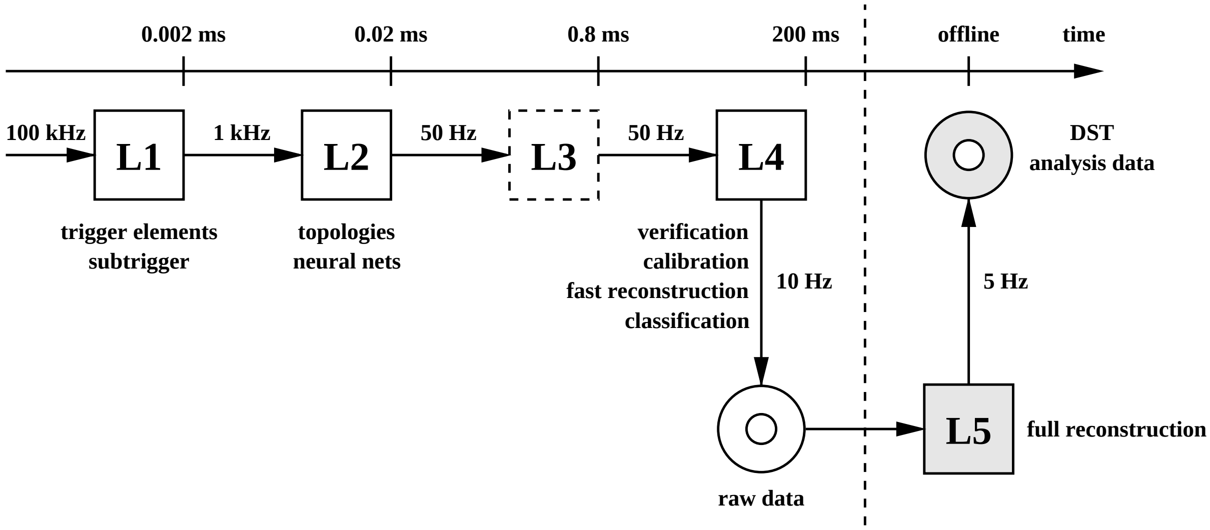

Figure 2.9: *Overview of the trigger system.*

The decision time on the first trigger level (L1) cannot be shorter than the signal shaping time of the subdetectors providing input to the system. For some components this is significantly larger than the interval of 96 ns between two potential *ep* interactions. For this reason, the detector information is stored intermediately in cyclic ring buffers (*pipelines*). The pipeline storage depth of 2.5 μs determines the maximum L1 decision time if the system is to operate dead time free.

The starting point for an L1 decision are L1 *trigger elements* (TE) provided by various subsystems. Each TE contains information as to whether a certain basic pre–defined condition is fulfilled or not. Examples relevant for this analysis are:

- *Central muon trigger*: The central muon trigger uses signals from five of the 16 streamer tubes in the instrumented iron (see Figure 2.7). The L1 trigger element `MU_BAR` requires a hit coincidence in at least two of the innermost four trigger layers in the barrel region.

- *zVtx trigger*: Based on signals from the central MWPC and the innermost FPC, the zVtx trigger provides an estimate of the event vertex z position. The starting point are *rays*, each defined by a four–fold hit coincidence in chamber pads which can be connected in the rz plane by a straight line pointing roughly (± 44 cm in z) to the nominal interaction point. The z intersect of a ray with the beam axis gives an entry in one of the 16 bins of a *zVtx histogram*, see Figure 2.10. Genuine *ep* interactions are signalled by a significant maximum in the $zVtx$ histogram. Further L1 trigger elements are constructed from the numbers of entries in the zVtx histogram (*sum*) as well as the number of entries in and the position of the highest bin (*peak* and *peak position*). For example, four different regions in the *peak* vs. *sum* plane define different levels of the peak significance, see [46], which are encoded in a two–bit TE `zVtx_sig`.

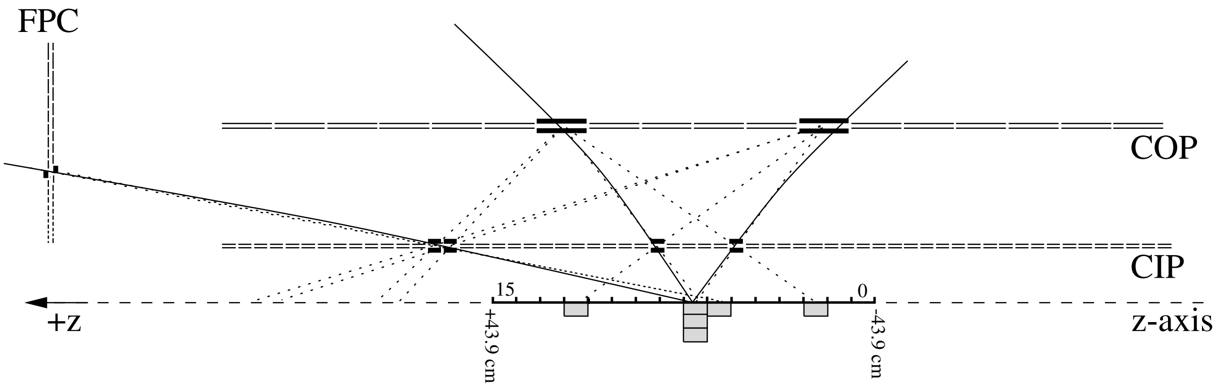

Figure 2.10: *Sketch of the zVtx trigger.*

- *DCrφ trigger*: The drift chamber $r\varphi$ trigger is designed to identify charged particle tracks in a plane perpendicular to the beam axis. The drift time information from ten out of the 54 CJC wire layers is compared to predefined patterns (*masks*). This procedure distinguishes between two transverse momentum ranges (400 MeV $\lesssim p_t \lesssim$ 800 MeV and $p_t \gtrsim$ 800 MeV respectively) as well as between positive and negative charge. L1 trigger elements are defined by, e.g., at least three tracks (`DCRPh_Tc`), at least one negatively charged track (`DCRPh_TNeg`) or at least one high momentum track (`DCRPh_THig`).

- *SpaCal IET*: The SpaCal *inclusive electron trigger* (IET) is based on overlapping *trigger towers*, each consisting of 16 adjacent cells within the electromagnetic section of the calorimeter. The total energy of each trigger tower registered in a time window consistent with an *ep* interaction is compared to three adjustable thresholds, which in 1997 were set to 0.5 GeV, 2 GeV and 6 GeV. In addition, a central and an outer SpaCal region are distinguished corresponding to radial distances from the beam axis below and above 16 cm respectively. This results in 6 distinct trigger conditions encoded in a two–bit TE `SPCLe_IET` for the outer part and three one–bit trigger elements (`SPCLe_IET_Cen_1`, `SPCLe_IET_Cen_2` and `SPCLe_IET_Cen_3`) for the central region.

- *ET triggers*: The trigger elements `LU_ET` and `LU_ET44` indicate significant energy depositions in the electron taggers ET33 and ET44 respectively. These are used, in combination with veto conditions against Bethe–Heitler processes based on photon detector trigger elements (`LU_PD` and `LU_WatVet`), to select photoproduction events.

The trigger elements can be combined in a flexible way into up to 128 logical conditions, which are referred to as L1 *subtriggers* s0…s127. Fulfilling at least one subtrigger condition is necessary for a positive L1 decision (*L1 keep*). However, this is not a sufficient condition as some of the subtriggers are *prescaled*, i.e. only one out of a predefined number (*prescale factor*) of positive decisions is considered.

Following an L1 keep signal the pipelines are stopped, marking the beginning of the primary detector dead time, and the second trigger level (L2) starts to operate. Within 20 μs the decision of certain L1 subtriggers is verified. This longer decision time makes it possible to consider more complex topological conditions, either via matrix operations (L2TT) or using neural networks (L2NN).

In case of a positive L2 decision the pipeline readout is started and the collected information is passed on to a subsequent trigger level L4[2], which is realised in contrast to the hardware trigger systems L1 and L2 as a software trigger running on a PC processor farm. After a fast event reconstruction and a determination of calibration factors, filter algorithms are applied, resulting in a selection decision within 100 ms.

The *raw data* of an event which has been accepted by the L4 system are written to *production output tapes* (POT). In further steps, which together are referred to as *trigger level 5* (L5), the event reconstruction is repeated, now using the calibration data obtained on L4. Also, the event is assigned to one or more *physics classes*. After a further reduction and compression, the event information is written to *data summary tapes* (DST), which are the starting point for physics analysis. All data is organised in predefined tables (*banks*), which are written and accessed using the BOS software package [47].

Any recorded event is labelled in a unique way by a *run number* and an *event number*. All events belonging to a given run have been recorded within the same time period ($\lesssim$ 2 hours) with a constant trigger setup and under similar experimental conditions.

2.6 Detector Simulation

As has been discussed in Section 1.7, the theoretical models to be tested by the experiment are often implemented in Monte Carlo event generators, which provide event–wise topologies as four–vectors of the final state particles. In order to compare to experimental data, the detector response to these final states has to be modelled in a detailed way. The software package GEANT [48] is used in combination with H1 specific detector simulation programs to map the simulated four–vectors on detector signals, which then undergo the same reconstruction procedure as the measured data. In this way the MC model predictions include the detector acceptance and efficiency and can thus be compared directly to experimental data.

[2] A further intermediate trigger level L3 was not operated in 1997

Chapter 3

Analysis Overview

Before entering the details of the analysis, the following chapter gives an overview on some key aspects of the measurement. The choice of the semi–muonic decay channel to measure beauty production is motivated and the expected typical final state topology is sketched. After a description of potential background processes the beauty–sensitive observables used in this measurement are defined and discussed. The chapter concludes with a summary of the analysis strategy.

3.1 Choice of Channel

In this analysis, the semi–muonic decay mode is chosen to measure the beauty production cross section. The branching ratio of about 10% is acceptably large and the decay muon provides a clean experimental starting point, which is highly desirable in view of the strongly suppressed signal cross section (cf. Section 1.5). In contrast to other final state particles, which in general are stopped within the calorimeter, the muon typically traverses the inner detector region as a minimal ionising particle and can be detected in the instrumented iron if its momentum is sufficiently large.

The muon in most cases originates promptly from the beauty decay,[1] thus providing direct access to the decay kinematics. Also, performing an inclusive muon analysis avoids combinatorial background, which in general is an issue in the measurement of hadronic decay modes. Part of the decay information, however, is lost in this approach, because the hadronic decay products are not reconstructed explicitly and the muon neutrino unavoidably escapes detection.

As has been stated in Section 1.5, the dominant beauty production mechanism is the formation of a $b\bar{b}$ pair through boson–gluon fusion. If the momenta of the outgoing quarks are not too low, each of them will form a hadronic jet (see Section 1.4). In this analysis, jet information is needed to estimate the flight direction of the semi–muonically decaying

[1]The relative contribution from charm cascade decays to signal muons in the range $p_t > 2$ GeV and $35° < \theta < 130°$ is expected to be at the level of 13%.

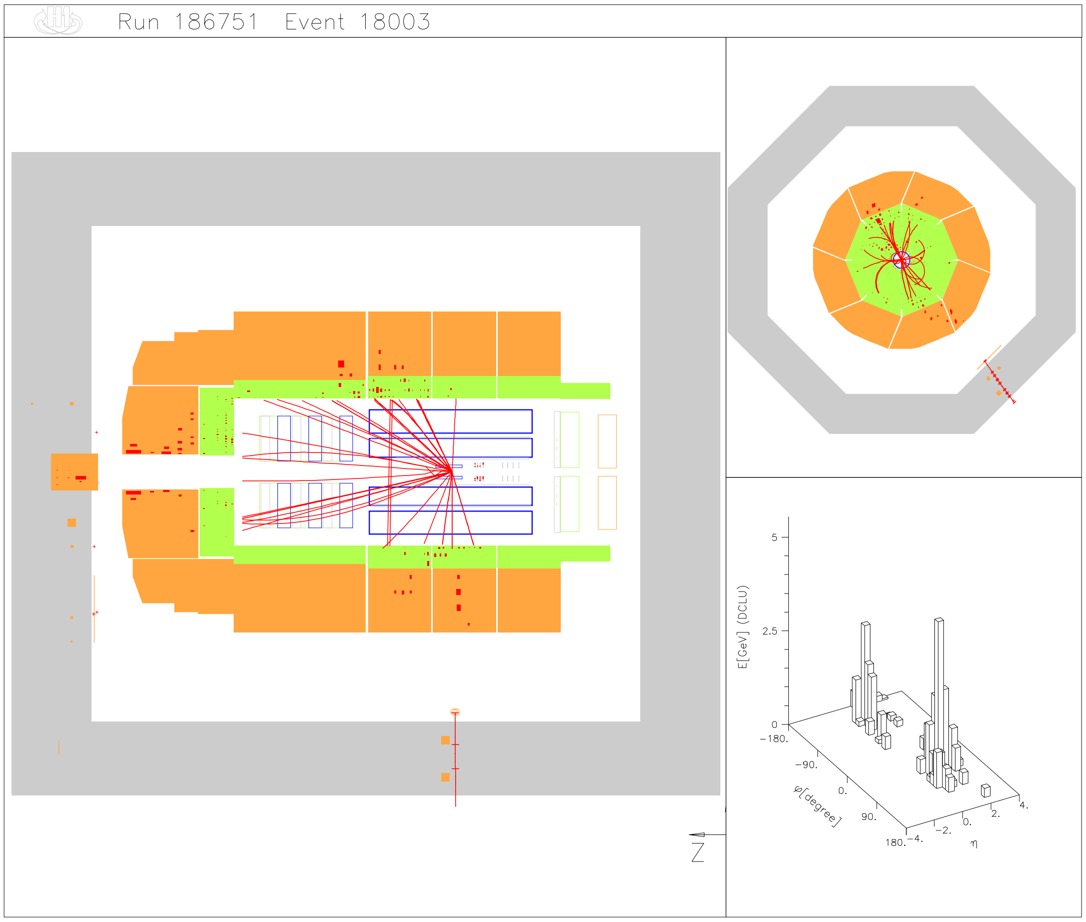

Figure 3.1: *Display of a signal candidate event selected from H1 data taken during 1997.*

beauty hadron, and the selection is based on events with two or more jets with (at least) one of them containing a muon.

It will be discussed below that the vertex detector CST is an indispensable tool for this measurement. The muon, therefore, is required to be found within the CST polar acceptance, i. e. in the central part of the H1 detector. In this region a reliable detection in the instrumented iron is expected for muon transverse momenta $p_t \gtrsim 2$ GeV.

Figure 3.1 shows a graphical representation (*display*) of a signal candidate event selected from H1 data taken during 1997, where the typical final state topology of two jets and a central high–p_t muon is clearly visible.

3.2 Background Processes

Obviously, performing a selection of dijet events with a central high p_t muon will not result in a pure signal sample. There are various background processes producing similar final state topologies. Potentially relevant examples are discussed below.

Semi–Muonic Charm Decays

In principle, the production mechanisms for charm and beauty are the same, and charm hadrons also decay semi–leptonically with branching ratios of the order of 10%. As a consequence, semi–muonic charm decays are expected to produce final state topologies similar to those of signal events. Further, the charm production cross section considerably exceeds the beauty production cross section (cf. Section 1.5). A good separation of charm and beauty events, therefore, is one of the crucial requirements for a measurement of beauty production. Possible starting points for the definition of observable quantities to distinguish between charm and beauty are the differences in mass, lifetime and fragmentation. These will be discussed in more detail in Section 3.3.

Heavy Vector Meson Decays

Muon pair production from the decay of heavy vector mesons, in particular the process $J/\psi \to \mu^+\mu^-$, might also have to be considered as a background source. In contrast to semi–muonic hadron decays, however, all hadronic activity is due to the underlying event and is not directly connected to the decay itself. A study of the final state topologies for muonic J/ψ decays using Monte Carlo simulated events suggests that two central hadronic jets with one of them containing a high–p_t muon is an unlikely configuration. The relative contribution from this source to the final analysis sample is estimated to be below 1% and is thus neglected.

Cosmic Muons

High–energy muons from cosmic rays (*cosmic muons*) penetrate the outer detector shielding at a rate of about 1 kHz. If a cosmic muon crosses the central detector region close to the nominal interaction point then it can be be mis–interpreted as an *ep* event with one or two identified muons in the final state. There is, however, no correlation with the colliding HERA beams. Cosmic muons are thus in general isolated with little additional detector activity and, therefore, do not fulfil the requirement of at least two reconstructed hadron jets. Only in rare cases where a cosmic muon is recorded at the same time as an *ep* event (*overlay event*) might the final state topology be similar to a semi–muonic beauty decay. Based on filter algorithms designed to suppress non–ep muon background [49] and a visual inspection of a part of the final analysis event sample, the background from this source is found to be negligible.

Background from mis–identified Hadrons

In this analysis, muon identification is based on a signal in the barrel region of the instrumented iron associated with a reconstructed drift chamber track. All other detectable particles are expected to be stopped within the calorimeter. Hadrons coming from the interaction region, however, also produce in rare cases a signal in the central muon system. In this way any process producing two or more jets and including central, high–p_t

hadrons might contribute to the signal sample. Although the probability for a given event to contain a hadron mis–identified as a muon is small, the background due to these *fake muons* turns out to be large. The inclusive dijet cross section, which is dominated by light quark production, exceeds the signal cross section by several orders of magnitude. Even relatively rare configurations can, therefore, result in a sizeable absolute number of background events. It should also be noted that, while the muonic background can be associated with specific physics processes which can be studied separately using dedicated Monte Carlo event samples, this in general is not the case for fake muons. Details on the classification and modelling of the fake muon background can be found in Appendix B.

3.3 Analysis Observables

As discussed above, the selection of dijet events with an identified muon results in a data sample containing both signal and background events. An event–by–event separation of signal and background turns out to be impossible, but the fraction f_b of beauty events can be determined on a statistical basis. The potentially contributing processes can be modelled using, for example, Monte Carlo event generators and their relative contributions can be obtained from a likelihood fit to the shape of distributions of suitably defined observables.

The definition of signal–sensitive observables is based on the large mass or the long lifetime of beauty–flavoured hadrons. In this analysis, two different observables are used, namely the muon transverse momentum relative to an associated jet p_t^{rel} and the muon signed impact parameter δ. For illustration, Figure 3.2 shows, in the xy projection, the vertex region of the same simulated signal event that has already been shown in Figure 3.1. Again, the two beauty jets, one of them containing the decay muon, are clearly visible. The muon flight direction is found to differ significantly from the direction of the muon jet. This indicates a large muon transverse momentum relative to the *mother hadron* producing the muon, which is only possible due to the large mother hadron mass. On the other hand, the long beauty *lifetime* leaves a clear separation of the muon production (*secondary*) vertex from the *ep* interaction (*primary*) vertex. This separation, i. e. the decay length of the beauty hadron, could be measured by reconstructing explicitly both the primary and the secondary vertices. The impact parameter technique, however, which is applied in this analysis, follows a different approach. Instead of using secondary vertex information, the incompatibility of the muon with the *ep* interaction point is quantified by measuring the distance by which the back–extrapolated muon track misses the primary event vertex.

With these introductory remarks, the mass and lifetime signature in semi–muonic beauty decays and the definition of the corresponding analysis observables, p_t^{rel} and δ, are now discussed in more detail.

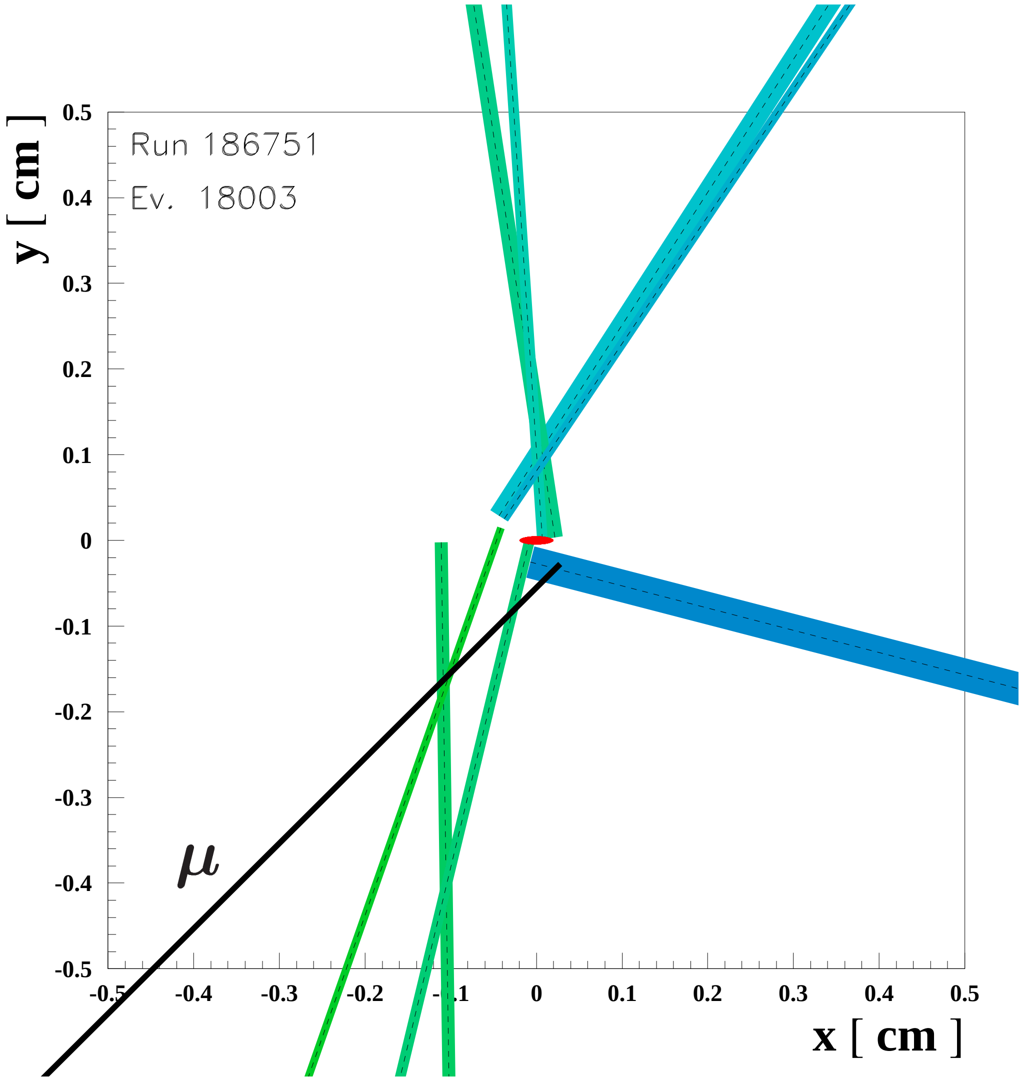

Figure 3.2: *Enlarged vertex region of the signal candidate event already shown in Figure 3.1.*

Mass Signature: The Muon p_t Relative to an Associated Jet

Beauty–flavoured hadrons are considerably heavier than hadrons with charm and light valence quark contribution only (see Table 1.3). This is reflected also in certain aspects of the decay kinematics and topology, which can be exploited experimentally.

Figure 3.3(a) compares the shapes of the spectra of the transverse momentum relative to the beam axis for muons from beauty and charm decays as obtained from the MC event generator AROMA. Beauty production is found to give a significantly harder p_t spectrum than charm production processes. This is partly due to the larger beauty mass, but differences in the hadron production kinematics and the harder beauty fragmentation as compared to charm are also relevant here. As already stated in Section 3.1, using the instrumented iron to experimentally identify muon candidates implies a minimum transverse momentum requirement of about 2 GeV. According to Figure 3.3(a), this results in a considerable enrichment of signal events with respect to the charm background.

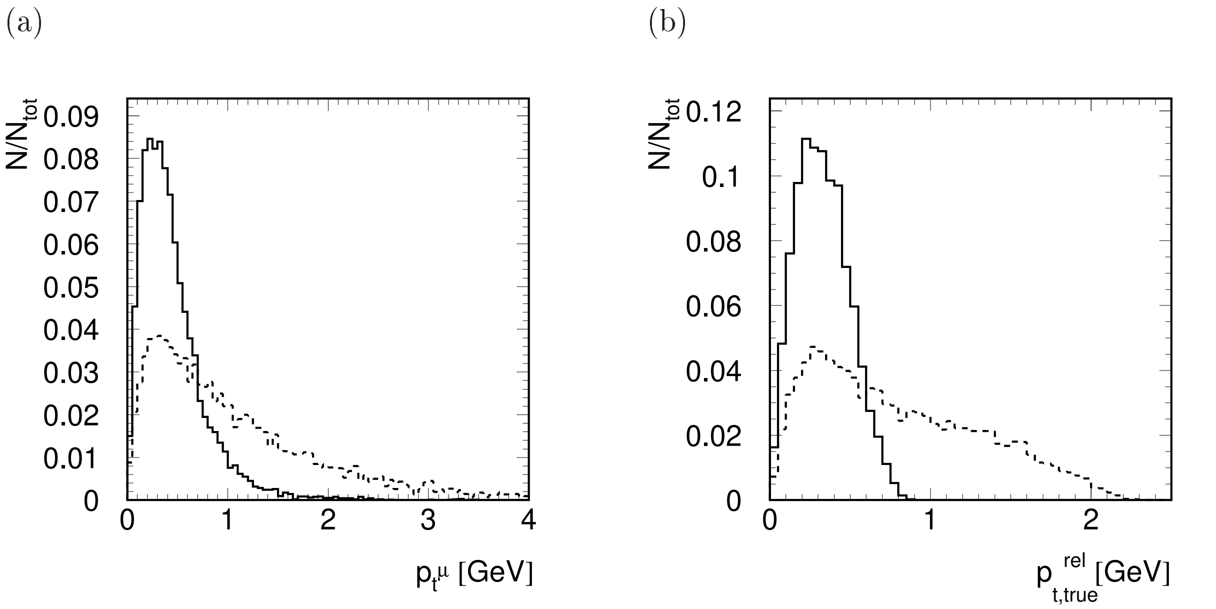

Figure 3.3: *Normalised distributions of (a) the transverse momentum and (b) the transverse momentum relative to the direction of the mother hadron for muons from charm decays (full line) and beauty decays (dashed line) as predicted by AROMA.*

For a quantitative extraction of the signal contribution to the sample, however, better observables can be found, which are not only based on the muon momentum but also consider the mother hadron.

While the muon momentum component parallel to the flight direction of the mother hadron also depends on the hadron production kinematics, the transverse momentum of the decay muon relative to the hadron direction,

$$p_{t,true}^{\mathrm{rel}} \equiv \left|\vec{p}_{t,true}^{\;\mathrm{rel}}\right| = \left|\frac{\vec{p}_{\mu,true} \times \vec{p}_{hadron}}{|\vec{p}_{hadron}|}\right| \quad , \tag{3.1}$$

reflects the hadron mass in a more direct way,[2] resulting in clearly different spectra for beauty and charm decays as demonstrated in Figure 3.3(b). Approximating the hadron direction by a suitably defined jet–based *reference axis* $\vec{A}_{jet}/|\vec{A}_{jet}|$, the corresponding experimental observable is defined as

$$p_t^{\mathrm{rel}} \equiv \left|\vec{p}_t^{\;\mathrm{rel}}\right| = \left|\frac{\vec{p}_\mu \times \vec{A}_{jet}}{|\vec{A}_{jet}|}\right| \quad , \tag{3.2}$$

where $\vec{p}_\mu$ is the reconstructed muon three–momentum. A graphical illustration of this quantity (in the rz–projection) is given in Figure 3.4.

The observable p_t^{rel} was used for the first measurement of beauty production at H1 [50, 51]. In that analysis, the reference axis $\vec{A}_{jet}$ was taken as the jet *thrust axis* with the muon excluded from the thrust calculation.

[2] The p_t^{rel} distribution is closely related to the muon momentum spectrum in the rest frame of the decaying hadron, the kinematic end point being the same for both quantities.

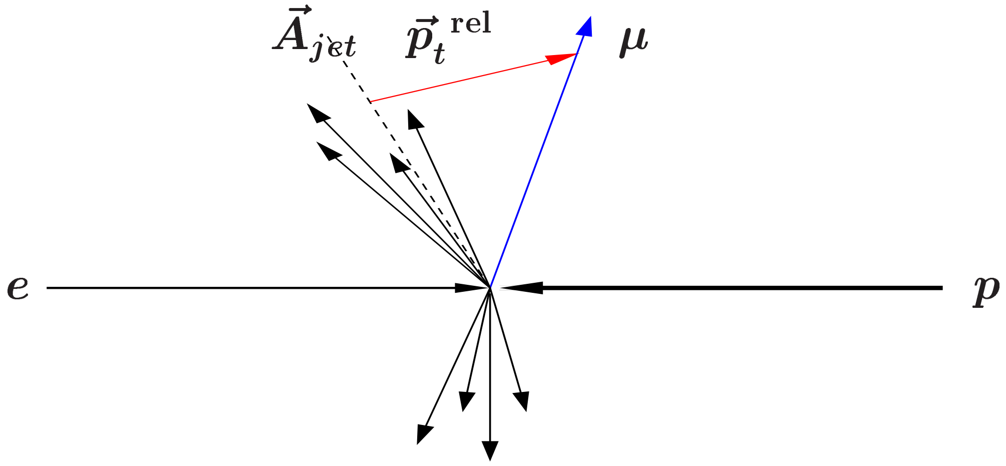

Figure 3.4: *The transverse muon momentum p_t^{rel} relative to an associated jet.*

Lifetime Signature: The Signed Muon Impact Parameter

The large decay length of beauty hadrons arising from their long lifetime can also be used to define beauty–sensitive observables. Table 1.3 lists for various hadrons the *proper decay length* $c\tau$, where τ denotes the lifetime in the rest frame of the decaying hadron, but in the laboratory frame the decay length l accessible by experiment also depends on the hadron *boost* $\beta\gamma \equiv |\vec{p}\,|/m$ via

$$l = c\tau\beta\gamma \quad . \tag{3.3}$$

The probability that an individual hadron of characteristic decay length l traverses at least a laboratory distance L between production and decay is given by

$$\mathcal{P}(L) = \exp\left(-\frac{L}{l}\right) \quad . \tag{3.4}$$

For experimental reasons, lifetime information is extracted only in a plane perpendicular to the beam axis in this analysis. Therefore, only the $r\varphi$–projection

$$L_t = L\sin\theta \quad , \tag{3.5}$$

where θ denotes the polar angle of the decaying hadron, is relevant here.

The *impact parameter* of a particle coming from the hadron decay is the closest distance in $r\varphi$ between the decay particle's trajectory and the production point of the decaying hadron and is given by

$$\delta_{true} = L_t \sin\alpha \quad . \tag{3.6}$$

Here, α is the angle in the $r\varphi$–plane between the hadron direction and the direction of the decay particle. The factor $\sin\alpha$ approximately compensates the boost dependence of L_t.

The lifetime difference between charm and beauty–flavoured hadrons leads to significantly different decay muon δ_{true} spectra, the large δ_{true} region being dominated by beauty events. This is shown in Figure 3.5. For central muons with $p_t > 2$ GeV arising from

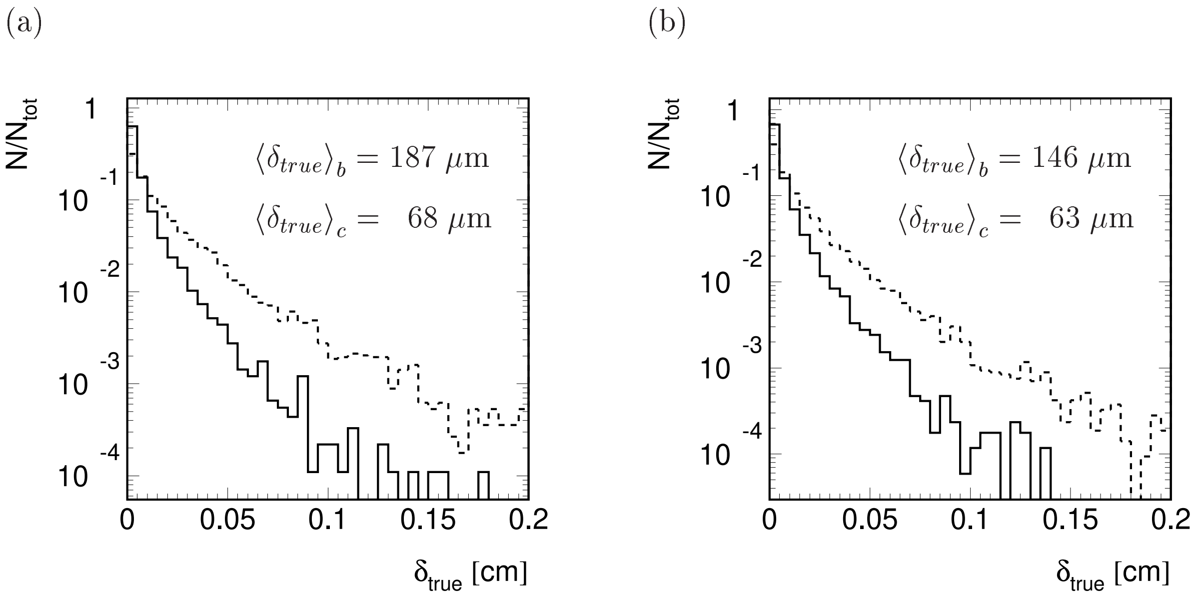

Figure 3.5: *Normalised distributions of the muon impact parameter δ_{true} as obtained from AROMA for semi–muonic charm (full) and beauty (dashed) decays; (a) without cuts and (b) for muons in the range $p_t > 2$ GeV, $35^\circ < \theta < 130^\circ$.*

beauty decays, the mean of the impact parameter distribution is predicted to be at about 150 μm, whereas for charm decays $\langle\delta_{true}\rangle \approx 60$ μm, see Figure 3.5(b).

In order to construct an experimental observable corresponding to δ_{true}, the hadron production vertex is taken to be the reconstructed primary event vertex and the flight direction of the decaying hadron is approximated by a jet–based reference axis as already discussed for $p_t^{\rm rel}$ in the previous section. While δ_{true} is by definition a positive quantity, it turns out to be useful to define a sign for the corresponding experimental observable. The resulting *signed muon impact parameter* δ is defined as follows:

- The magnitude of the impact parameter is given by the $r\varphi$–distance of closest approach of the reconstructed muon track to the reconstructed primary event vertex,

$$|\delta| = \left|\vec{d}_{ca}^{\,\mu,\rm pv}\right| \quad , \tag{3.7}$$

  where $\vec{d}_{ca}^{\,\mu,\rm pv}$ denotes the vector connecting in the $r\varphi$–plane the primary event vertex with the muon track at the point of closest approach, see Figure 3.6(a).

- Taking the jet containing the muon as reference, a sign can also be assigned to the impact parameter. The sign is positive if the intercept of the muon track with the jet in the $r\varphi$–projection is downstream of the primary vertex, and negative otherwise. Figure 3.6(b) gives a schematic illustration of this sign convention. Formally, this definition reads

$$sign(\delta) = \begin{cases} = +1 & \text{if} \quad |\Delta\varphi| \leq \pi/2 \\ = -1 & \text{if} \quad |\Delta\varphi| > \pi/2 \end{cases} , \text{ where } \Delta\varphi = \text{acos}\left(\frac{\vec{A}_{t,jet} \cdot \vec{d}_{ca}^{\,\mu,\rm pv}}{\left|\vec{A}_{t,jet}\right| \left|\vec{d}_{ca}^{\,\mu,\rm pv}\right|}\right) \tag{3.8}$$

  and $\vec{A}_{t,jet}$ is the $r\varphi$–projection of the jet–based reference axis $\vec{A}_{jet}$.

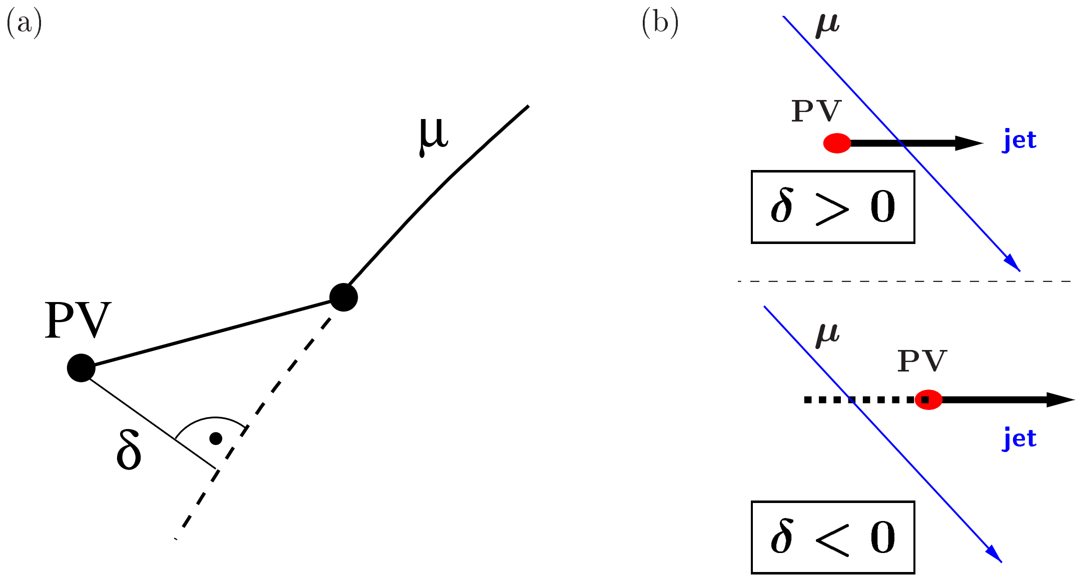

Figure 3.6: *Definition of the signed impact parameter δ: (a) magnitude and (b) sign. PV denotes the primary event vertex.*

For muons originating from the primary vertex the δ spectrum will be symmetric around zero, the width of the distribution reflecting the finite track and vertex reconstruction resolutions. Decays of long–lived particles are signalled by an excess at positive δ values. The region of large positive impact parameters is expected to be dominated by muons from beauty decays.

The impact parameter method is based on the reconstruction of the muon track and the event primary vertex, which is assumed to be the production vertex of the heavy hadron. In contrast to an explicit decay length analysis, no knowledge of the hadron decay vertex is required and, therefore, a reconstruction of secondary event vertices is not necessary. Also, the impact parameter depends only weakly on the boost of the decaying hadron. In this sense δ probes the proper lifetime of the decaying hadron in a more direct way than the decay length, which is proportional to the hadron boost, cf. Equation 3.3.

Correlation of δ and p_t^{rel}

Figure 3.7 shows the correlation of δ_{true} and $p_{t,true}^{rel}$ for semi–muonic beauty and charm decays ($p_t^\mu > 2$ GeV) as obtained from the AROMA event generator without considering any detector effects. As has been already discussed for the one–dimensional distributions, the signal extends to larger values in both δ_{true} and $p_{t,true}^{rel}$ than the charm background. Figure 3.7(a) does not indicate, however, any obvious correlation between the two quantities. In particular, a large value for one observable does not necessarily imply a large value for the other observable. The signal can, therefore, be enriched by selecting events from the tail of either observable, with these two beauty–enriched event samples being sufficiently independent from each other, i. e. the two observables reinforce each other in discriminating beauty from background processes.

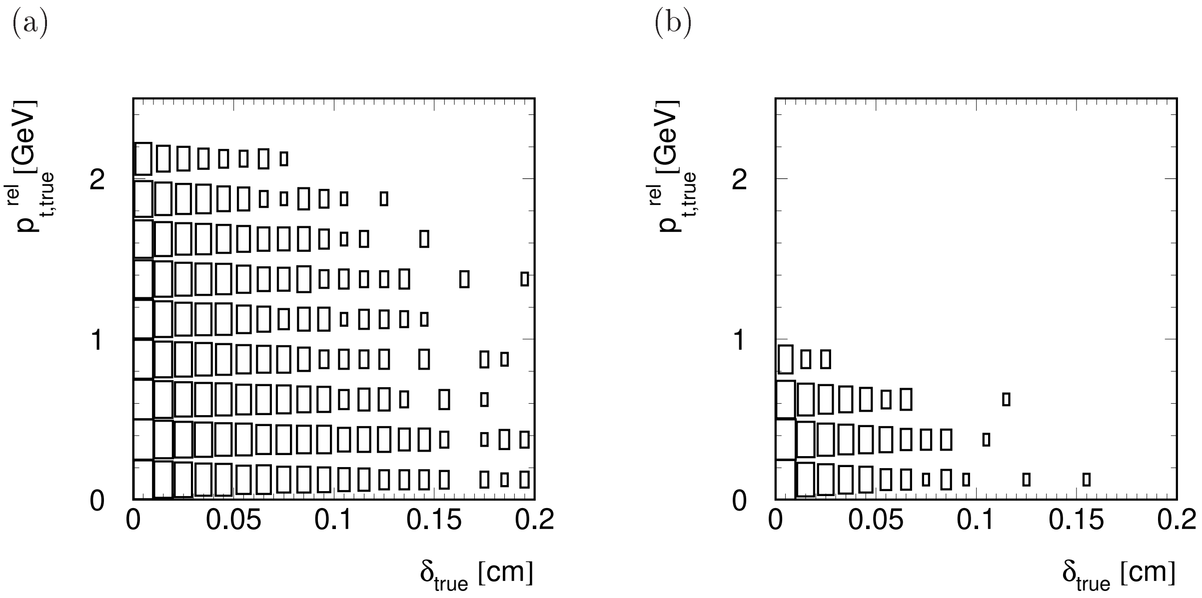

Figure 3.7: *Correlation of δ_{true} and $p^{\rm rel}_{t,true}$ for semi–muonic (a) beauty and (b) charm decays as generated by AROMA.*

Experimental Requirements

In order to use the observables defined in the previous section to determine the beauty content of a selected sample of dijet events containing a muon candidate, all quantities entering the calculation of $p_t^{\rm rel}$ and δ need to be reconstructed with sufficient precision. This turns out to be an experimental challenge, especially for the impact parameter analysis.

The typical δ_{true} values of 150 μm and 60 μm for muons from charm and beauty decays respectively (see Figure 3.5) require an impact parameter resolution of the order of 100 μm in order to separate the signal from the charm background via this observable. The intrinsic $r\varphi$ hit resolution of the central drift chambers being about 150 μm, clearly the vertex detector is needed for an impact parameter based measurement of beauty production. In this analysis, CST information is used in the reconstruction of both the muon track and the primary event vertex.

The jet reference axis is used in the calculation of both δ and $p_t^{\rm rel}$. The $p_t^{\rm rel}$ resolution depends directly on how well the jet reflects the direction of the heavy hadron. In the impact parameter distribution a degraded jet angle resolution will lead to an increased number of signal events with large δ_{true} reconstructed with negative sign, thus making long lifetime effects indistinguishable from badly modelled resolution.

For the $p_t^{\rm rel}$ analysis, also a good modelling of the energy flow within the jet is of relevance.

3.4 Analysis Strategy

To summarise, the analysis is based on the following procedure: Dijet events containing a central, high–p_t muon candidate are selected, considering in particular high quality requirements for the reconstruction of the muon track, the jet axis and the primary event vertex. This is done for H1 data taken during 1997 and for Monte Carlo simulated events modelling the signal and relevant background processes. The relative contributions of the different processes are obtained from likelihood fits to the muon δ and p_t^{rel} spectra, taking the normalisation from the data. Correcting for luminosity, detector acceptance and selection efficiency, the relative beauty contribution is transformed into a beauty production cross section which can be compared to theoretical predictions.

While p_t^{rel} has been used already in a previous measurement of beauty production at H1 [50, 51], the measurement presented in this thesis is the first to be based (also) on the impact parameter method.[3] A new analysis based on an independent data set and using δ as the only observable can serve as a cross check of the previous measurement and introduces the impact parameter method in a well–controlled way. Having established consistency between δ and p_t^{rel}, a combined analysis using the two observables simultaneously can be performed. As δ and p_t^{rel} probe beauty in a fairly independent way, this combination is expected to result in a measurement which is clearly improved with respect to analyses based on only one of the observables.

One way in which this can be used to extend the scope of previous measurements is to study previously unaccessed kinematic regions. While the earlier measurements of beauty production in ep scattering have been performed in the photoproduction regime, the aim of this analysis is to also perform the first measurement of the beauty cross section in deep inelastic scattering.[4]

[3] Here, an earlier feasibility study [44] provided a valuable starting point.

[4] In parallel to this work, the DIS process $ep \to bX \to D^{\star}X$ has also been analysed with H1, see [52].

Chapter 4

Event Reconstruction and Selection

This chapter describes the relevant steps of the reconstruction and selection of the events to be used in the beauty production cross section measurement. The basic selection criteria, including trigger requirements, are defined first. They provide an *ep* event sample that is sufficiently clean to be used as starting point for the subsequent analysis. This is followed by a detailed discussion of the reconstruction and selection procedure for muon candidates, the primary vertex and jets. After defining experimentally the kinematic ranges for the beauty production measurements in photoproduction and DIS, the chapter concludes with a summary of the selection chain and the resulting event samples.

4.1 Definition of the Data Set

The data used in this measurement were collected with the H1 detector between April and October 1997.[1] As the central silicon tracker is an indispensable tool for this measurement, no data taken prior to the full CST commissioning in spring 1997 can be considered. The restriction to run numbers below 200407 results in a homogeneous data set recorded with a stable experimental setup. In the following, further selection criteria are listed which ensure that only data obtained with a fully operational detector under well–defined trigger conditions are considered for the later analysis.

Detector Status

A *run quality* classification based on the available slow control and detector status information is performed online. In this analysis, only runs with *high* and *medium quality* are considered. A *poor quality* is assigned if at least one major detector component was found to be not fully operational and the corresponding runs are rejected. An additional event selection on the basis of the information on the detector status (voltages, readout, trigger) is used to ensure that only events are considered for which all subsystems relevant for this analysis (namely CST, CJC, MWPC, BDC, digital muon system, LAr calorimeter, SpaCal, ToF devices and the luminosity system, cf. Chapter 2) were working properly.

[1]This corresponds to run numbers 185631 to 200407.

Analysis Subtriggers

The selected events are required to fulfil at least one of the L1 subtrigger conditions listed below. For a more detailed description of the individual trigger elements see Section 2.5.

- **s19:** The subtrigger condition s19 is designed to detect high transverse momentum muons in the central region of the detector. A signal in the barrel region of the digital muon system is combined with a charged track signature in the jet chamber in coincidence with a significant peak in the zVtx trigger histogram. In standard H1 trigger element notation this reads[2]

  $$\texttt{(DCRPh\_Tc} \wedge \texttt{DCRPh\_TNeg} \wedge \texttt{DCRPh\_THig)} \wedge \texttt{zVtx\_sig>1} \wedge \texttt{Mu\_Bar}\ .$$

- **s2/s61:**[3] Designed for inclusive DIS events, this subtrigger requires a high energy deposition in the backward calorimeter, together with track and vertex activity in the central region:

  $$\texttt{DCRPh\_THig} \wedge \texttt{zVtx\_sig>0} \wedge \texttt{(SPCLe\_IET>2} \vee \texttt{SPCLe\_IET\_Cen\_3)}\ .$$

- **s83:** This subtrigger condition is designed to select photoproduction events, where the scattered positron is detected in the electron tagger ET33. The photon detector is used as a veto counter against Bethe-Heitler processes. A coincidence with central track and vertex activity is required to suppress non-ep background:

  $$\texttt{DCRPh\_Tc} \wedge \texttt{zVtx\_sig>1} \wedge \texttt{LU\_ET} \wedge \texttt{!LU\_PD\_low}\ .$$

- **s84:** In complete analogy to the condition s83, but using a different electron detector, this subtrigger selects ET44 tagged photoproduction events:

  $$\texttt{DCRPh\_Tc} \wedge \texttt{zVtx\_sig>1} \wedge \texttt{LU\_ET44} \wedge \texttt{!LU\_PD\_low} \wedge \texttt{!LU\_WatVet}\ .$$

In addition to the trigger elements given above, all subtriggers include various veto conditions against non–ep background. These are based on, for example, event timing information provided by the ToF devices and have a negligible inefficiency for ep interaction events.

Event samples

Several different event samples are needed for the beauty cross section measurement. All are based on the selection of dijet events with central, high–p_t tracks within a well–defined kinematic region (either photoproduction or low–Q^2 DIS), see below. There are, however, differences in the trigger and muon identification requirements.

[2]Here, $\wedge$, $\vee$ and ! denotes a logical AND, OR and NOT respectively.

[3]At the beginning of 1997 data–taking this subtrigger condition was labelled 's2'. Starting with run number 193433 the name was changed to 's61'.

- *Signal* or *muon data* samples are obtained by selecting identified muons from events recorded with H1 in 1997. For the photoproduction analysis the events are required to fulfil the L1 subtrigger condition s19, whereas for the DIS analysis the subtrigger s2/s61 is used. The same selection on simulated semi–muonic beauty decay events (obtained from the AROMA program) gives corresponding *signal MC* samples.

- Omitting in the signal selection the muon identification and rejecting explicitly events containing identified muons results in useful control samples, which are dominated by light flavours and referred to in the following as *(inclusive) tracks* or *hadrons*. Here, muon system-independent subtriggers are used, namely s83, s84 (photoproduction) and s2/s62 (DIS). Track samples are selected from both H1 data and MC simulation. The simulated γp and DIS events are obtained from the PYTHIA and DJANGO programs respectively.

- It is often useful to compare H1 data distributions to a *combined MC* prediction. Here, beauty, charm and fake muon MC events passing the signal selection are combined according to the decomposition of the H1 data into signal and background contributions as obtained in the later measurement (see Chapter 5). Beauty and charm production is simulated with AROMA. For the fake muon background PYTHIA (γp) and DJANGO (DIS) are used.

More detailed information on all these event samples can be found in Section 4.8. If not stated otherwise, the distributions shown in this chapter are obtained from the photoproduction samples.

4.2 Muon Identification

Muons are identified in the central tracking chambers and the instrumented iron. In a first step track hypotheses are formed independently for both systems. Afterwards a test is performed to find if any combination of a central track and an iron track segment is compatible with a single particle trajectory.

In order to resolve ambiguities in the reconstruction and to ensure a sufficiently high reconstruction quality, various selection cuts have to be applied. In this analysis this is done using a standard H1 software package [53], which extracts the relevant information from the event data and provides the framework for a flexible implementation of selection criteria. The selection is described in the following and a cut summary is given in Table 4.1.

Selection of Drift Chamber Tracks

Vertex–fitted tracks as measured with the CJC, CIZ, COZ and/or, depending on the polar angle, the forward tracking system are selected and are referred to in the following as *drift chamber tracks*. These tracks are parametrised by the inverse transverse momentum $1/p_t$, the sign of the electromagnetic charge and the polar and azimuthal angles at the vertex

Selection of drift chamber tracks		**Muon identification in the iron**	
parameter	selection cut	parameter	selection cut
transv. momentum	$p_t > 2$ GeV	radial distance to prim. vertex	$\rho < 100$ cm
polar angle	$35° < \theta < 130°$	distance in z to prim. vertex	$z_o < 100$ cm
start radius	$R_{start} < 35$ cm	number of iron layers	$N_{il} \geq 2$
track length	$l_{track} > 22$ cm	index of first (last) iron layer	$i \leq 5$ (≥ 2)
minimum probability for drift chamber–iron combination: 0.001			

Table 4.1: *Summary of muon selection cuts.*

(θ and φ). Together with the vertex coordinates this gives a unique description of the track, which is stored in the DST BOS bank DTRA. One physical particle can lead to multiple track hypotheses, for example if several event vertices are found and a track is successfully linked to more than one vertex. In the acceptance overlap region of the central and the forward tracking chambers parallel hypotheses are obtained also by using either only the forward tracker, only the central tracker or by combining the information of the two systems. Correspondingly, the hypotheses are labelled as *central, forward* or *combined* tracks.

In this analysis, an improved track measurement with the vertex detector is necessary. Central tracks which are found well within the the polar angular acceptance of the CST ($35° < \theta < 130°$), also referred to as *CJC tracks* in the following, are selected. As the jet chamber resolution is not sufficient to resolve the decay length of beauty hadrons, hypotheses associated to the reconstructed primary event vertex are preferred. A cut of 2 GeV is imposed by muon identification criteria and also suppresses contributions from multiple scattering in the impact parameter resolution. In most cases a sufficiently precise determination of the parameters for short track segments is not possible, so a cut on the minimum track length of 22 cm is applied. To later reliably associate CST information with the extrapolated drift chamber track, hit information within the CJC1 is desirable. It is, therefore, required that the start radius of the track, i. e. the radial position of the innermost CJC hit, is not larger than 35 cm.

Identification in the Instrumented Iron

The method of track reconstruction in the instrumented iron is described in [45]. The resulting parameters are stored together with relevant additional information in the bank DMUO. Only track segments found in the barrel region are selected because the later analysis will be restricted to the CST acceptance region anyway. At least two hits behind iron plates are required; the innermost hit has to be within the first two layers. The extrapolated track is also demanded to point roughly back to the interaction region with a maximum separation from the nominal interaction point of 1 m and 2 m in $r\varphi$ and z respectively.

Combination of Drift Chamber and Iron Tracks

All high momentum drift chamber tracks are extrapolated into the instrumented iron. If a reconstructed iron track segment is found sufficiently close, a probability that both tracks stem from a single particle is calculated.

All pairs of DTRA–DMUO tracks passing the above selection cuts are considered. If a drift chamber track was assigned to several iron tracks, only the highest probability link is used. Finally, all drift chamber tracks which have an iron link with a probability higher than 10^{-3} are selected and these are referred to in the following as *muon candidates*.

Performance

In Figure 4.1 the muon candidate φ spectrum is shown as obtained from the H1 data and combined MC samples. The drop in the distributions in the negative φ region reflects CJC tracking inefficiencies due to broken wires, high voltage problems and aging effects in part of the lower half of the chamber. The simulation of the CJC response close to the regions with degraded efficiency turns out to be difficult. This is reflected in an imperfect description of the muon candidate φ spectrum by the Monte Carlo in this region, which is taken into account in the later cross section measurement by globally correcting the simulated signal selection efficiency by -9%.

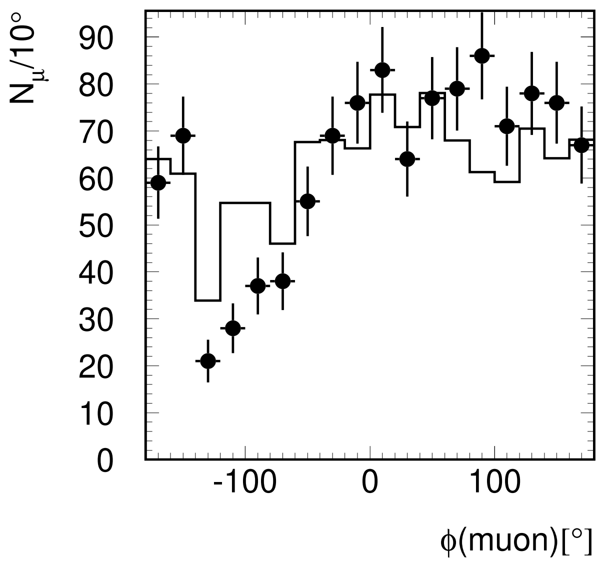

Figure 4.1: *φ distribution for selected muon candidates for H1 data (points) and AROMA beauty MC (histogram).*

Figure 4.2 shows that the combined MC provides an overall acceptable description in terms of the muon transverse momentum and polar angle. There is, however, a clear tendency of the MC prediction to be below the data for small p_t and small θ. In contrast to the φ distribution, these spectra do not only contain information on the detector description, but are also sensitive to the physics modelling. A possible explanation for the observed deviations are resolved processes in the H1 data, see Section 1.3.2 and Section 1.5.1, which are not provided by the AROMA program that is used here to simulate heavy flavour production. In these processes only a fraction $x_\gamma < 1$ of the photon's momentum enters the hard subprocess, and the final state is expected to be more forward–directed compared to direct photon interactions.

It should be noted that these figures compare only the shape of the distributions and do not test the absolute muon identification efficiency ϵ_μ. As the selected sample of muon candidates contains a significant fraction of mis–identified hadrons (see Section 3.2), which cannot be distinguished from real muons, it cannot be used to measure ϵ_μ. In $J/\psi \to \mu^+\mu^-$ analyses, however, ϵ_μ can be determined by selecting track pairs for which the invariant mass is compatible with the J/ψ mass, requiring a muon signal for one of the tracks and studying the identification efficiency of the other. Results based on 1997 and muon selection criteria similar to those used in this analysis are discussed, for example, in [54]. Good agreement between H1 data and MC simulation is found. In spite of some differences in the decay muon kinematics, it is a reasonable assumption that this result holds also for this analysis, such that ϵ_μ can be taken from the simulation.

(a) (b)

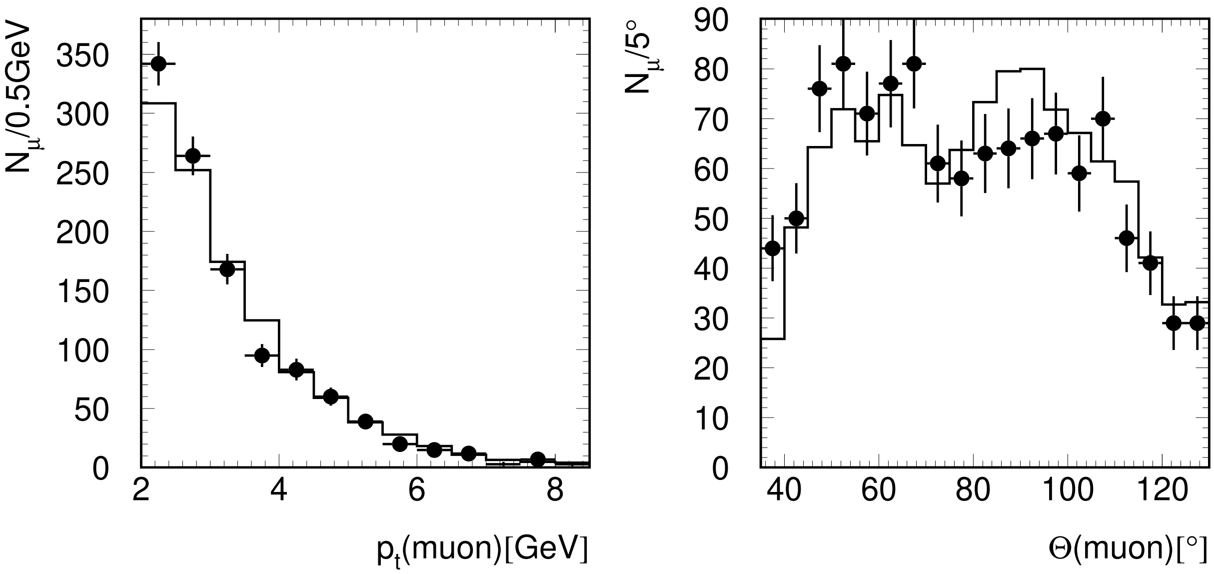

Figure 4.2: *Muon (a) p_t and (b) θ for H1 data (points) and combined MC samples (histograms).*

4.3 Improved Track Reconstruction Using the CST

The muon transverse momentum relative to an associated jet can be reconstructed with sufficient accuracy using drift chamber information alone, whereas the impact parameter method relies on a precise track measurement in the vertex region, which can only be achieved with the vertex detector CST.

With the CST, which consists of only two layers, tracks cannot be recognised without external constraint. In order to obtain CST–improved tracks, vertex detector and drift chamber information need to be combined. Currently this is done starting from reconstructed drift chamber tracks, either before or after a fit to a reconstructed event vertex has been performed, and CST hits. The latter are available as *clusters*, which are reconstructed separately for the n and the p–side and thus contain only $r\varphi$ and z information respectively, or three–dimensional *space points* resulting from the combination of associated n and p–side clusters.

When this analysis work started, there was already software available for the combination of CST hits and drift chamber tracks [44], which had been successfully used for various purposes. It turned out, however, that certain aspects of this procedure, which in the following will be referred to as the *standard method*, are problematic for the impact parameter analysis. In order to overcome these problems, an alternative (*new*) method for the CST–drift chamber combination has been developed.

This section outlines those features of the new method which are relevant for the impact parameter analysis, i. e. the improved reconstruction in the $r\varphi$–plane for individual tracks.[4] It should be noted, however, that, after the first implementation of the new CST–drift chamber combination was done within the framework of this analysis, it has since been developed into a general purpose software package (CSTLIN) which is applicable to all central tracks in a given event (providing also improved z information) and which has recently become part of the standard H1 event reconstruction.[5] A detailed documentation can be found in [58].

Standard Method

Following the standard procedure, CST–improved parameters for a given drift chamber track are obtained in two steps, which are performed separately for $r\varphi$ and z–related track parameters.

1. *Linking:* CST space points are associated to the (vertex–fitted) drift chamber track. This is done independently for the two vertex detector layers.

2. *Track fit:* Improved track parameters are determined in a fit combining information from the (non–vertex fitted) drift chamber track and the linked CST hits.

[4] A first performance study based on an early implementation of this concept is documented in [55].

[5] The method has also been successfully used in a lifetime–based H1 analysis of charmed meson production [56, 57].

Based on an AROMA MC sample of semi–muonic beauty decays, Figure 4.3 shows, as a function of the true impact parameter, the efficiency for a successful high–quality combination of non–vertex fitted tracks, fulfilling the θ and p_t cuts described in Section 4.2, with at least one hit in each vertex detector layer. The efficiency is found to degrade significantly towards large δ_{true} values, i. e. in the very region where the signal is expected to dominate.

This unwanted feature of the standard method is due to the use of the extrapolated vertex–fitted drift chamber track in the $r\varphi$–linking step, which is motivated by the significantly better precision in the region of the CST detector compared to the non–vertex fitted track. For a given CST layer, hits found at separations less than five times the track extrapolation error from the track intersect are considered as candidates for the linking. As illustrated by Figure 4.4(a), this is problematic for large δ_{true} values, for which the reconstructed vertex–fitted track is likely to deviate significantly from the true particle trajectory thus increasing the probability of assigning a wrong hit (due to electronic noise or other tracks) or of finding no hit candidate at all. Both cases reduce the efficiency to obtain a high quality CST–drift chamber combination in the subsequent track fit.

Although the probability to find any associated CST information can be increased by enlarging the search window around the track, this does not solve the problem of incorrectly assigning hits stemming from noise or other tracks. Due to the superior CST resolution, wrong hits are likely to severely distort the CST–CJC–combined track. In order to obtain a CST–drift chamber combination with both a high purity of correct links and a sufficiently high efficiency also in the large impact parameter region, conceptual changes are needed.

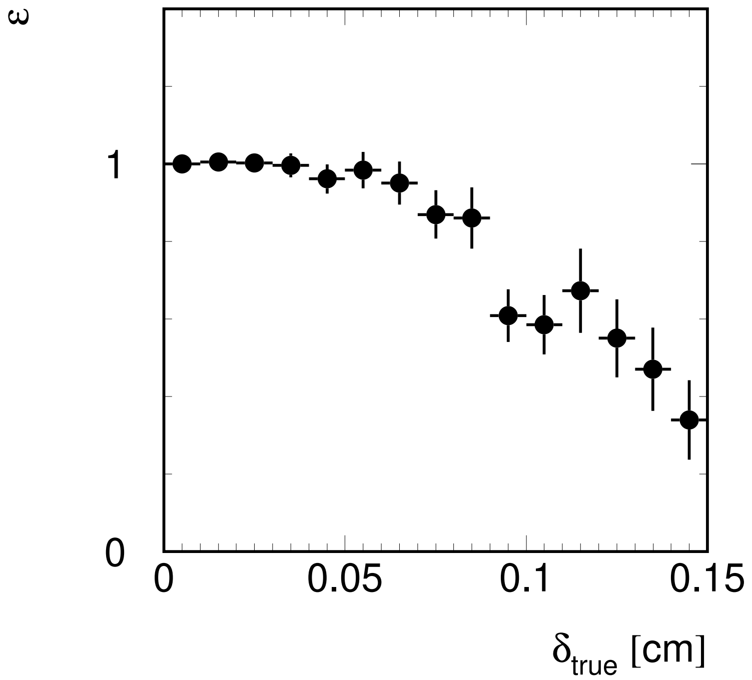

Figure 4.3: *CST–drift chamber combination efficiency for muon candidates selected from AROMA signal MC as a function of the true impact parameter, obtained with the standard method. The distribution has been normalised such that $\epsilon(0) = 100\%$.*

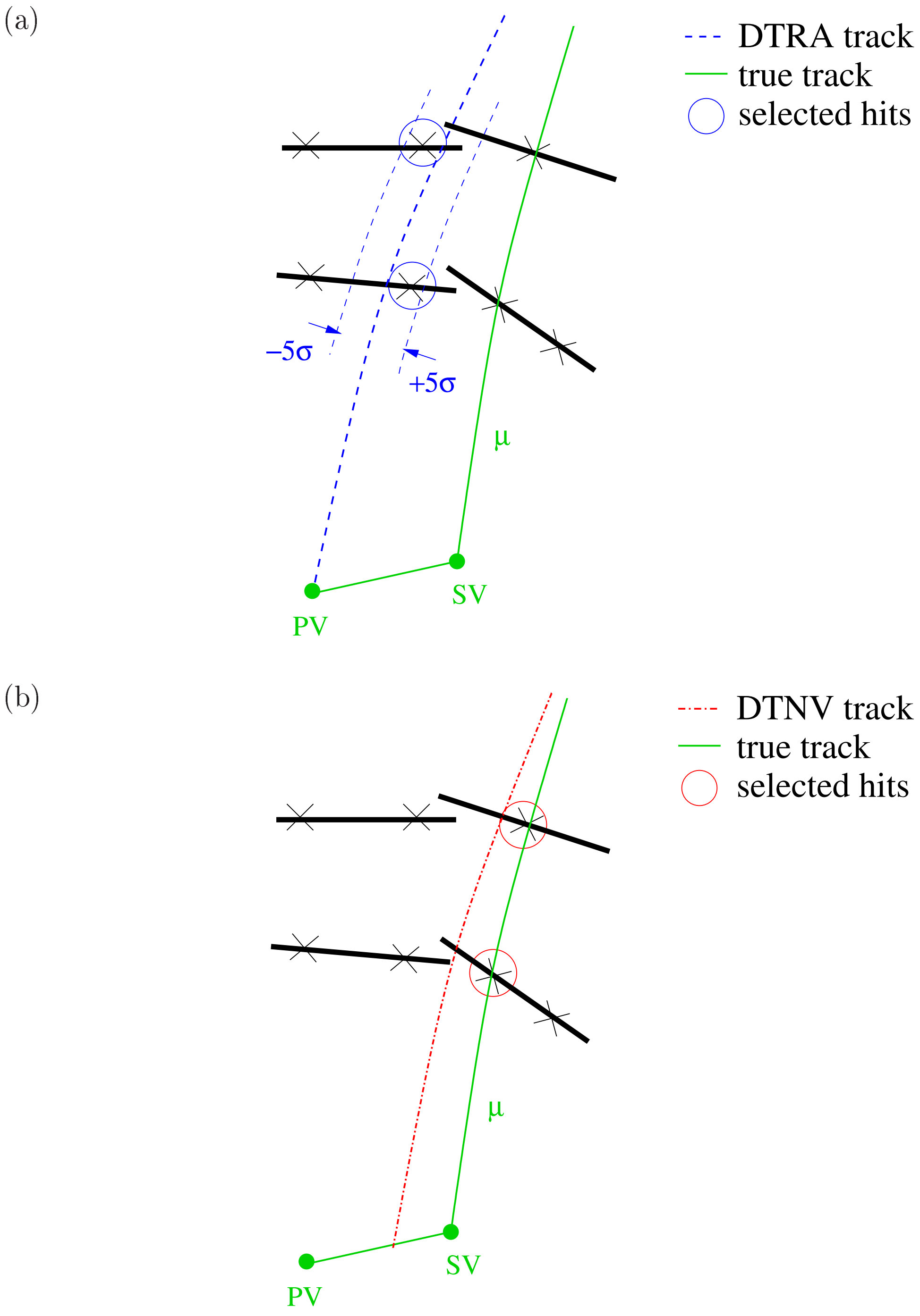

Figure 4.4: *Association of CST hits to a muon drift chamber track for a large separation of the primary event vertex (PV) and the secondary muon production vertex (SV) using (a) the standard method and (b) the new method. In the standard method, only CST hits within a $\pm 5\sigma$ window around the vertex–fitted (DTRA) track are considered, making it likely to assign wrong (or no) hits if the muon impact parameter is large. The new method does not rely on a primary vertex constraint and uses non–vertex fitted (DTNV) tracks instead, thus avoiding a drop of the efficiency for a high–quality CST–drift chamber association in the large impact parameter region.*

New Method

Having identified the vertex constraint as a problematic feature of the standard method, the new method uses instead non–vertex fitted tracks as input. These are stored in the BOS bank DTNV using as parameters the track curvature $\kappa \sim 1/p_t$, the $r\varphi$ distance–of–closest–approach $d_{ca,0}$ to the nominal interaction point as well as the azimuthal angle φ_0, polar angle θ_0 and z-coordinate corresponding to $d_{ca,0}$.

CST hits in the inner and outer layers are linked to the drift chamber track simultaneously, i. e. the hit combination of inner and outer layers is chosen which maximises the total link probability. This is superior to a separate linking in the inner and outer layers, because obviously all hits from one track are correlated in their positions, and is expected to work reliably also for large δ_{true} values, see Figure 4.4(b). As a result, the association of CST hits to the drift chamber track (linking) and the determination of the improved track parameters (track fit) are performed in one step.

Another conceptual change with respect to the standard method is the use of CST clusters instead of space points, leading to a further separation of $r\varphi$ and z information. This way CST–improved $r\varphi$ track parameters can be obtained using p–side information alone without being affected by possible n–side inefficiencies.

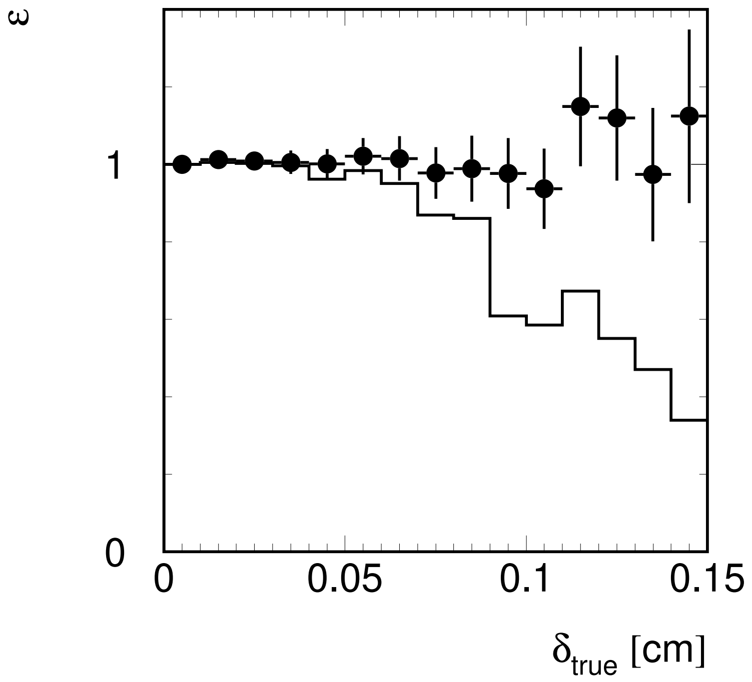

Figure 4.5: *CST–drift chamber combination efficiency for muon candidates selected from AROMA signal MC as a function of the true impact parameter, obtained with the new method (points) and the standard method (histogram). The distributions have been normalised such that* $\epsilon(0) = 100\%$.

Specifically, the CST–improved $r\varphi$–parameters for the selected muon candidates are obtained according to the following procedure: For the muon DTNV track and all possible combinations of p–side hits from the inner and the outer CST layers, a circle track fit is applied which minimises the χ^2 function

$$\chi^2 = (\vec{T} - \vec{T}_{DC})^t \, V_{T_{DC}}^{-1} \, (\vec{T} - \vec{T}_{DC}) \;+ \sum_{(\text{i. l. hits } i)} \frac{d_{i\vec{T}}^2}{\sigma^2(d_{i\vec{T}})} + \sum_{(\text{o. l. hits } j)} \frac{d_{j\vec{T}}^2}{\sigma^2(d_{j\vec{T}})} \;, \qquad (4.1)$$

where the two sums run over the inner and outer layer hits respectively. $\vec{T} = (\kappa, \varphi_0, d_{ca,0})$ denotes the $r\varphi$ track fit parameters, $\vec{T}_{DC}$ the DTNV parameters and $V_{T_{DC}}$ the covariance. $d_{j\vec{T}}$ and $\sigma(d_{j\vec{T}})$ are the $r\varphi$–separation between the track and the hit and its error, as calculated from the hit covariance, respectively. The hit combination which minimises the χ^2 of the track fit is selected. Solutions with a maximal number of CST hits are preferred but must have a reasonable χ^2. When no reasonable solutions are found with hits in both layers, solutions with hits from only one layer are also taken into consideration.

As can be seen from Figure 4.5, the CST–drift chamber combination efficiency, unlike for the standard method, does not decrease in the high impact parameter region. Again, a high probability link with at least one hit in each CST layer is required here. Further examples of quality checks, also involving the CST–improved primary event vertex, can be found below.

Selection and Performance

For the muon candidates used in the later analysis a high–quality $r\varphi$–combination of the drift chamber track with at least one hit in each CST layer is required. A quantitative quality criterium is obtained by translating the χ^2 (4.1) into a track fit probability $\mathcal{P}_{\text{track}}$ according to

$$\mathcal{P}_{\text{track}}(\chi^2, N) = \frac{1}{\sqrt{2^N}\Gamma(N/2)} \int_{\chi^2}^{\infty} e^{-\frac{1}{2}t} t^{-\frac{1}{2}N-1} dt \;, \qquad (4.2)$$

where N denotes the number of linked CST hits, and requiring

$$\mathcal{P}_{\text{track}} > 0.1 \;. \qquad (4.3)$$

In [42], based on cosmic muon data recorded in 1997, the CST p–side single hit efficiency is determined to be 97%. Following the same method, this value is found to be well reproduced by the simulation.

In contrast to the CST hit efficiency, the $\mathcal{P}_{\text{track}}$ distribution is not well described by the standard MC simulation, see Figure 4.6(a), resulting in an unacceptably large difference in the probability cut efficiency between H1 data and MC. In Figure 4.6(b), the width of the δ distribution is also visibly different for measured and simulated tracks.

(a)

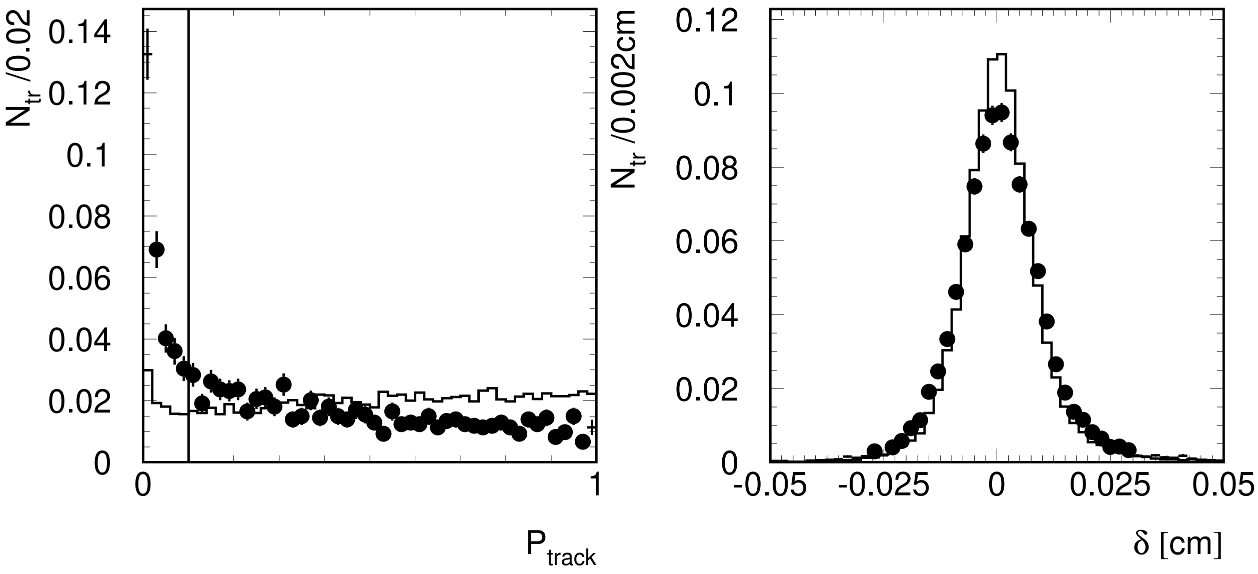

(b)

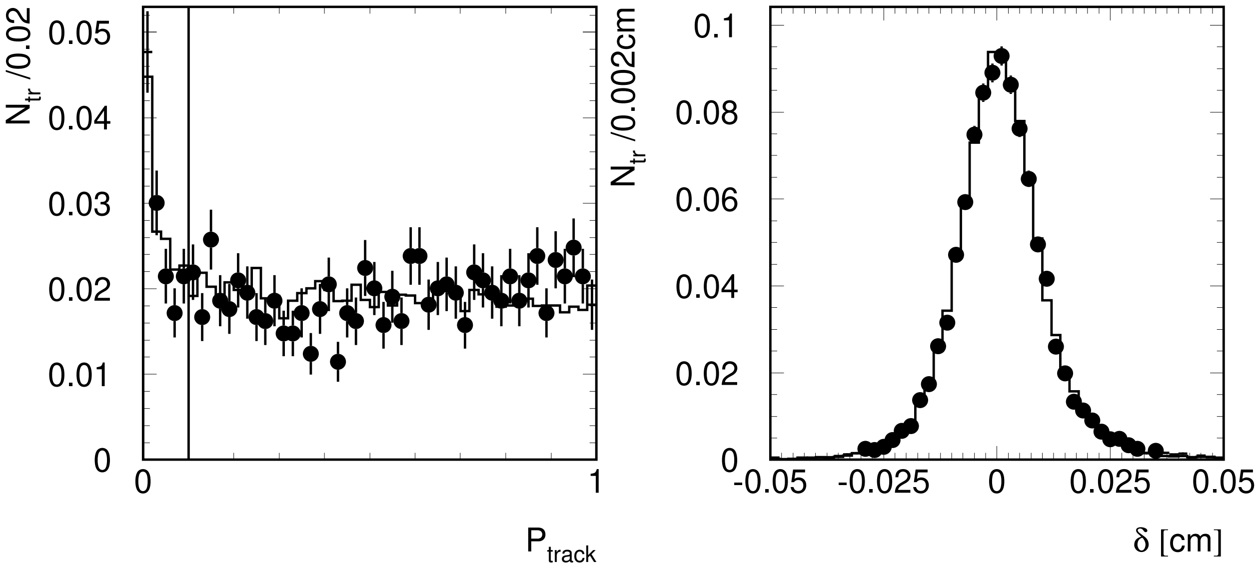

Figure 4.6: *Left: CST–drift chamber combination probability for identified muons from the H1 data (points) and AROMA beauty MC (histograms). Right: Impact parameter distributions for inclusive tracks from H1 data (points) and PYTHIA MC (histograms). The distributions are shown (a) before and (b) after applying the corrections to drift chamber tracks and CST hits which are described in the text.*

The input to the CST–drift chamber combination is, therefore, corrected in the following way:

- *CST hit resolution*: An additional Gaussian smearing of 10 μm is applied to the simulated CST $r\varphi$ cluster position.
- *Drift chamber track resolution*: In the MC simulation, the reconstructed values of the $r\varphi$–related drift chamber track parameters are changed such that the difference with respect to the true values increases by 60%. Also, for both H1 data and MC simulation the corresponding covariances are scaled by a factor 1.6.

Both types of corrections turn out to be necessary. In all following comparisons of H1 data and Monte Carlo as well as in the later measurement, this "smeared" version of the simulation has been used.

The size of the corrections have been obtained by optimising the MC description of the H1 inclusive track sample in terms of the $\mathcal{P}_{\text{track}}$ distribution and the impact parameter resolution. As illustrated in Figure 4.6(c) and (d), after the correction reasonably good agreement of H1 data and MC is achieved for both distributions. The central width of the δ distribution is found to be 82 μm for both the H1 data and the MC simulation. Assuming the contribution from secondary particles to the inclusive track samples to be negligible, this is a direct measure of the impact parameter resolution.[6] Still, some imperfections in the tracking simulation remain. These reflect in a relative overestimation of the CST–drift chamber combination efficiency, which for the above selection criteria is determined from the H1 data to be 73%, by about 8%.

While this pragmatic approach using global correction factors is found to give satisfactory results for the purposes of this analysis, for future high–statistics measurements it is probably necessary to understand and possibly eliminate the underlying effects on a deeper level, i. e. in terms of the detector alignment and other parameters entering the track reconstruction. This has been followed up in parallel to this work, and systematic mis–calibration and mis–alignment effects have been found which are consistent with the size of corrections applied in this analysis. For further details see [59].

Further performance studies of the new CST–drift chamber combination scheme include, for example, a more detailed investigation of the impact parameter resolution, which is of particular relevance for this analysis.

In order to separate contributions from the event vertex fit, which will be discussed in Section 4.4, here, instead of the primary event vertex, an average beam position (*run vertex*, see below) is used in the impact parameter definition (3.7) , the resulting quantity being denoted $d_{ca,RV}$ in the following. The width of the central Gaussian of the $d_{ca,RV}$ distribution is shown for inclusive tracks in Figure 4.7 as a function of track φ_0. Here, the minimum transverse momentum cut has been raised to 4 GeV in order to suppress multiple scattering effects. In this region, the φ_0 dependence of the $d_{ca,RV}$ resolution is expected to follow, to good approximation, a function of the form

$$\sigma^2_{d_{ca,RV}}(\varphi_0) = \sigma_0^2 + \sigma_x^2 \sin^2\varphi_0 + \sigma_y^2 \cos^2\varphi_0 \quad , \tag{4.4}$$

[6] Also the primary vertex resolution, which will be discussed in Section 4.4, enters here.

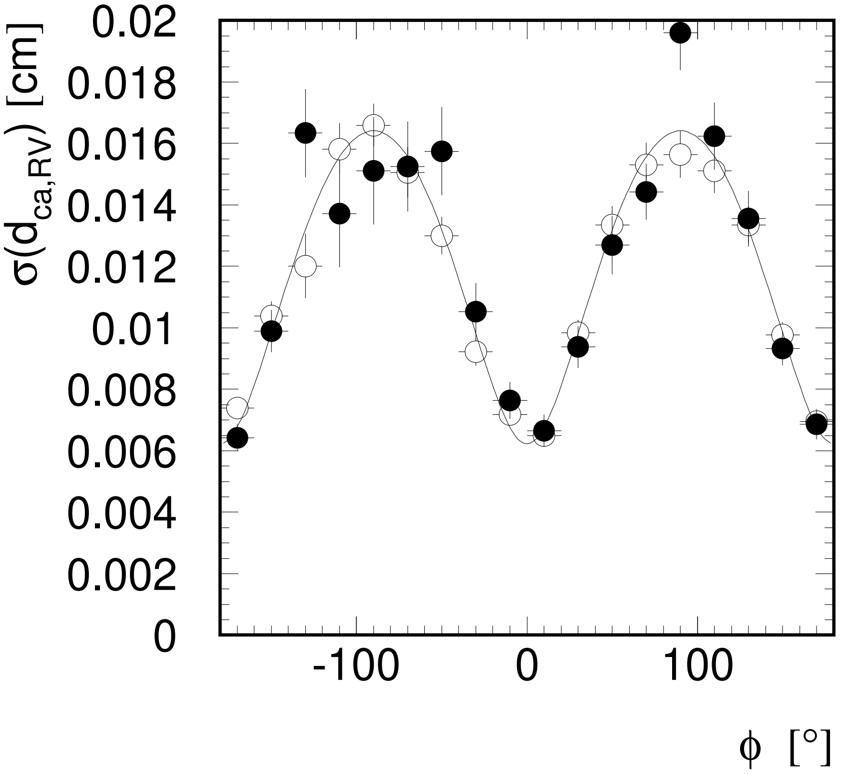

Figure 4.7: *Width of the central Gaussian of the $d_{ca,RV}$ distribution as a function of the track direction around the beam for inclusive tracks ($p_t > 4$ GeV) from H1 data (closed points) and PYTHIA MC (open points). The curve corresponds to Equation (4.4) with the parameters (4.5).*

where σ_0 accounts for the intrinsic CST d_{ca} resolution. σ_x and σ_y describe the size of transverse interaction region profile at HERA, which is an ellipse with a horizontal–to–vertical aspect ratio of $\sigma_x/\sigma_y = 5/1$. In an earlier study [42], these parameters were determined using 1997 data to be

$$\sigma_0 = 54\ \mu\text{m} \quad , \quad \sigma_x = 155\ \mu\text{m} \quad \text{and} \quad \sigma_y = 31\ \mu\text{m} \ . \tag{4.5}$$

This is also an adequate choice here. Using the measured values for σ_x and σ_y in the Monte Carlo simulation, a good description of the data in $\sigma^2_{d_{ca,RV}}(\varphi_0)$ is obtained.

4.4 Primary Vertex Reconstruction

The impact parameter method requires precise knowledge of the primary vertex position in the plane transverse to the beam axis. As shown in the previous section, the transverse profile of the interaction region at HERA (*beam spot*) has a Gaussian width of 155 μm in the horizontal (x) direction and about 31 μm in the vertical (y) direction. For each run the average coordinates of the ep interaction point are determined by collecting information from many events. This *run vertex* is used as starting point for an event–wise primary vertex fit to selected tracks. CST information is used in the determination of the run vertex as well as in the event vertex fit to ensure a high reconstruction quality.

Fit Procedure

For the determination of the primary event vertex the software package CSPRIM [60] is used. A tight selection of the input tracks is applied in order to avoid a possible bias from secondary particle tracks, e.g. all tracks are required to be compatible with the run vertex within two standard deviations. For the same reason, the muon candidate track is excluded explicitly from the vertex fit.

The fit follows a two–step procedure. First, the vertex position in the xy–plane is determined. In a second step the z–coordinate is reconstructed from selected tracks having been matched to the xy vertex position.[7] As in this analysis the muon impact parameter is calculated in the xy plane, only the first step is relevant here.

The event vertex position $\vec{x}_V$ in the xy–plane is determined by iteratively minimising

$$\tilde{\chi}^2 = \sum_i \left\{ d_i^2/\sigma_{d_i}^2 + (\vec{x}_V - \vec{x}_{RV})^T \cdot V_{RV}^{-1} \cdot (\vec{x}_V - \vec{x}_{RV}) \right\} \quad . \tag{4.6}$$

Here, $\vec{x}_{RV}$ and V_{RV} denote the run vertex xy–position and covariance matrix respectively. The sum includes all input tracks, d_i^2 and $\sigma_{d_i}^2$ being the significance of the xy separation between track i and the event vertex and its associated error respectively. After each iteration step the track with the largest $\tilde{\chi}^2$–contribution is excluded if the contribution exceeds a given limit.

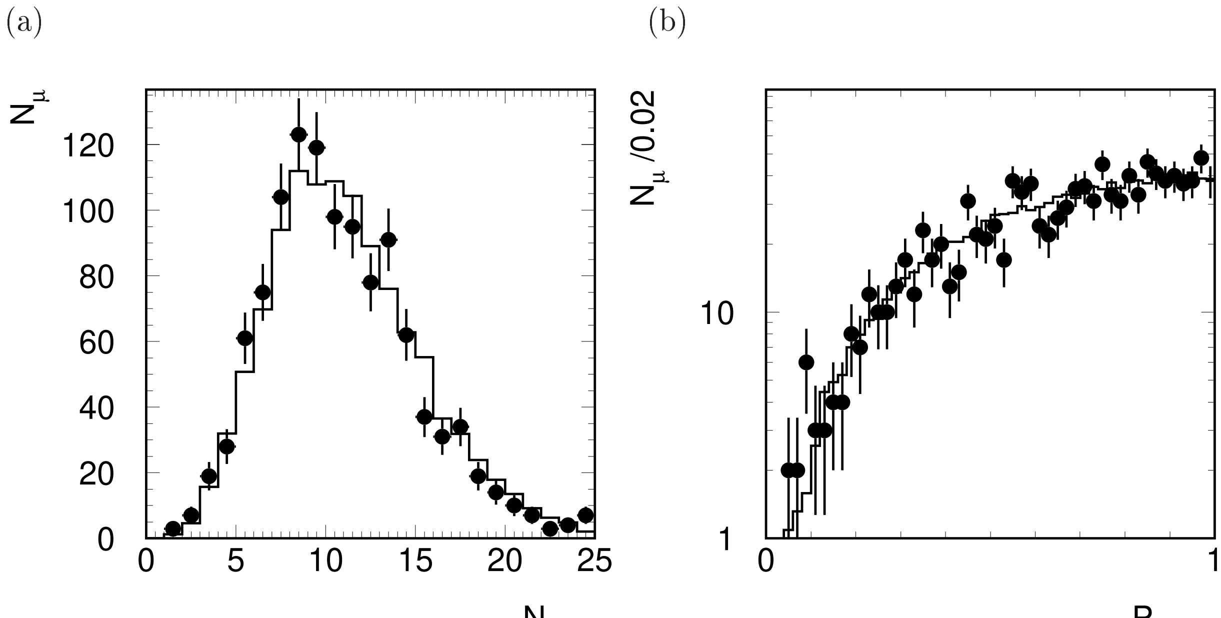

Figure 4.8: *(a) Number of tracks used in the primary vertex fit and (b) primary vertex fit probability for the H1 data (points) and the combined MC simulated samples (histograms).*

[7] The HERA beams are slightly tilted with respect to the z axis, so that the xy-position of the vertex depends on z. The xy vertex fit step, therefore, needs to be repeated with the new z position.

Selection and Performance

In analogy to Equation (4.2), the $\tilde{\chi}^2$ resulting from the vertex fit can be translated into a probability–like quantity[8] $\tilde{\mathcal{P}}_{\text{track}}(\tilde{\chi}^2, N_{tr})$, N_{tr} denoting the number of tracks used in the vertex fit, and this can be used as a measure for the vertex reconstruction quality. Also, the precision of the vertex fit is expected to improve with N_{tr}. The H1 data distributions of $\tilde{\mathcal{P}}_{\text{track}}$ and N_{tr} are well modelled by the MC simulation, see Figure 4.8. Thus both quantities can be used to define selection criteria.

It turns out, however, that the internal selection cuts applied within the default vertex fit procedure already ensure an acceptable vertex quality, so that no further strong requirements are needed. Only an additional cut $\tilde{\mathcal{P}}_{\text{track}} > 0.01$ is applied and events where only one track has been used to determine the primary vertex are rejected.

The vertex reconstruction resolution is estimated using MC events by looking at the difference between the reconstructed and simulated vertex position. This is shown for the x–projection in Figure 4.9. For inclusive tracks, this distribution has an RMS of 100 μm and a central Gaussian part with a width of about 70 μm. For beauty production events, the primary vertex reconstruction is complicated by a large secondary particle activity resulting in about a 30% decrease of the x vertex resolution. In both cases, however, this is still a clear improvement with respect to the beam spot size along the x axis of 155 μm. In the y–projection, however, the vertex fit is completely dominated by the constraint from the small beam spot size of 31 μm and, therefore, no significant improvement is achieved by replacing the run vertex with the CSPRIM event vertex.

Having reconstructed the primary event vertex, the φ–dependence of the impact parameter resolution $\sigma(\delta)$ can be studied as has been described for the track separation from the beam line, $d_{ca,RV}$, in Section 4.3. The result is shown in Figure 4.10, where, in contrast to Figure 4.7, the minimum track p_t cut has been relaxed to the standard value of 2 GeV. Neither the resulting increase of multiple scattering effects nor the contribution from the CST event vertex resolution spoil the agreement between the H1 data and the MC simulation.

In conclusion, the reconstruction of the run vertex, the CST–CJC combined track and the CST–improved primary event vertex is found to be well under control. The resulting δ resolution ranges from about 70 μm to 115 μm for vertical and horizontal tracks respectively. Comparing this to a typical δ_{true} value of 150 μm which is expected for muons from beauty decays (cf. Section 3), the reconstruction quality should be sufficient for an impact parameter analysis to separate the signal from light–flavour induced background. It should be noted, however, that this statement needs to be verified at a later stage in the analysis, because for an asymmetric distribution the reconstruction quality for $sign(\delta)$ via a jet–based reference axis needs to be considered in addition. Differences in the kinematics between inclusive tracks and muons from beauty decays might also have to be taken into account as well as the decreased primary vertex resolution for signal events due to the large secondary particle activity.

[8]Due to the iterative track rejection within the vertex fit, the resulting $\tilde{\chi}^2$ does not follow a χ^2 distribution. Strictly speaking, the corresponding $\tilde{\mathcal{P}}_{\text{track}}$, therefore, cannot be interpreted as vertex fit probability.

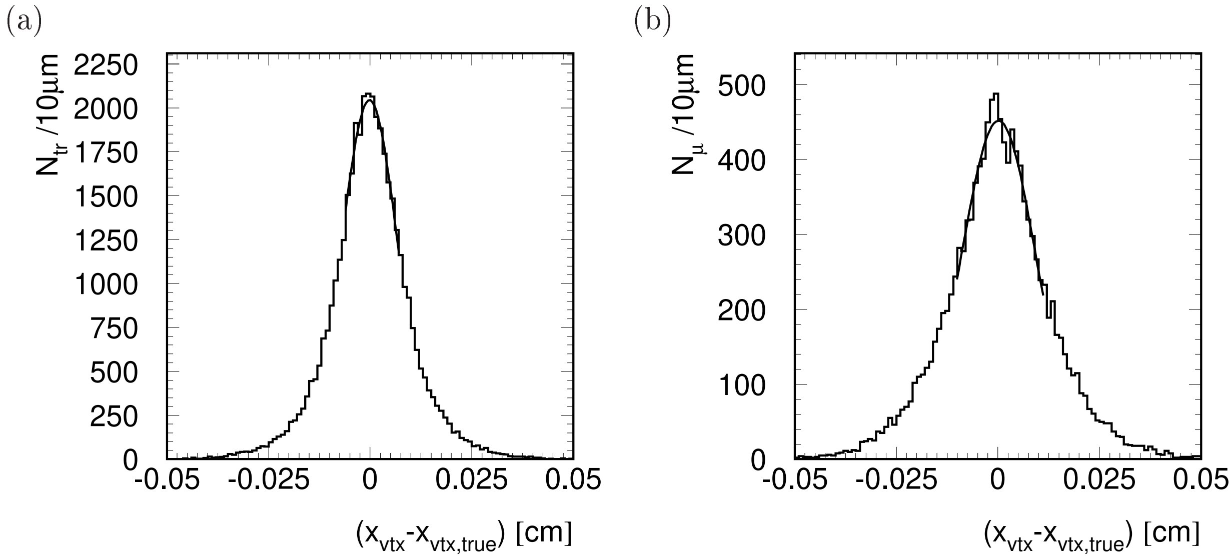

Figure 4.9: *Primary vertex resolution in x obtained from simulated event samples: (a) inclusive tracks (PYTHIA) and (b) semi–muonic beauty decays (AROMA).*

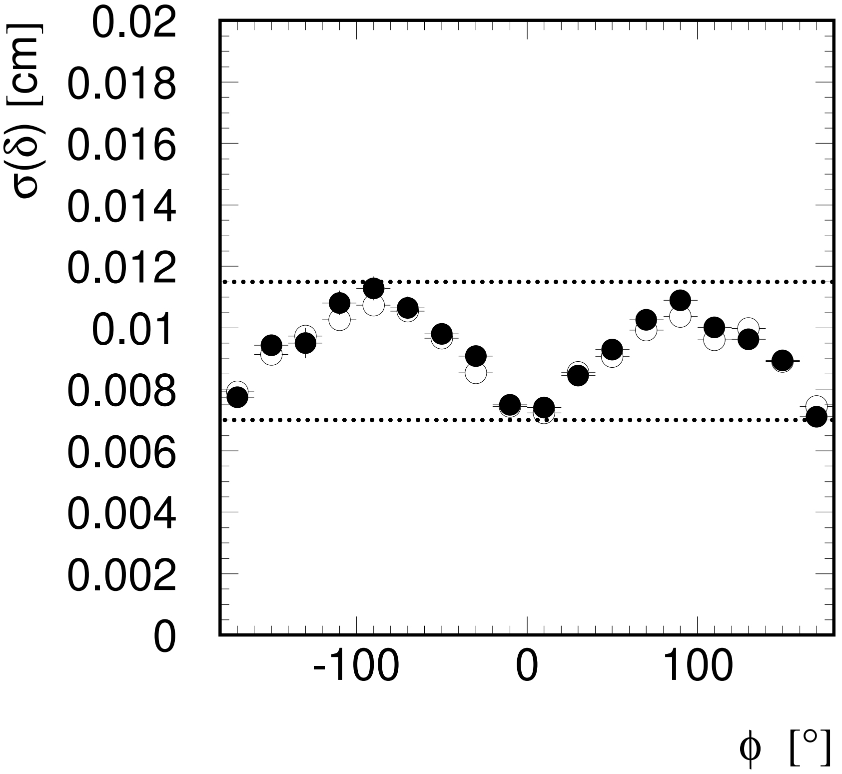

Figure 4.10: *Width of the central Gaussian of the δ distribution as a function of the track direction around the beam for inclusive tracks ($p_t > 2$ GeV) from H1 data (closed points) and PYTHIA MC (open points).*

4.5 Jet Reconstruction

The role of jets in this analysis is twofold:

1. Requiring at least two reconstructed hadronic jets selects a topology expected for photon–gluon fusion, which is the dominating mechanism for beauty production. The resulting inclusive 2–jet sample will, however, be largely dominated by light flavour production.

2. If a muon candidate is found in one of the selected jets, the relative muon–jet topology is used to define two observables, which are sensitive to beauty production. In both observables the jet enters as a reference axis approximating the original hadron direction, cf. Chapter 3.3.

The definition of final state detector objects serving as input for the jet algorithm as well as the construction and selection of jets is described in this section.

4.5.1 Reconstruction of Hadronic Final State Objects

The starting point for the reconstruction of the hadronic final state particles are *clusters* in the LArC and SpaCal resulting from the combination of energy depositions in neighbouring calorimeter cells. The clustering procedure is done independently for the electromagnetic and the hadronic sections in the SpaCal, whereas LArC clusters can in general include cells from both sections. Although there is no strict one–to–one correspondence between clusters and particles, the gross features of the final state topology are in general reasonably well described by the cluster four–momenta defined by the cluster energies and positions.

The final state energies will typically be underestimated due to imperfections in the calorimeter hermeticity and particle energy losses in inactive (*dead*) material between the interaction point and the inner calorimeter surface. Also, a necessary electronic noise suppression procedure rejecting isolated low–energy depositions in some cases removes energy originating from physical particles. Globally, these effects are accounted for in the calorimeter energy calibration procedure, which includes dead material corrections. However, the reconstruction quality can be improved further by using event–by–event the information from reconstructed charged particle tracks. For this purpose vertex–fitted drift chamber tracks with a transverse momentum $p_t^{track} > 150$ MeV are selected. A track energy is defined by assuming the corresponding particle to be a pion with the measured three–momentum. In the following, the reconstructed tracks and clusters are also referred to as final state or detector *objects*.

Simply adding track and calorimeter objects without further manipulation certainly over–estimates the final state particle energies due to double counting. The tracks and clusters, therefore, have to be combined in a more sophisticated way.

Combination of Clusters and Tracks

Selected clusters and tracks are collected into a combined list of final state objects using an existing software implementation [61] of a scheme proposed in [62]. The idea is to reject clusters which can be associated to a track in order to avoid double counting of energy. Only tracks with a transverse momentum below an adjustable threshold $p_{t,max}$ are considered in this procedure. High–energy particles are expected to be well measured in the calorimeter while the track momentum determination precision decreases towards very high transverse momenta, which correspond to small track curvatures.

The selected tracks are extrapolated into the calorimeter. For each track, the hadronic (electromagnetic) clusters[9] within a cone of radius R_c^{had} (R_c^{elm}) are identified and sorted by their distance d_{ct} to the extrapolated track. With ascending d_{ct}, the cluster energies $E_{cl,i}$ are summed until

$$\sum_{i=1}^{j+1} E_{cl,i} > E_{track} \quad . \tag{4.7}$$

The first j clusters are then removed from the list of final state objects. The cluster $j+1$ is kept and its four–momentum is re–scaled such that the total rejected calorimetric energy equals E_{track}.

Here, the values of the free parameters are adopted from earlier analyses and set to

$$p_{t,max} = 2 \text{ GeV} \quad , \quad R_c^{had} = 50 \text{ cm} \text{ and } R_c^{elm} = 25 \text{ cm} \quad . \tag{4.8}$$

Muon Candidate Treatment

The treatment of selected muon candidates in the final state needs special consideration. Within the final state reconstruction scheme discussed above, muon candidates are included via their calorimeter depositions. Due to the transverse momentum cut $p_t^\mu > 2$ GeV, the track information is not considered. For muons, which typically loose only a small fraction of their energy within the main calorimeters, this is certainly not appropriate. In particular, a well measured muon track is crucial for this analysis and the candidate has been selected accordingly, so there is no motivation for excluding the track information for the final state reconstruction. As a result, the muon candidate track is included without modification in the list of final state objects.

An adequate treatment of calorimeter clusters behind the muon track is less obvious, because a selected muon candidate is not necessarily a real muon behaving as a minimal ionising particle. In addition, several classes of hadronic fake muon background with different calorimeter signatures need to be considered, see Section 3.2 and Appendix B.

Within a sample of muon candidates selected from the H1 data, muons and fake muons cannot be distinguished on an event–by–event basis. A common procedure, therefore, needs to be found which is applicable to muon candidates from all possible sources. Going

[9] Here, "electromagnetic" and "hadronic" refers to the calorimeter section containing the dominant part of the cluster energy.

through the complete analysis chain, several methods have been tried and compared with respect to, for example, the MC description quality for relevant observables, and the overall stability of the measurement. Some details related to the modelling of the fake muon background are discussed in Appendix B.

As a result, the track–cluster combination procedure for the muon candidate is changed in the following way:

- No $p_{t,max}$ cut is applied, i. e. the muon track information is always used.
- R_c^{had} and R_c^{elm} are reduced to 25 cm and 12.5 cm respectively.
- The condition (4.7) is ignored, i. e. all clusters behind the muon candidate track are removed irrespective of their total energy.

For the other tracks and clusters in the event the procedure remains unchanged.

Transverse Momentum Balance

The quality of the hadronic final state reconstruction can be studied in NC DIS events using the ratio of the transverse momenta of the hadronic final state and the scattered positron:

$$R_{pt} = \frac{\sqrt{(\sum_h p_{x,h})^2 + (\sum_h p_{y,h})^2}}{p_{t,e}} \quad , \tag{4.9}$$

where the sum includes all final state particles h except for the scattered positron e. Distributions of this quantity for track DIS samples obtained from H1 data and MC simulated events are shown in Figure 4.11. The simulation provides a reasonably good description of the H1 data with the maximum close to $R_{pt} = 1$ in both cases.

4.5.2 Jet Definition and Selection

After the hadronic final state objects, including the muon candidate, have been defined, they can be used as input to a jet algorithm, cf. Section 1.4. The construction, selection and resulting quality of jets within this analysis are discussed below. As stated in Section 3.1, in signal events at least two jets are expected. One of them, which in the following is denoted the *muon jet*, should contain a muon.

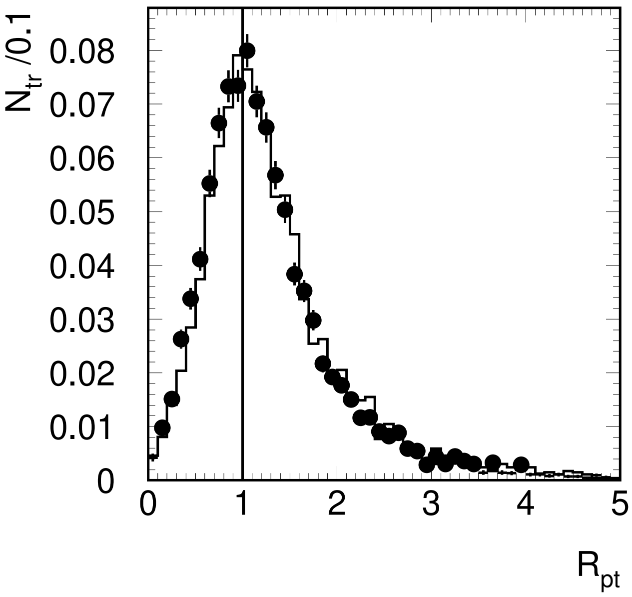

Figure 4.11: *Transverse momentum balance R_{pt} between the hadronic final state and the scattered positron for low Q^2 DIS events selected from the H1 data (points) and a DJANGO MC sample (histogram).*

Jet Algorithm

For the reconstruction of jets the *longitudinally invariant k_t algorithm* [24] is used, which is a cluster algorithm governed by two distance measures

$$d_{i,j} = \min\left(E_{t,i}^2, E_{t,j}^2\right)\frac{R_{ij}^2}{R_0^2} \qquad \text{and} \qquad d_k = E_{t,k}^2 R_0^2 \ . \tag{4.10}$$

Here, R_{ij} is the separation of two particles i and j in the pseudorapidity–φ plane,

$$R_{ij} = \sqrt{(\eta_i - \eta_j)^2 + (\varphi_i - \varphi_j)^2} \ , \tag{4.11}$$

and R_0 is an adjustable distance parameter, which usually is set to 1. For each iteration step the particle with the minimum d_k and the particle pair with the minimum $d_{i,j}$ are found. If $\min(d_k) < \min(d_{ij})$ the corresponding particle k is defined as a jet and removed from the list of input particles. Otherwise the particles i and j are combined to a new pseudo–particle (*proto–jet*) with

$$E_t = E_{t,i} + E_{t,j} \ , \qquad \eta = \frac{E_{t,i}\eta_i + E_{t,j}\eta_j}{E_{t,i} + E_{t,j}} \quad \text{and} \quad \varphi = \frac{E_{t,i}\varphi_i + E_{t,j}\varphi_j}{E_{t,i} + E_{t,j}} \ , \tag{4.12}$$

which replaces the particles i and j in the further procedure. The clustering continues until all (pseudo–)particles have been used in the jet finding.[10]

[10] For this reason, this method is also known as the *inclusive k_t* algorithm.

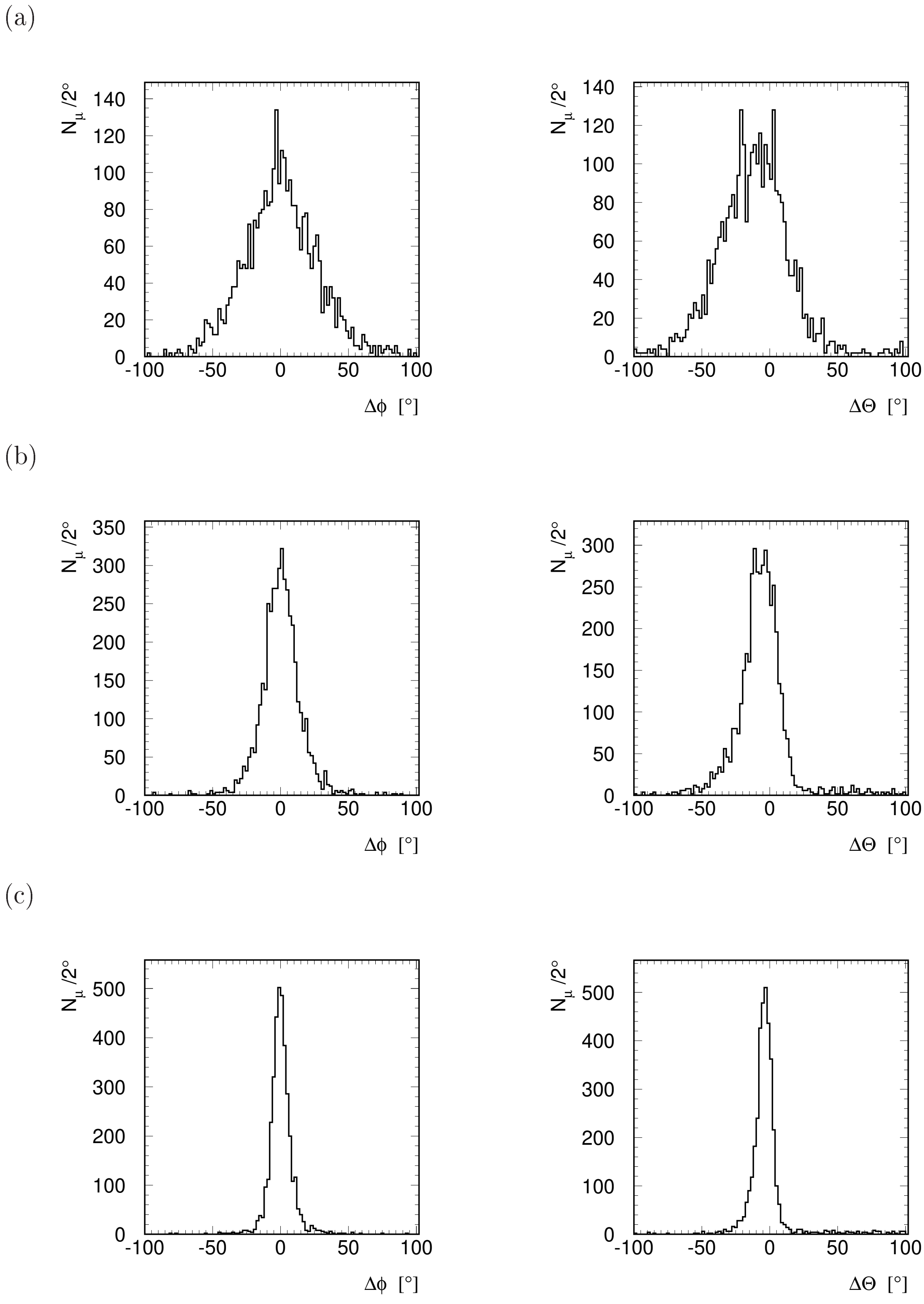

Figure 4.12: *Difference in azimuthal (left) and polar angle (right) of the muon jet and the b quark as obtained from AROMA for different muon jet E_t regions: (a)* 3 GeV $\leq E_t < 5$ GeV, *(b)* 5 GeV $\leq E_t < 8$ GeV *and (c)* 8 GeV $\leq E_t < 20$ GeV.

Selection Criteria

Having decided on the choice of final state objects and the jet algorithm, the resulting jets are uniquely defined for a given event. Now jet–based observables can be used for further event selection.

An incomplete reconstruction should be avoided by requiring the jet centre to be well inside the polar acceptance of the main detector. For the muon jet this is implied already by the restriction of the muon candidate to the central detector region. In order to ensure a sufficient "jettiness" of the event, also a cut on the jet minimum transverse momentum needs to be applied. Also, a very low E_t muon jet will be completely dominated by the muon candidate.

The jet φ and θ resolution, which arises from a combination of hadronisation effects, detector resolution and the undetected decay neutrino, depends quite strongly on the chosen cut on the minimum jet transverse momentum. Based on a sample of MC simulated signal events, this is demonstrated for three different E_t regions in Figure 4.12 showing the correlations of jet and b quark in the azimuthal and polar angle. The asymmetry in the $\Delta\theta$ distributions is due to the detector acceptance limit in the forward direction.

These findings seem to suggest a hard cut on the minimum jet transverse momentum. On the other hand, as near–threshold production is dominating (see Section 1.5.1), the signal events will be found typically in the low jet E_t region. Therefore, a minimum transverse momentum cut has to be chosen carefully in order not to loose too much acceptance. This is displayed in Figure 4.13. After going through the complete analysis

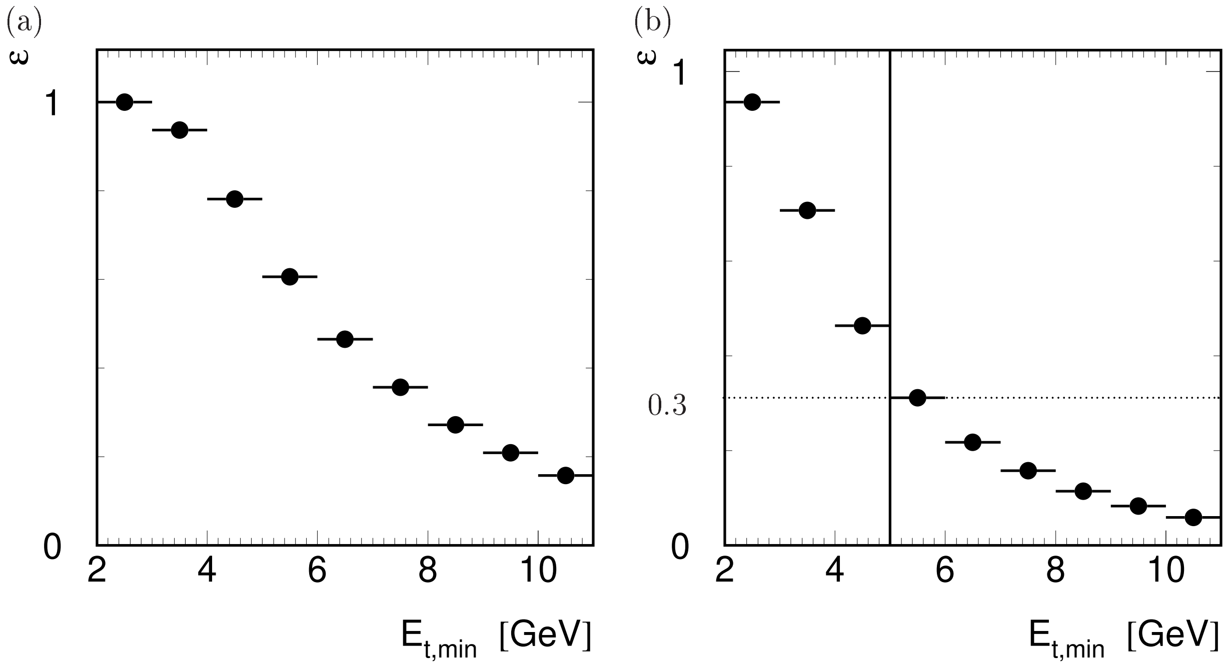

Figure 4.13: *Efficiency for a cut on the minimum transverse momentum of (a) the muon jet and (b) two jets as a function of the chosen cut value.*

chain in order to study the effect on the results, a cut of $E_t^{jet} > 5$ GeV for the muon jet and the hardest of the remaining jets in the chosen θ range is found to be a reasonable compromise. This corresponds to a signal acceptance of $\approx 30\%$, see Figure 4.13(b) and a mean resolution in φ and θ of 8°.

Jet–$D^\star$ Correlations

For this analysis, the Monte Carlo description of heavy flavour production events is of particular interest. While there is no straight–forward way to obtain a sufficiently large high purity beauty event sample from the H1 data, charm production processes can be reliably tagged via the reconstruction of $D^\star$ mesons.

In a 1997 H1 DIS event sample $D^\star$ candidates are identified via the decay chain

$$D^{*\pm} \to D^0\pi_s^\pm \to (K^\mp\pi^\pm)\pi_s^\pm \quad . \tag{4.13}$$

The selection follows [63] but uses an increased cut on the minimum $D^\star$ transverse momentum of 2.5 GeV in order to improve the signal–to–background ratio. In addition, the $D^\star$ meson has to be found within a reconstructed jet with $E_t > 5$ GeV. The resulting signal in the distribution of the reconstructed mass difference

$$\Delta M = M(K,\pi,\pi_s) - M(K,\pi) \tag{4.14}$$

is shown in Figure 4.14(a). If a second jet is required in the event, both the available statistics and the signal–to–background ratio decreases considerably, see Figure 4.14(b).

(a) (b)

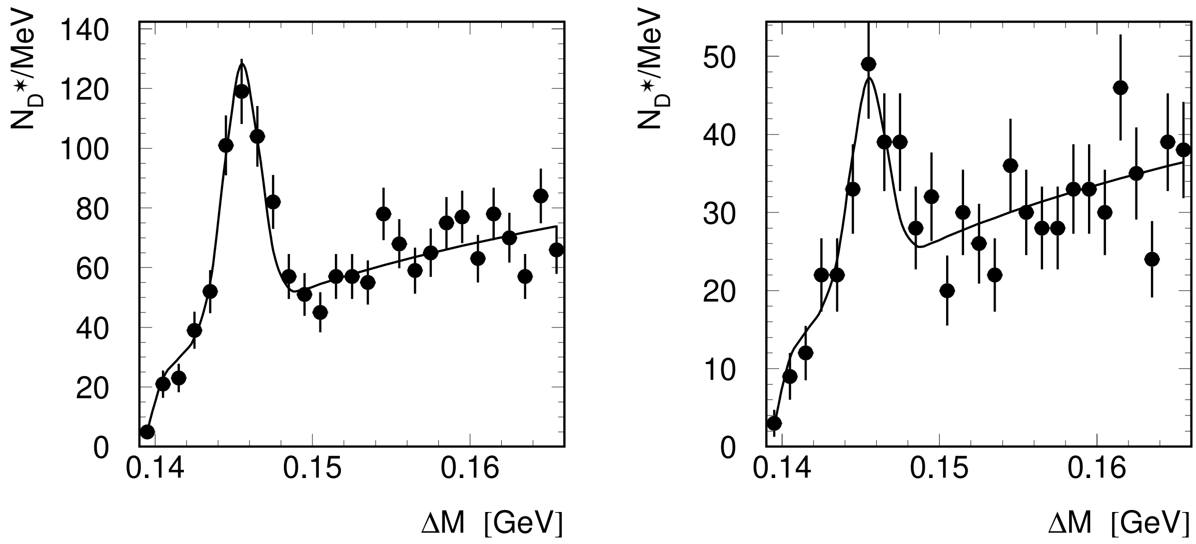

Figure 4.14: *$D^\star$ signals obtained from a 1997 H1 DIS data sample requiring (a) ≥ 1 jet and (b) at least two jets.*

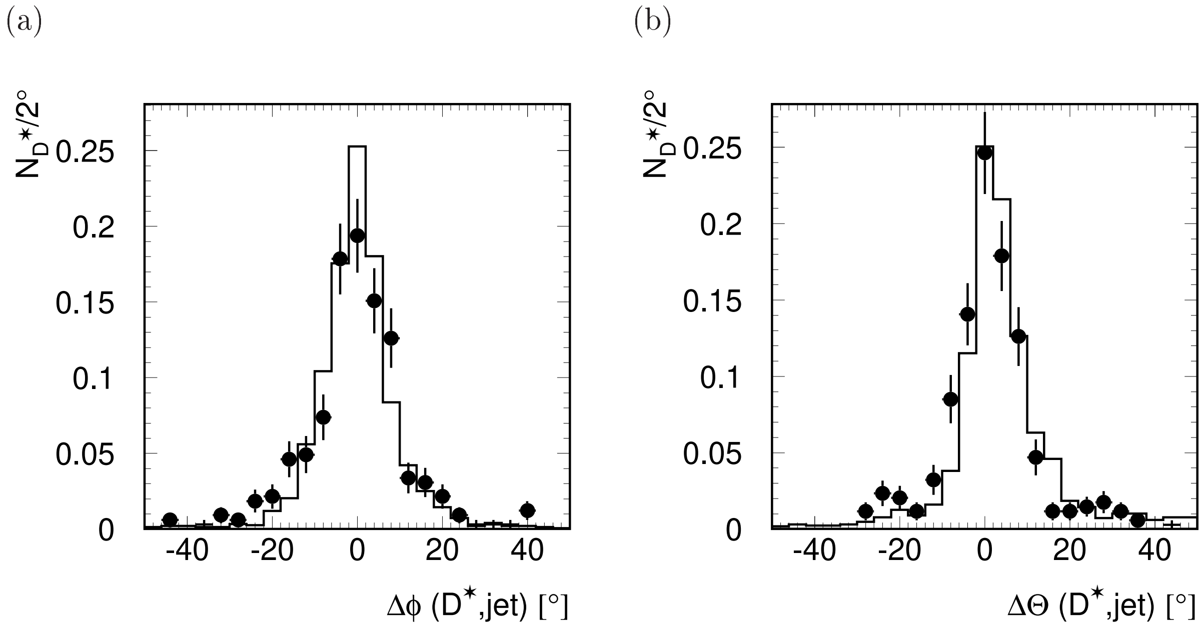

Figure 4.15: *Jet–$D^\star$ difference in (a) azimuthal and (b) polar angle for H1 data (points) and AROMA MC (histograms).*

In the following, any $D^\star$ candidate found in the region 142 MeV $< \Delta M <$ 148 MeV and $35° < \theta < 130°$ is denoted a *reconstructed $D^\star$ meson.*

Based on the one–jet selection, correlations of the $D^\star$ kinematics with corresponding jet quantities have been studied. In Figure 4.15, the distributions of the polar and azimuthal $D^\star$–jet separation are shown and compared to the AROMA MC prediction. The agreement is reasonable, but not perfect. Figure 4.15(a) suggests, that the width of the $\Delta\varphi$ distribution is somewhat underestimated by the simulation. It should be noted that the data contain non–$D^\star$ background which is not included in the simulation and the statistics are limited, so it is difficult to draw firm conclusions.

Energy Flow within Jets

The quality of the jet description can also be studied by going beyond the four–momentum representation of jets and looking into the internal jet structure. As an example, the energy flow within jets is shown in figure 4.16. For each final state object found in a jet the $\eta\varphi$ distance to the jet momentum direction is histogrammed, weighted with its relative contribution to the jet energy. The plots are based on a dijet selection ($E_t > 5$ GeV) from the $D^\star$ meson sample and light flavour dominated inclusive tracks respectively. In both cases the highest–E_t jet not containing the candidate is used. While the distribution for the charm–enriched H1 data is, within the errors, well described by the corresponding MC, light flavour jets in the H1 data appear to be slightly less collimated than predicted by the simulation.

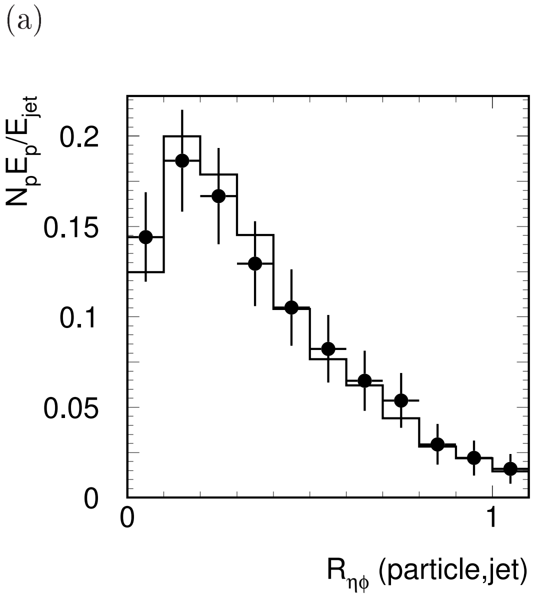

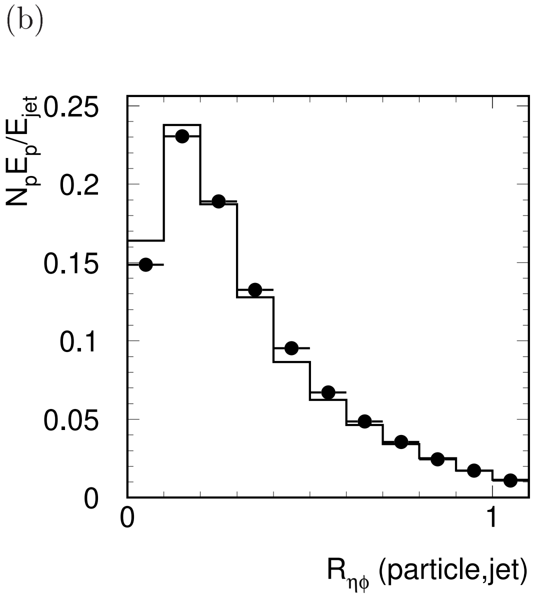

Figure 4.16: *Energy flow within the highest–E_t jet not containing the candidate as obtained from H1 data (points) and MC simulation (histograms) for (a) selected $D^\star$ mesons and (b) inclusive tracks.*

Jet Angular Resolution in Data and MC

Comparing H1 data with the MC prediction, several indications of problems in modelling the jet axis resolution have been seen:

- For selected $D^\star$ mesons found within hadronic jets, Figure 4.15(a) suggests, that the width of the azimuthal $D^\star$–jet separation distribution obtained from the H1 data is underestimated by the AROMA simulation.
- Light flavour jets in the H1 data appear to be slightly less collimated than predicted by the simulation, see Figure 4.16(b).
- The simulated p_t^{rel} spectrum for inclusive tracks is slightly shifted towards lower values compared to the corresponding H1 data distribution, cf. Figure B.7 on Page 122.

The high–statistics light–quark samples can be used to get a quantitative estimate of the effect. For this purpose, in the MC the true four vectors of the stable final state particles are taken as input to the jet algorithm. Taking the resulting *generator level* jets as reference, the resolution of the reconstructed (*detector level*) jet axis can be manipulated by scaling the $\eta\varphi$–separation of generator and detector level jets with a constant factor. While the energy flow within the jet cannot be studied in this approach, the p_t^{rel} spectrum from the H1 track data can be used to optimise the scale factor. Enlarging the $\eta\varphi$–separation by about 15% is found to give the best p_t^{rel} description. The effect of this procedure can be judged from Figure 4.17. It is, however, not clear that this result is also valid for the simulation of heavy flavour jets. A qualitative trend in same direction is visible, but the $D^\star$ sample is neither large nor clean enough for a quantitative study.

Non–negligible effects, however, cannot be excluded for a $p_t^{\rm rel}$–based measurement of beauty production. They have to be considered in the evaluation of systematic errors.

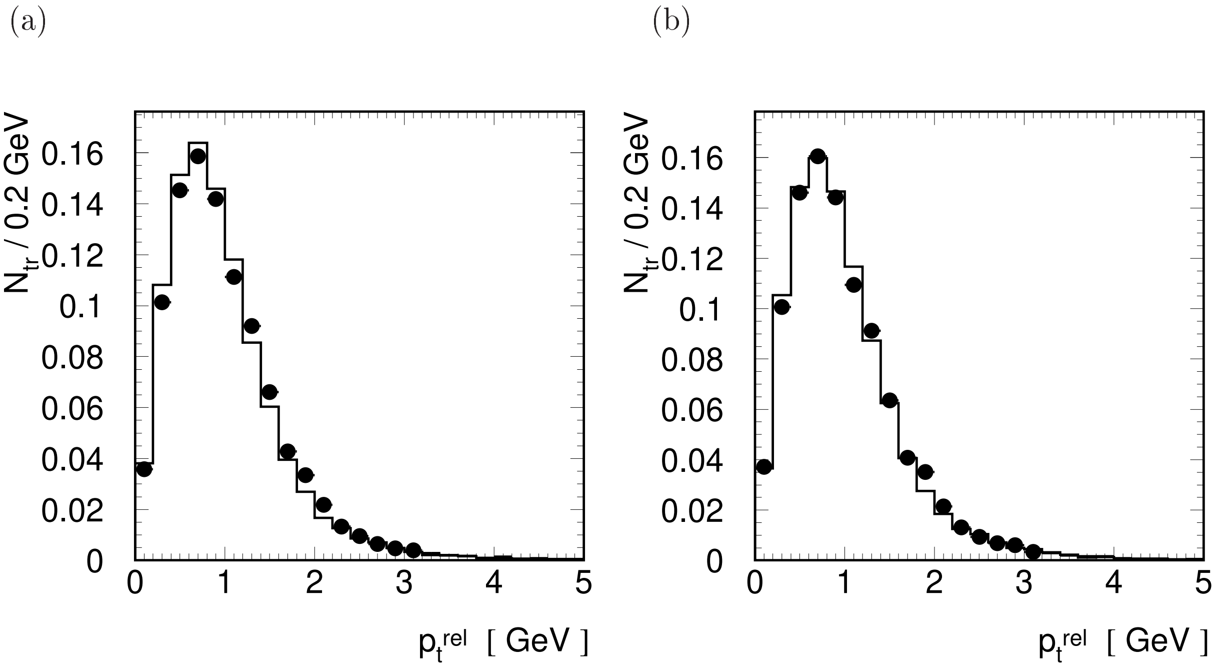

Figure 4.17: *Reconstructed $p_t^{\rm rel}$ distributions for inclusive tracks selected from the H1 data (points) and a PYTHIA simulation (histograms) (a) before and (b) after a jet direction smearing in the simulation. The distributions in (a) are the same as in Figure B.7.*

Jet Selection Summary

In summary, only events containing at least two jets with

$$E_t > 5\,\text{GeV} \quad \text{and} \quad 10^\circ < \theta < 170^\circ \tag{4.15}$$

are considered in the subsequent analysis. In at least one of these jets a muon candidate fulfilling the selection criteria described in Section 4.2 and Section 4.3 has to be found.

Applying in addition cuts on the event kinematics (see Section 4.6) and combining beauty, charm and fake muon MC event samples according to the result of the later photoproduction analysis (cf. Chapter 5), a reasonably good description of the H1 data in terms of jet based quantities is achieved. Two examples are given in Figure 4.18. The measured and simulated muon jet E_t spectra agree very well. Also for the distribution of the muon jet polar angle the simulation provides an acceptable description, with a tendency, however, to underestimate the H1 data in the forward region. Again, see also Figure 4.2, this might point to resolved processes in the H1 data, which are not included in the heavy flavour MC used here.

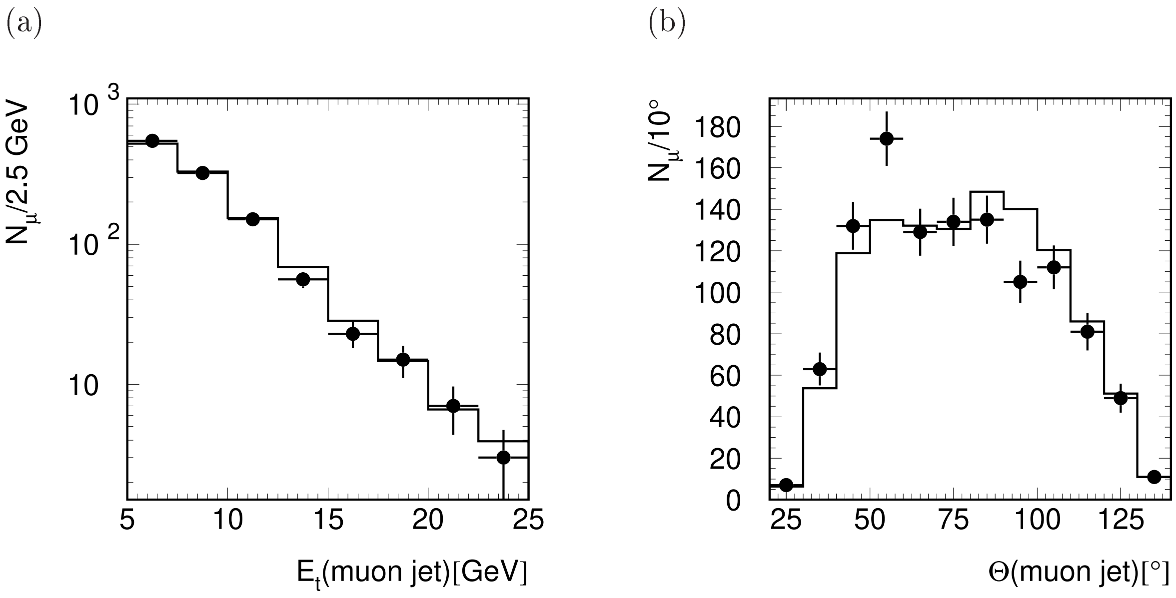

Figure 4.18: *Muon jet (a) E_t and (b) and θ for H1 data (points) and combined MC samples (histograms).*

4.6 Event Kinematics

In order to compare the experimental results to theoretical predictions, the used samples need to be well–defined in terms of the event kinematics. The aim of this analysis is to measure beauty production in two different kinematic regions, photoproduction and low Q^2 DIS. The procedure and performance of the kinematic selection for both cases is sketched in this section.

For a full description of the event kinematics it is sufficient to determine two of the three kinematic variables, cf. Equation (1.8). Here, y and Q^2 are chosen.

4.6.1 Selection of Photoproduction Events

In photoproduction processes the beam positron is typically scattered into the backward beam pipe and is not detected within the main detector. Instead, the dedicated small–angle electron tagging devices (see Section 2.4) can be used to reconstruct the scattered positron. The selection of such *tagged photoproduction* events suffers from the low kinematical acceptance of the electron taggers. In an alternative approach, *untagged photoproduction* processes can be selected indirectly by vetoing events with a scattered positron candidate found in the main detector. The default γp sample for this analysis is obtained from an untagged selection. An additional selection of tagged γp events provides a useful control sample.

Untagged Selection

Photoproduction events selected using the untagged approach contain no experimental information on the scattered positron. The reconstruction of the event kinematics, therefore, is based on hadronic final state observables. Following the *Jaquet–Blondel* (or *hadron*) method, the kinematic variables are determined according to

$$y = \frac{\sum_h (E_h - p_{z,h})}{2E_e} \quad , \quad Q^2 = \frac{\sqrt{(\sum_h p_{x,h})^2 + (\sum_h p_{y,h})^2}}{1-y} \quad , \quad x = \frac{Q^2}{sy} \quad . \tag{4.16}$$

The sum includes all final state particles h. If applied to DIS events, the scattered positron has to be explicitly excluded.

Unfortunately, the achieved resolution in Q^2 turns out to be insufficient to reliably select γp events sample by simply applying an upper cut on the reconstructed Q^2. Instead, a photoproduction sample is obtained indirectly by rejecting DIS candidate events. Due to the $1/Q^4$ dependence of the cross section, the dominant contribution to DIS background is expected from the low Q^2 DIS regime, where the positron is scattered into the backward calorimeter SpaCal (see Section 4.6.2). Events containing an electromagnetic SpaCal cluster with an energy above 8 GeV are interpreted as DIS processes and are rejected. In addition, the total energy in the SpaCal cells directly adjacent to the beam pipe (*veto layer*) is required to be less than 1 GeV. Larger veto layer energies might indicate a partially reconstructed DIS positron at the limit of the SpaCal acceptance.

DIS background, also from high Q^2 processes, can be further reduced using the reconstructed y. If a DIS positron is accidentally considered as a hadronic final state object, the sum $\sum_h (E_h - p_{z,h})$ becomes

$$\mathcal{S} = (E_e - p_{z,e}) + \sum_i (E_i - p_{z,i}) \tag{4.17}$$

resulting in a reconstructed $y = \mathcal{S}/2E_e$. For a perfect final state measurement, conservation of energy and longitudinal momentum implies $\mathcal{S} = 2E_e = 55$ GeV. In reality, the measured $\mathcal{S}$ spectrum for DIS events will be smeared around this nominal value due to detector resolution and acceptance effects. Still, for DIS background events entering the untagged γp sample a reconstructed $y \approx 1$ is expected, whereas it is unlikely to find photoproduction events in this region. DIS background, therefore, is effectively suppressed by applying an upper y cut. Events in the range

$$0.1 < y < 0.8 \tag{4.18}$$

are selected. The lower limit is motivated by difficulties in the reconstruction of very low y events, where the hadronic final state is typically concentrated in the forward region with a considerable fraction of particles outside the main detector acceptance.

In Figure 4.19 the quality of the kinematic reconstruction in the selected range is shown based on events fulfilling the subtrigger condition s19 (see Section 4.1) and all other selection criteria described in this chapter.

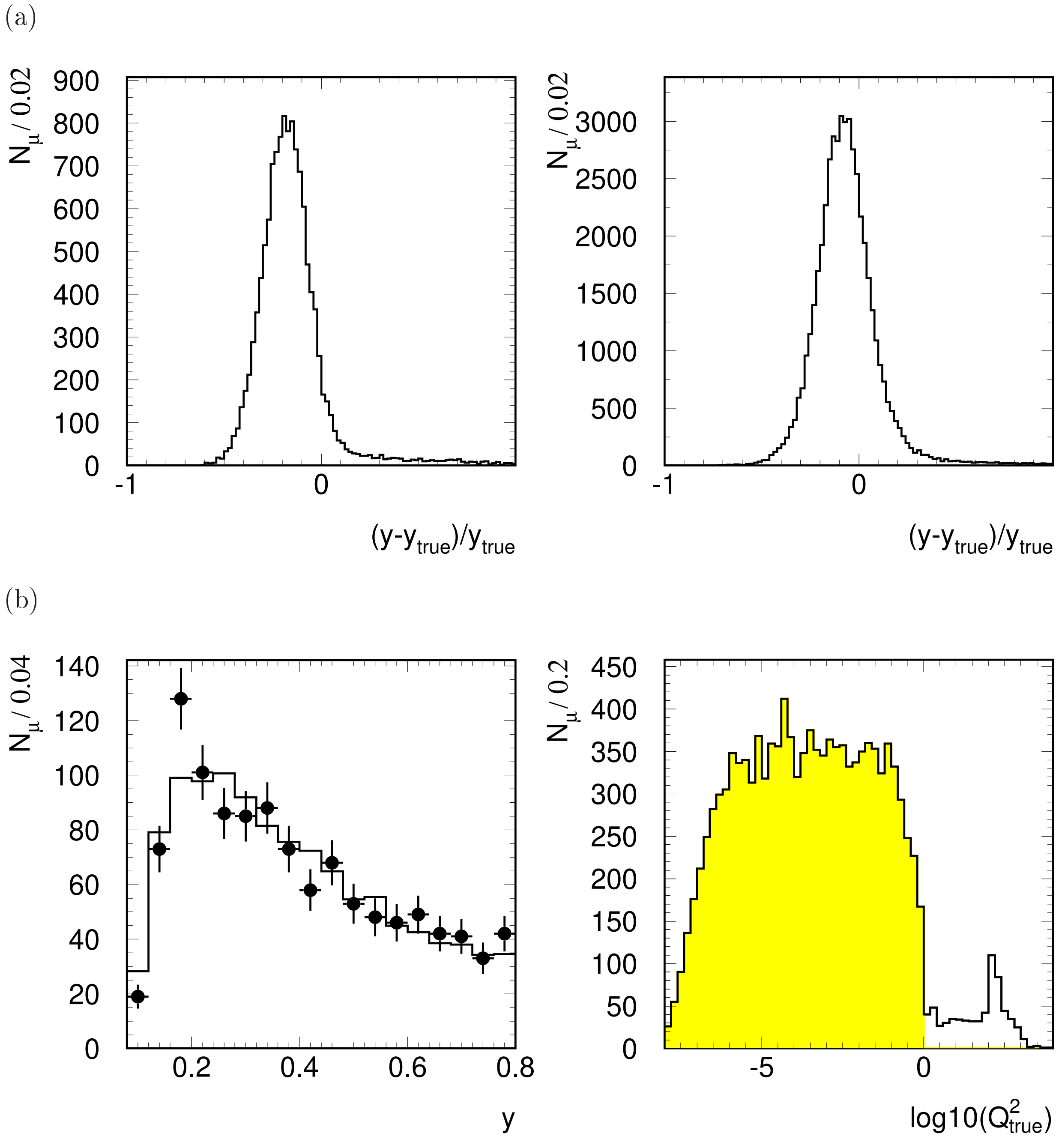

Figure 4.19: *(a) Relative deviation of the reconstructed y from the true value for simulated semi–muonic beauty decays (left) and an inclusive track MC sample (right), (b) reconstructed y distribution for H1 data (points) and combined MC samples (histogram) and (c) true Q^2 of simulated signal events after photoproduction selection, the shaded region corresponding to* $Q^2 < 1$ GeV.

The variable y is reconstructed according to Equation (4.16) using final state objects as defined in section 4.5. In Figure 4.19(a) the relative deviation of the reconstructed y from the true value is shown for simulated semi–muonic beauty decays and an inclusive track MC sample. On average, the reconstructed y in signal events is found to be 15% too low. According to generator level studies, a certain underestimation of the true y is expected due to the muon neutrino from the beauty decay escaping detection. For the light quark dominated track sample, where the effect from high–p_t neutrinos is negligible, better agreement is found. A shift to lower values by typically 6% remains, however, which is partly due to the y distribution being asymmetric within the selected range but also indicates possible imperfections in the final state reconstruction. Combining signal and background MC samples according to the result of the later photoproduction measurement, nevertheless, provides an acceptable description of the y spectrum obtained from H1 data, cf. Figure 4.19(b).

As demonstrated for simulated signal events in Figure 4.19(c), the above selection results in a fairly clean photoproduction sample with

$$Q^2 < 1 \text{ GeV}^2 \quad . \tag{4.19}$$

The relative DIS contamination is found to be at the level of 6% and accounted for.

Tagged Selection

The tagged photoproduction selection, which has been adopted from [64], uses events fulfilling one of the L1 subtrigger conditions s83 and s84 (see section 4.1). A minimum energy deposition E_{ET} of 4 GeV is required within the corresponding electron tagging device, i. e. ET33 and ET44 for s83 and s84 respectively. For the ET33, additional cuts are applied to ensure a good energy containment. The cluster position has to be within a horizontal distance of 6.5 cm from the geometrical centre of the detector. The limited acceptance in the vertical direction is accounted for indirectly by a restriction to the kinematic region $0.28 < y < 0.68$, where y is calculated from E_{ET} and the positron beam energy E_e according to

$$y = 1 - E_{ET}/E_e \quad , \tag{4.20}$$

cf. Section 1.3.2. As demonstrated in Figure 4.20, which shows the y distribution reconstructed using the hadron method (4.16), the resulting sample is highly dominated by medium y values obtained from the ET33 selection. The contribution from ET44 corresponds to the small peak in the low y region.

4.6.2 Selection of Low Q^2 DIS Events

The selection of DIS events is based on the reconstruction of the scattered positron in the backward calorimeter SpaCal. According to Equation 1.10, the SpaCal polar angular acceptance of $153° \lesssim \theta \lesssim 178°$ translates into accessible Q^2 values between about 1 GeV^2 and 100 GeV^2. This region of the phase space is commonly referred to as the *low Q^2 DIS* domain. The selected events fulfil the subtrigger condition s2/s61 based on a combined SpaCal–CJC signature (see Section 4.1).

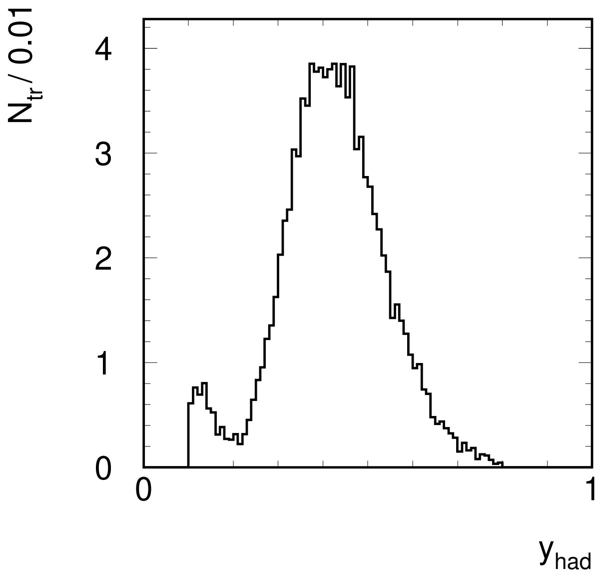

Figure 4.20: *y distribution (hadron method) for the tagged γp sample.*

Reconstruction of the Scattered Positron

The offline reconstruction and selection of scattered positron candidates follows a standard procedure using existing software [65], which provides a technical interface to the relevant detector information.

The selection is based on SpaCal clusters resulting from the grouping of energy depositions in neighbouring cells. The cluster energy E_{cl} is obtained by summing the energies from the contributing cells. The position in the xy plane and the transverse dispersion of the cluster are calculated from the cell information using *logarithmic weighting*. Details can be found in [66].

The maximum energy cluster in the electromagnetic SpaCal section is taken as scattered positron candidate if

$$E_{cl} > 9 \text{ GeV} \quad . \tag{4.21}$$

The positron four–momentum is determined from the cluster energy, the cluster xy–position and the z–position of the (CJC) event vertex. Further quality cuts are applied, e.g. on the cluster size and position,[11] which have been adopted from an earlier analysis. The details are described in [63].

[11] Here, *beam tilt corrections* are applied accounting for z dependent deviations of the beam transverse position from $(x, y) = (0, 0)$.

Event Containment

As has been discussed in Section 4.6.1, for well reconstructed DIS events the sum $\mathcal{S}$ of the differences of the energies and the z–momenta of all reconstructed final state particles (including the scattered positron) is expected to be compatible, within the detector resolution, with $2E_e = 55$ GeV. Allowing for resolution and acceptance, the selected $\mathcal{S}$ interval is

$$35 \text{ GeV} < \mathcal{S} < 70 \text{ GeV} \quad . \tag{4.22}$$

Larger deviations from the nominal $\mathcal{S}$ value are expected for poorly reconstructed DIS processes as well as for photoproduction events, where the positron escapes undetected into the backward beam pipe resulting in small $\mathcal{S}$ values. The same holds for *initial state radiation* (ISR) processes, where the incoming beam positron radiates a high–energy photon under typically small emission angles.

Kinematic Cuts

The kinematic variables Q^2 and y are calculated according to Equation (1.10) using the scattered e^+ quantities (*electron method*). The selected Q^2 range

$$2 \text{ GeV}^2 < Q^2 < 100 \text{ GeV}^2 \tag{4.23}$$

is given by the acceptance of the SpaCal e^+ selection. y is restricted to

$$0.05 < y < 0.7 \quad . \tag{4.24}$$

The upper y cut roughly corresponds to the chosen minimum positron energy of 9 GeV. At very low y the electron method y resolution degrades significantly.

Performance

The quality of the kinematic reconstruction in the selected region can be judged from Figure 4.21.

Based on simulated signal events, for both y and Q^2 the distributions of the relative deviation of the reconstructed value from the true value is found to be well–centred at 0 with a width of about 4%, see Figure 4.21(a) and (b). The non–Gaussian tails in the $(y - y_{true})/y_{true}$ distribution reflect the degrading reconstruction quality towards low y.

Within the large errors of the signal data sample, the combined MC prediction provides an overall acceptable description of the kinematic variable spectra, cf. Figure 4.21(c) and (d). There are, however, indications for problems at large y, where the prediction is found to be below the data. This might indicate that γp background, due to hadrons and photons mis–identified as positrons, is underestimated in the MC.

(a)

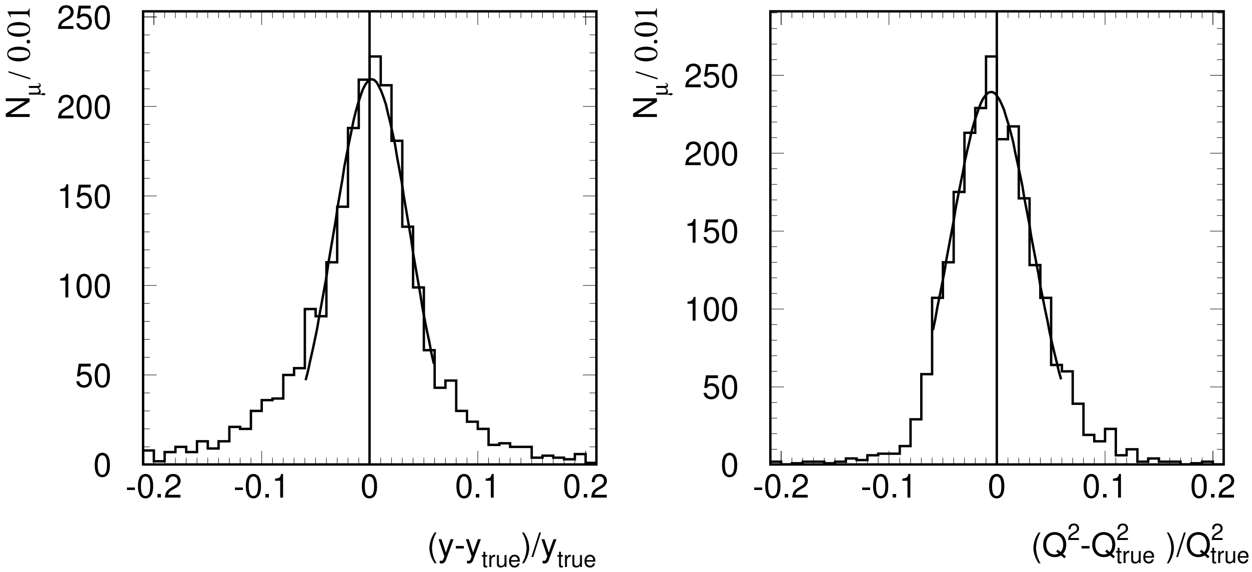

(b)

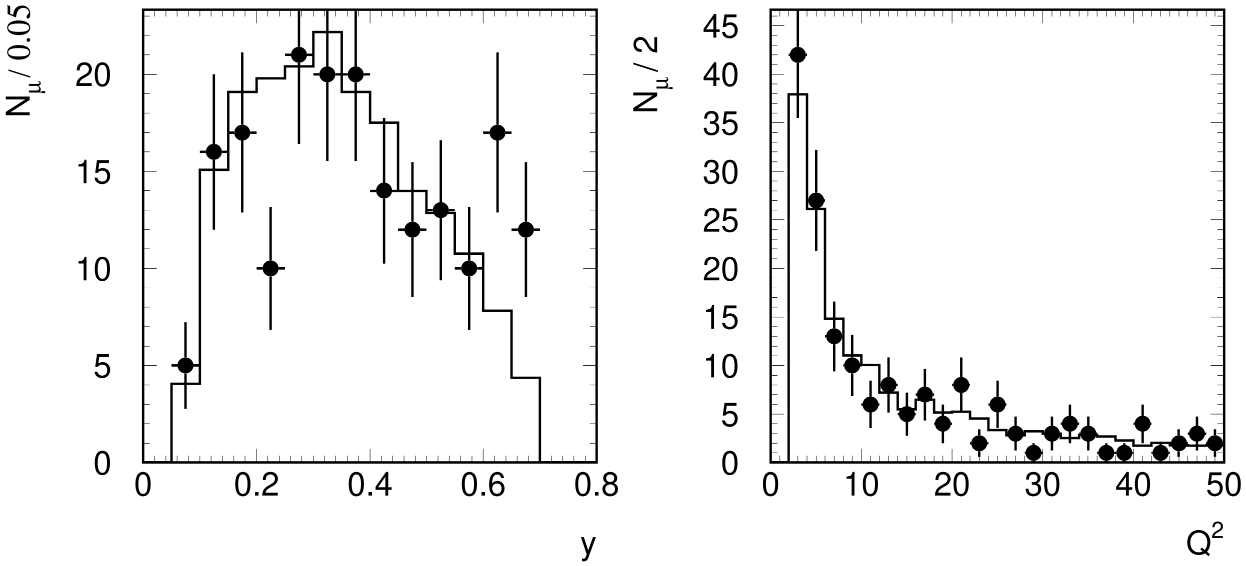

Figure 4.21: *(a) Relative deviation of the reconstructed y (left) and Q^2 (right) from the true value for simulated semi–muonic beauty decays. (b) Reconstructed y (left) and Q^2 (right) distributions for H1 data (points) and combined MC samples (histograms).*

4.7 Selection and Trigger Efficiencies

In the following, an overview of the efficiencies for the event selection criteria and trigger conditions is given, which are determined from the AROMA simulation of semi–muonic beauty decays. Relevant differences between the H1 data and the MC simulation and the corresponding corrections are also summarised.

4.7.1 Selection Efficiency

Table 4.2 summarises the selection efficiency as obtained from the AROMA MC in the region $Q^2 < 1$ GeV^2 (2 GeV$^2 < Q^2 < 100$ GeV^2), $0.1 < y < 0.8$ ($0.05 < y < 0.7$), $p_t^\mu > 2$ GeV and $35° < \theta^\mu < 130°$, which defines the visible range for the later cross section measurement in photoproduction (DIS).

	Efficiency [%]					
	γp			DIS		
sim. muons within visible range	100.0	——	——	100.0	——	——
rec. muons within visible range	67.8	100.0	——	63.1	100.0	——
CST–improved muon reconstruction	47.6	70.2	100.0	43.3	68.7	100.0
Jet selection	14.1	20.8	29.7	11.4	18.1	26.3

Table 4.2: *Selection efficiency for semi–muonic beauty decays as determined from AROMA. The visible ranges for photoproduction (γp) and deep inelastic scattering (DIS) are defined by the event and muon kinematics as described in the text. The muon reconstruction efficiency reflects inefficiencies in the identification of muons in the drift chamber and the instrumented iron (without CST–related selection cuts) as well as migrations in Q^2 and y.*

Comparing for the visible ranges the number of simulated muons to the number of reconstructed muons yields an efficiency of 68% and 63% for photoproduction and DIS respectively, which reflects inefficiencies in the reconstruction of muons in the drift chamber and the instrumented iron as well as migrations in Q^2 and y. For the CST–related track and vertex selection criteria an efficiency of about 70% is found. The largest effect, however, arises from the the jet selection (including the requirement that the muon is found in one of the selected jets). The corresponding efficiency in photoproduction and DIS is determined to be 30% and 26% respectively.

In order to account for imperfections in the description of the H1 data by the MC simulation, the selection efficiency is corrected in the following way:

- A correction of 9% is applied accounting for the overestimation of the track selection efficiency close to the inefficient CJC regions by the simulation, see section 4.2.
- Due to the differences between H1 data and simulation in the CST–drift chamber combination, see Section 4.3, the MC efficiency is corrected by 8%.

This results in a corrected signal selection efficiency in the visible range of 12% for photoproduction and 10% for DIS. These numbers include all selection criteria except for the trigger conditions. The trigger efficiencies are discussed in the next section.

4.7.2 Trigger Efficiency

The trigger efficiencies given below are determined, based on independent subtrigger conditions, for muon candidates fulfilling all other selection cuts.

Photoproduction

The efficiency of the L1 subtrigger condition s19 for muon candidates is determined using an independent, calorimeter–based subtrigger. The results for signal data and signal MC are listed in Table 4.3. The simulation tends to slightly overestimate the trigger efficiency. Within the statistical errors, however, the effect is not significant. In conclusion, the L1 trigger efficiency is taken from data to be 81.8%. The statistical uncertainty of 3.2% will be taken into account in the systematic error.

L1 trigger condition	Efficiency [%] H1 data	MC
`DCRPh_THig`	98.6 ± 1.0	99.8 ± 0.1
`zVtx_sig`	95.3 ± 1.7	97.8 ± 0.4
`Mu_Bar`	85.1 ± 2.9	85.6 ± 0.9
s19	81.8 ± 3.2	82.4 ± 0.9

Table 4.3: *Efficiency of the L1 subtrigger condition s19 for signal events selected from H1 data and AROMA MC respectively.*

In 1997, a trigger verification was performed on trigger level 4. For muon–system based subtriggers, this includes a requirement for a reconstructed track in the iron to be close in both θ and φ to a reconstructed drift chamber track. This matching procedure causes an inefficiency, especially for subtrigger conditions containing the `MU_BAR` trigger element. Using an iron–independent L4–verified subtrigger, the s19 L4 verification efficiency for signal H1 data events is determined to be $(75.0 \pm 2.9)\%$. This inefficiency only becomes effective, however, for events fulfilling no other L4–verified subtrigger condition. The effective L4–efficiency is found to be $(93.6 \pm 3.8)\%$. As the L4 verification is not included in the simulation, the MC needs to be corrected accordingly. Again, the statistical uncertainty of this correction will enter the systematic error.

DIS

The maximum energy threshold of the inclusive electron trigger of 6 GeV is well below the applied cut of 9 GeV on the minimum energy of the scattered positron. Additional cuts on the positron's polar angle and the reconstructed Q^2 ensure the positron to be well inside the geometrical acceptance of the SpaCal. Inefficiencies of the `SPCLe_IET` L1 condition are, therefore, expected to be negligible and are not considered here. The efficiencies of the other L1 trigger elements contributing to the subtrigger condition s2/s61 are determined using two independent subtriggers, which are based on the LArC and the SpaCal respectively. The results are shown in Table 4.4. In data, the trigger efficiency is determined to be 92.4 ± 3.0. A moderate overestimation of 5% is seen in the simulation, which is slightly larger than the statistical uncertainty, and the MC is corrected accordingly. This will also be considered in the estimation of the systematic error.

L1 trigger condition	Efficiency [%] H1 data	MC
`DCRPh_THig`	$100^{+0}_{-2.9}$	$100^{+0}_{-1.0}$
`zVtx_sig`	92.4 ± 3.0	97.4 ± 1.0
s2/s61	92.4 ± 3.0	97.4 ± 1.0

Table 4.4: *Efficiency of the L1 subtrigger condition s2/s61 for signal events selected from H1 data and AROMA MC respectively.*

4.8 Resulting Event Samples

The selection procedure which has been described in this chapter results in the following samples:

- **H1 data:** The photoproduction and DIS samples selected from the H1 data correspond to an integrated luminosity of 11.6 pb^{-1} and 10.5 pb^{-1} respectively.[12] The γp sample consists of 1133 muon candidates, which are found in 1126 different events. The DIS selection results in 183 events with 187 muon candidates. A candidate event for beauty photoproduction has already been discussed in Chapter 3 (see Figures 3.1 and 3.2). An example for a candidate event entering the final DIS sample is shown in Figure 4.22.

- **Signal MC:** Semi–muonic beauty decays corresponding to an integrated luminosity of about 1200 pb^{-1} are simulated using the AROMA program yielding 12536 muons in 12350 different events after all photoproduction selection cuts. 2362 muons in 2332 events fulfil the DIS selection criteria.

[12]The luminosity calculation accounts for the prescale factors associated with the L1 subtrigger conditions used in the analysis. A small fraction of events produced outside the nominal interaction region by the collisions of positrons with protons which have migrated into *satellite bunches* is also corrected for.

- **Background MC:** The background from semi–muonic charm decays is also modelled using the AROMA MC The resulting photoproduction and DIS samples after all cuts amount to about 14000 and 3000 muons respectively. To model the fake muon background, the γp (DIS) muon selection is performed on inclusive, light flavour–dominated MC samples obtained from the PYTHIA (DJANGO) program (after rejecting muons from charm and beauty decays in order to avoid a double counting of these processes in the combined MC prediction). This yields about 2000 and 450 selected fake muons in photoproduction and DIS respectively.

Additional event samples are used in systematic studies. Beauty production events are simulated using the RAPGAP program, which includes resolved photon processes, and the CASCADE program, where an alternative parton evolution model is implemented, see Chapter 1. As stated already in Section 4.1, inclusive track samples, which are obtained from light flavour–dominated MC and H1 data using muon system–independent subtriggers and omitting the muon identification criteria in the selection procedure, are used in technical studies as well as in alternative approaches to model the fake muon background.

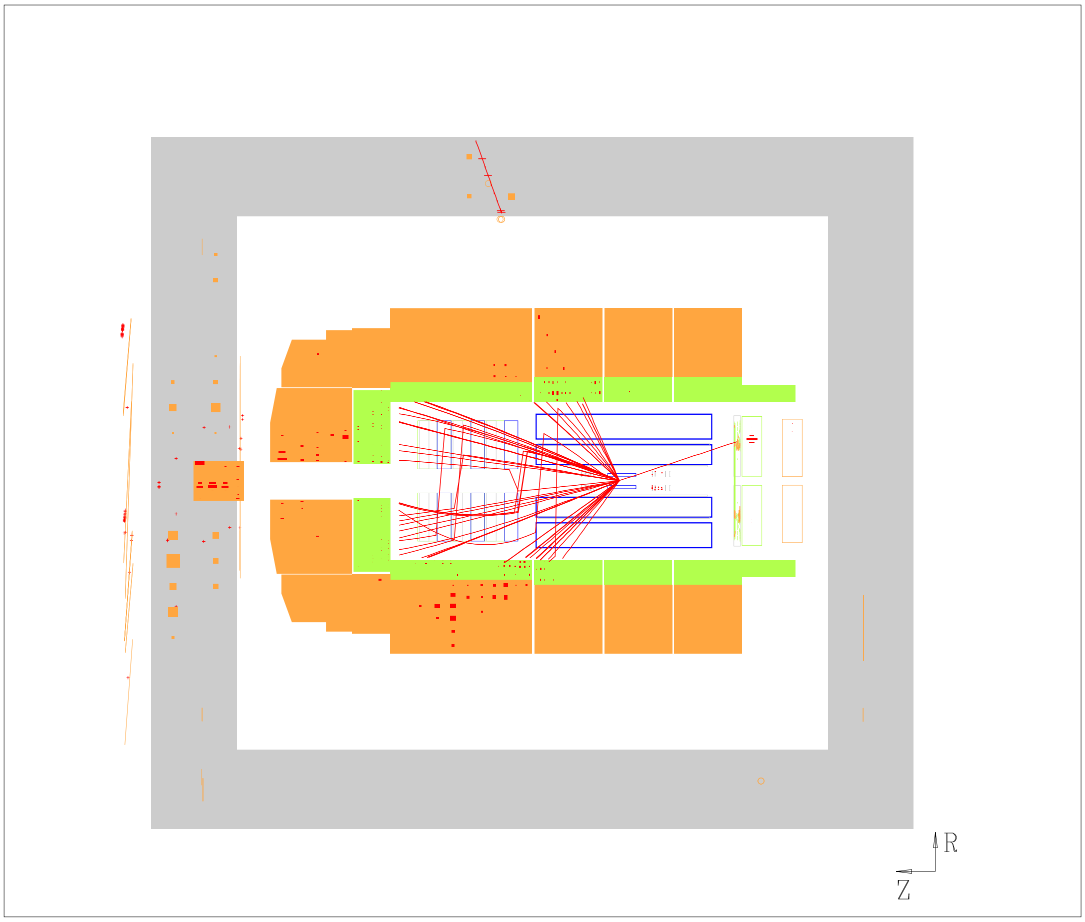

Figure 4.22: *Display of an DIS signal candidate event selected from the H1 data.*

Chapter 5

Cross Section Measurement

This chapter describes the measurement of the beauty production cross section based on the event selection discussed in the previous chapter and following the methods and strategy outlined in Chapter 3. The visible cross section is defined and the determination of the signal content in the selected H1 data, using the beauty sensitive observables defined in Section 3.3, is described. After a discussion of the systematic errors the chapter concludes with a summary of the cross section results.

5.1 Definition of the Visible Cross Section

The cross section definition is adopted from [50]:

$$\sigma^{vis}(ep \to bX \to \mu X) = \frac{f_b N_\mu}{2\epsilon\mathcal{L}} \quad . \tag{5.1}$$

Here, N_μ is the number of muon candidates selected from H1 data (corresponding to an integrated luminosity $\mathcal{L}$) from which a fraction f_b is due to beauty production and ϵ denotes the efficiency for a $b\bar{b}$ event with a primary or secondary muon in the visible range to fulfil the selection and trigger requirements. The factor of 2 accounts for the fact that the experiment measures muons from b and $\bar{b}$ decays. The visible range is defined by the transverse momentum and the polar angle of the muon,

$$p_t^\mu > 2 \text{ GeV} \quad \text{and} \quad 35^\circ < \theta^\mu < 130^\circ \quad , \tag{5.2}$$

and the chosen kinematic region, which is given by

$$\begin{array}{lll} Q^2 < 1 \text{ GeV}^2 & , & 0.1 < y < 0.8 \quad \text{and} \\ 2 \text{ GeV}^2 < Q^2 < 100 \text{ GeV}^2 & , & 0.05 < y < 0.7 \end{array} \tag{5.3}$$

for the photoproduction and DIS measurements respectively. According to the AROMA simulation, the visible γp (DIS) range corresponds to 5% (1%) of the total phase space for semi–muonic beauty decays.

5.2 Photoproduction Analysis

Following the analysis strategy outlined in Section 3.4, the first cross section measurement presented in this thesis is performed in the photoproduction regime using the impact parameter as the sole observable in the f_b determination. In photoproduction the available statistics is considerably larger than in deep inelastic scattering. Also, in contrast to beauty production in DIS, beauty photoproduction has already been measured at H1 using the $p_t^{\rm rel}$ method. Thus, a δ–based γp analysis is well suited to establish the impact parameter method as a new analysis technique at H1. Also, since a different data set is used here, this measurement can be used to obtain a largely independent confirmation of the earlier result. While these aspects are rather technical, the main motivation for this new analysis is to provide an improved cross section measurement. For this purpose a second analysis of the same data set is performed combining the two observables.

In the following discussion the emphasis lies on the statistical extraction of the beauty content in the data from the δ and $p_t^{\rm rel}$ spectra. The fit method has been adopted from [67] and is described in Appendix A. An overview of the event samples used in this procedure is given in Section 4.8. The H1 data sample ($\mathcal{L} = 11.6\ \mathrm{pb}^{-1}$) consists of 1133 muon candidates.

5.2.1 Impact Parameter Analysis

For each muon candidate the $r\varphi$ impact parameter δ as defined in Section 3.3 is calculated using CST improved track and vertex information, cf. Section 4.3 and 4.4 respectively.

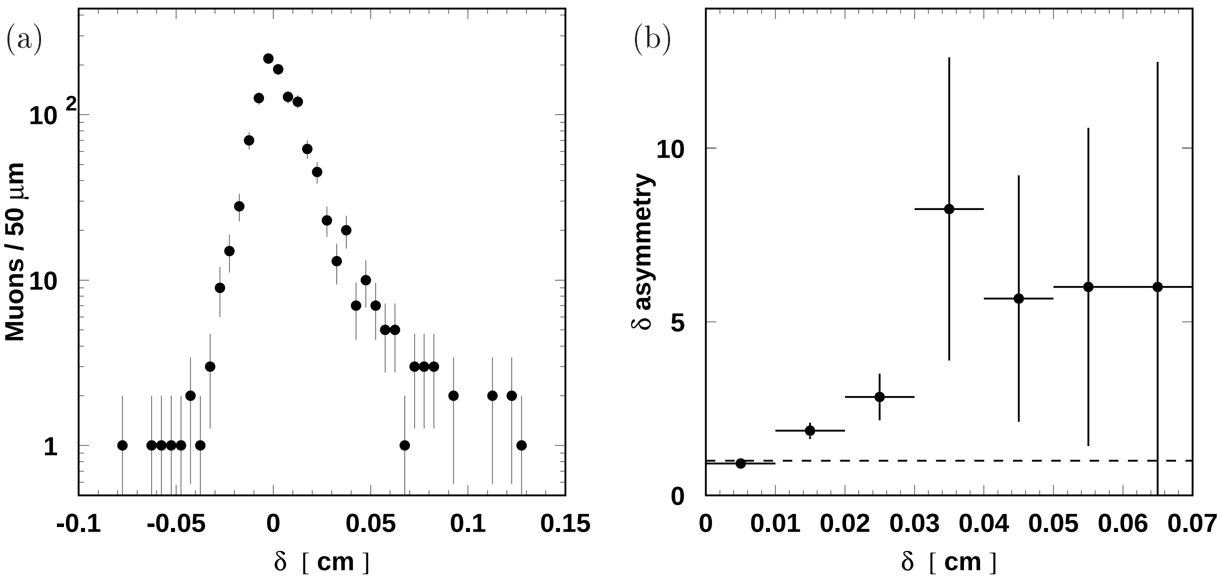

Figure 5.1: *(a) Impact parameter spectrum for the final H1 photoproduction data sample. The asymmetry of this distribution is demonstrated in (b) where the $\delta > 0$ part of the spectrum has been divided by the $\delta < 0$ part.*

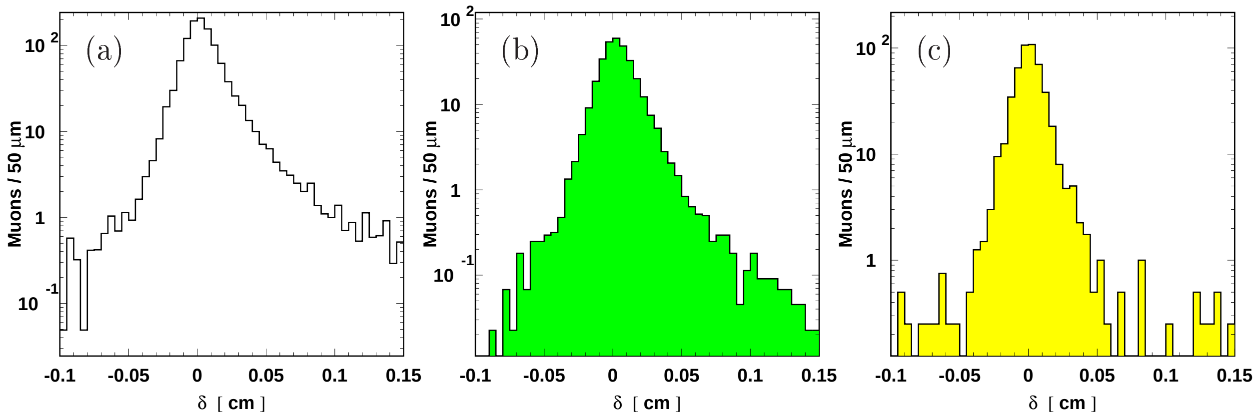

Figure 5.2: *Reconstructed δ distributions for the different MC samples: (a) beauty, (b) charm, (c) fake muons.*

The reference axis, which is needed to define the sign of δ, is taken as the direction of the muon jet three–momentum vector provided by the jet algorithm, from which the muon momentum has been subtracted:[1]

$$\vec{A}_{jet} = \vec{p}_{jet} - \vec{p}_{\mu} \quad . \tag{5.4}$$

Figure 5.1(a) shows the reconstructed muon impact parameter spectrum for the H1 photoproduction sample. The distribution in the unphysical region of negative δ reflects the finite resolution of the impact parameter reconstruction. As demonstrated in Figure 5.1(b), the distribution is clearly not symmetric around $\delta = 0$, the excess at positive delta indicating a relevant contribution from long–lived particle decays. This can already be taken as a qualitative proof for the existence of a significant lifetime signal.

To exploit this in a quantitative measurement, the fit procedure as described in Appendix A is applied to the impact parameter distribution using as further input the δ spectra obtained from the beauty, charm and fake muon MC samples, cf. Figure 5.2. The lifetime signature is much more pronounced for muons from beauty decays than in the charm case. The slight δ asymmetry for the fake muon sample arises from light meson decays in flight (see Appendix B). Comparing the spectra for the three MC sources, a good signal separation can be expected from the fit. Distinguishing semi–muonic charm decays from fake muons will turn out to be more difficult.

The sample decomposition is determined by the impact parameter fit to

$$\begin{aligned} f_b &= [27.2 \pm 5.7]\,\% \\ f_c &= [28.6 \pm 14.4]\,\% \\ f_f &= [44.2 \pm 11.0]\,\% \quad . \end{aligned} \tag{5.5}$$

[1]The exclusion of the muon from the reference axis calculation has been adopted from the earlier H1 measurement, where, however, the jet thrust axis was used instead of the momentum $\vec{p}_{jet}$. As a systematic cross check, the analysis has also be performed with the muon included in the reference axis, i.e. $\vec{A}_{jet} = \vec{p}_{jet}$ (see Section 5.4).

Here, f_b, f_c and f_f denote the proportions of beauty decays, charm decays and fake muons respectively. Only the statistical errors are given, which include contributions from the limited statistic of the MC reference samples. The signal fraction f_b corresponds to an absolute number of 307 ± 65 muons from semi–muonic beauty decays within the selected H1 data sample.

The result is illustrated in Figure 5.3. The fit gives a good description of the data ($\chi^2/n.d.o.f. = 0.96$) over the whole δ range. In the region of negative δ this indicates a good understanding of the reconstruction resolution, including non–Gaussian tails. The well–described large positive impact parameter region shows that also the signal dominated part of the data is under control, which adds confidence to the fit result for the beauty fraction in the data.

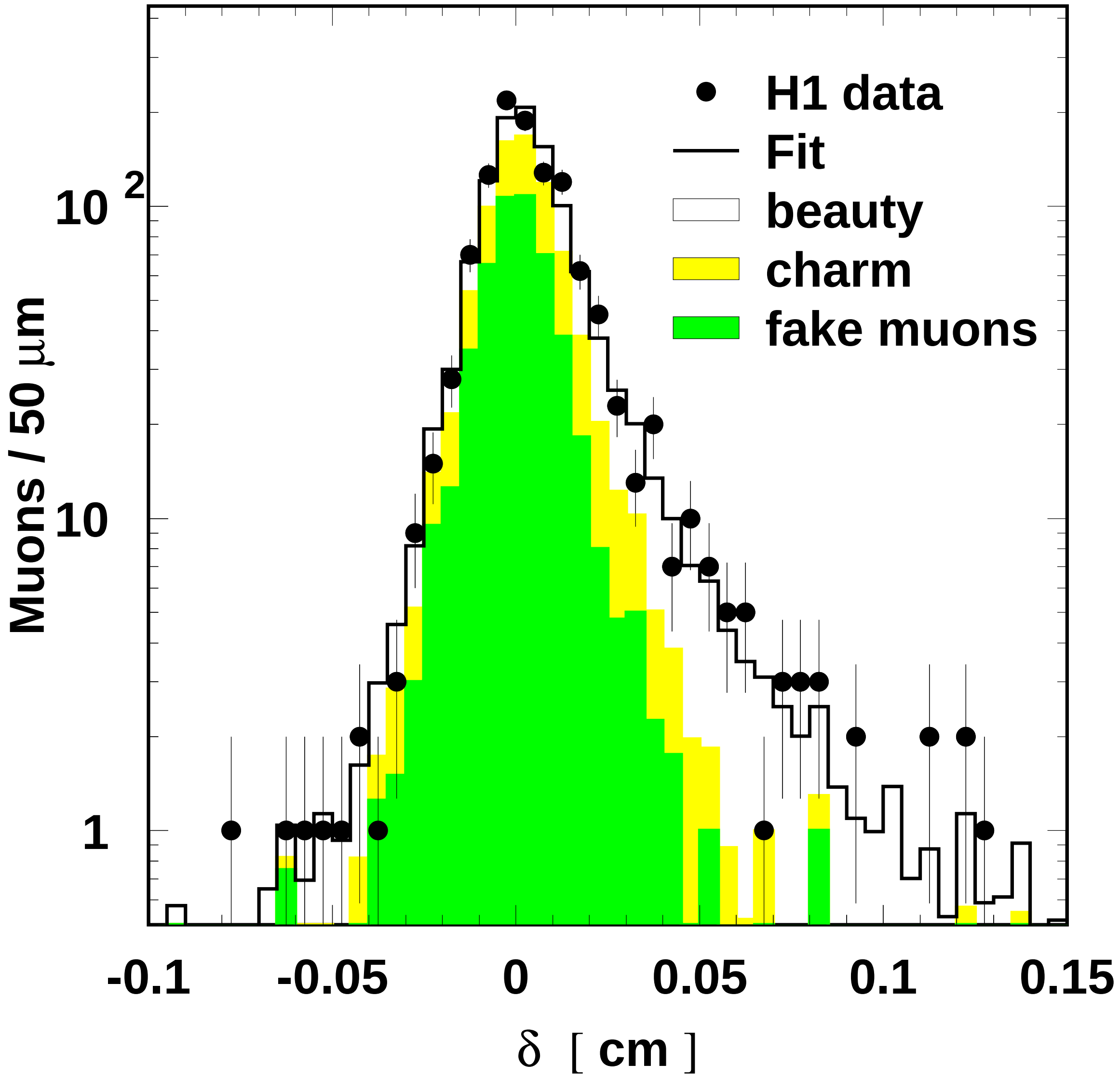

Figure 5.3: *Impact parameter distribution for the photoproduction sample and decomposition from the likelihood fit.*

Compared to f_b, the charm and fake contributions are determined with considerably larger uncertainties, because the separation of those two sources by the fit is relatively weak. This reflects also in a strong negative correlation of $\rho_{c,f} = -0.92$, whereas the signal–background correlation coefficients are $\rho_{b,c} = -0.75$ and $\rho_{b,f} = -0.51$ respectively.

Using (5.1) with the above values for the integrated luminosity and the trigger and selection efficiency, f_b translates into a visible cross section of

$$\sigma^{vis}_{\gamma p} = [142 \pm 30(stat.)] \text{ pb} \quad . \tag{5.6}$$

Although only the statistical error is given here, this agrees within errors with the earlier H1 result of $\left[176 \pm 16(stat.)^{+26}_{-17}(syst.)\right]$ pb, based on an independent method and an independent data set.

Parametrised momentum and polar angle dependent mis–identification probabilities adopted from the earlier H1 analysis of semi–muonic beauty decays can be used to obtain an independent prediction f_f^{ext} for the fake muon contribution from an H1 inclusive track data sample (cf. Appendix B). The result, $f_f^{ext} = (45 \pm 5)\%$, agrees very well with the fake contribution determined in the impact parameter fit.

5.2.2 Combined (δ , p_t^{rel}) Analysis

The impact parameter measurement can be considerably improved by adding the separation power of the second observable p_t^{rel} in a fit to the two–dimensional (δ , p_t^{rel}) distribution. Before doing that, however, the consistency of the two observables needs to be verified.

δ–p_t^{rel} Consistency

For each muon candidate the transverse momentum p_t^{rel} relative to an associated jet as defined in Section 3.3 is calculated using (5.4) to define the jet reference axis.

If p_t^{rel} and δ provide a consistent description of the data, the sample decomposition obtained in the impact parameter analysis should also be appropriate to model the H1 data p_t^{rel} spectrum using the same Monte Carlo samples. As can be seen in Figure 5.4, this is indeed the case for both small and larger p_t^{rel} values.

Using the p_t^{rel} spectrum instead of the δ distribution to determine the signal fraction in the data, it turns out that stable results are achieved only if the contribution from one of the background sources is fixed externally. This is due to an insufficient separation of charm and fake muon processes by this observable and was already observed in the earlier H1 measurement. Using the absolute external estimate $f_f^{ext} = 45\%$ (see above) for the fake contribution in the p_t^{rel} fit yields

$$\begin{aligned} f_b &= [25.0 \pm 3.1 \pm 1.1]\,\% \\ f_c &= [29.8 \pm 3.6 \pm 4.0]\,\% \end{aligned} \tag{5.7}$$

for the proportions of the other two sources in the data. Here, the first error results from the fit itself while the second error also considers the statistical uncertainty of ±5% on f_f^{ext}. Within the errors, the beauty contribution f_b agrees well with the result (5.5) from the impact parameter analysis.

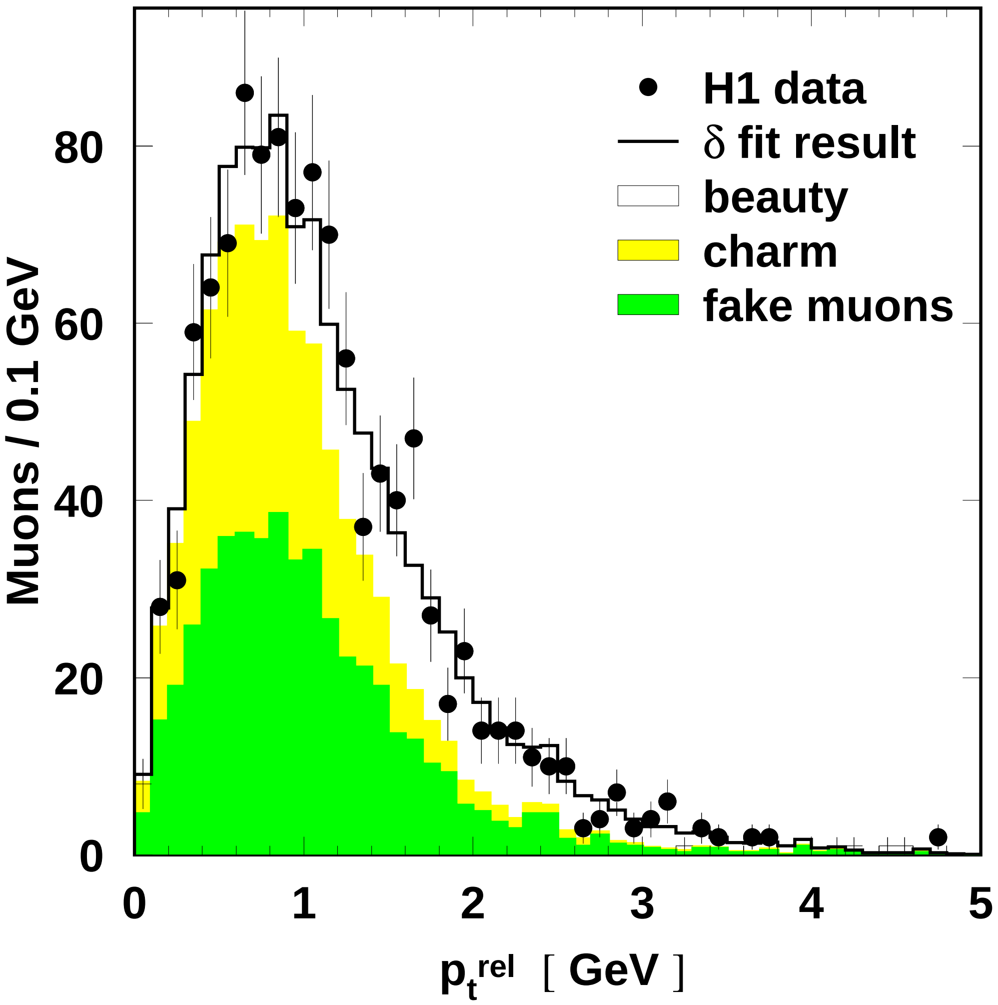

Figure 5.4: $p_t^{\rm rel}$ *distribution and decomposition obtained in the impact parameter analysis.*

In order to further establish the consistency of the two observables, the b component in the events is enriched by restricting the range of one variable and then studying the distribution of the other. Figure 5.5 shows the observed δ spectrum obtained after a cut $p_t^{\rm rel} > 1.5$ GeV. The different contributions, shown in Figure 5.5(a), are the absolute predictions from the δ fit for the limited $p_t^{\rm rel}$ region. Figure 5.5(b) shows the $p_t^{\rm rel}$ spectrum after a cut on $\delta > 400$ μm. Although both spectra clearly demonstrate the presence of a sizeable beauty component and show an overall acceptable description of the H1 data by the fit, they are also both consistent with the b contribution being moderately overestimated. The statistics, however, is not sufficient to draw more quantitative conclusions.

(a)

(b)

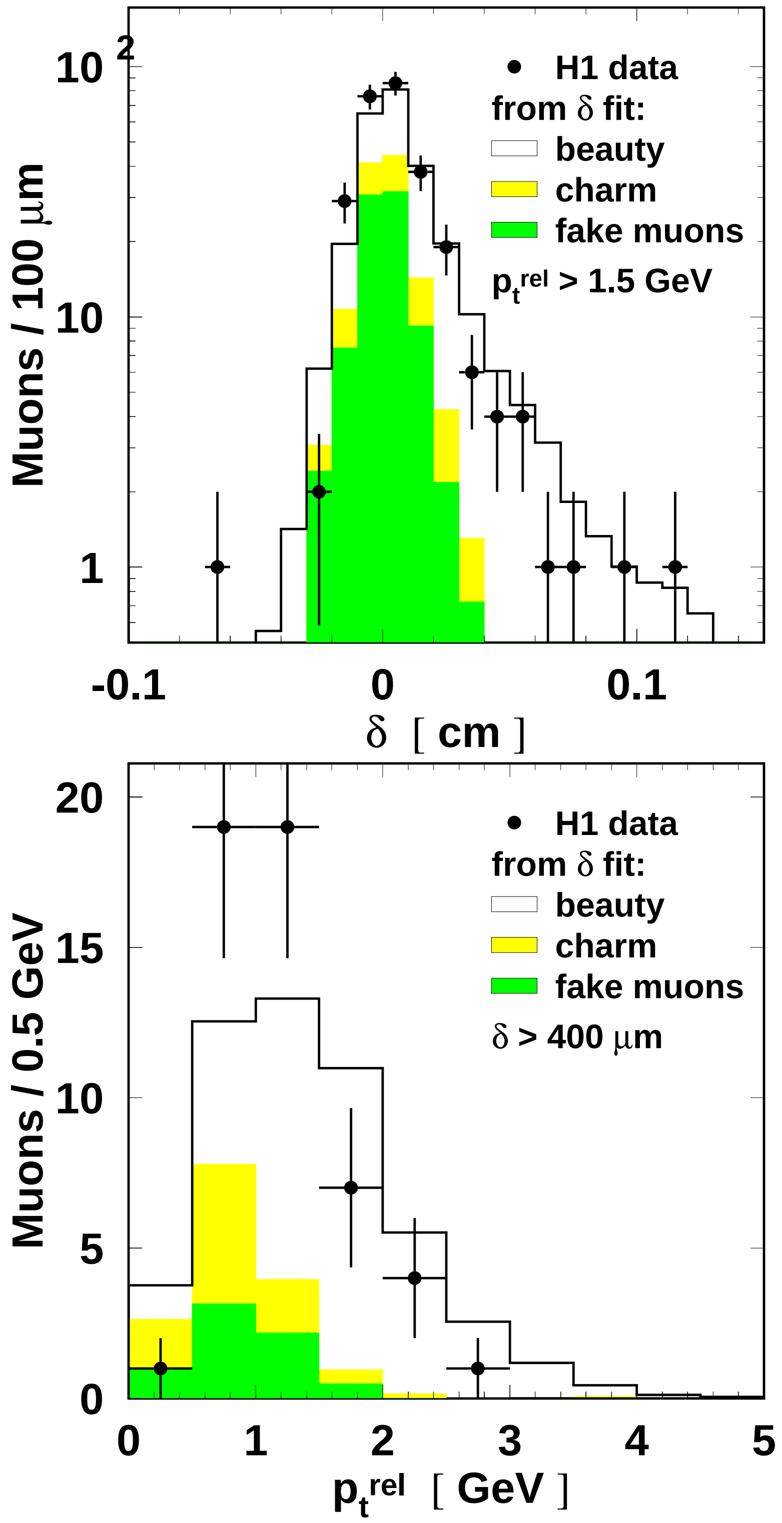

Figure 5.5: *(a) Impact parameter distribution for muon candidates with $p_t^{\rm rel}$ > 1.5 GeV and (b) $p_t^{\rm rel}$ distribution for muon candidates (γp) with $\delta > 400\ \mu m$, together with the MC prediction using the decomposition from the δ fit to the entire photoproduction sample.*

Combined Fit

Having shown that using p_t^{rel} and δ individually in the analysis yields a consistent description of the signal content in the data, the separation power of the two observables can be combined in a two–dimensional fit. The $(\delta\,,\,p_t^{\mathrm{rel}})$ distributions used as input to the fit are shown in Figure 5.6. As has already been discussed in Chapter 3 for the corresponding generator level quantities, there is no strong correlation between the two observables and, also for beauty decays, it is not too likely to find muons with both a very large impact parameter and an exceptionally high p_t^{rel}. The signal can be enriched by selecting events from the tail of either observable but these two beauty–enriched event samples will be largely independent from each other. Thus, a significant improvement of the measurement can be expected if one uses the two–dimensional distribution in the fit instead of fitting the two observable spectra separately.

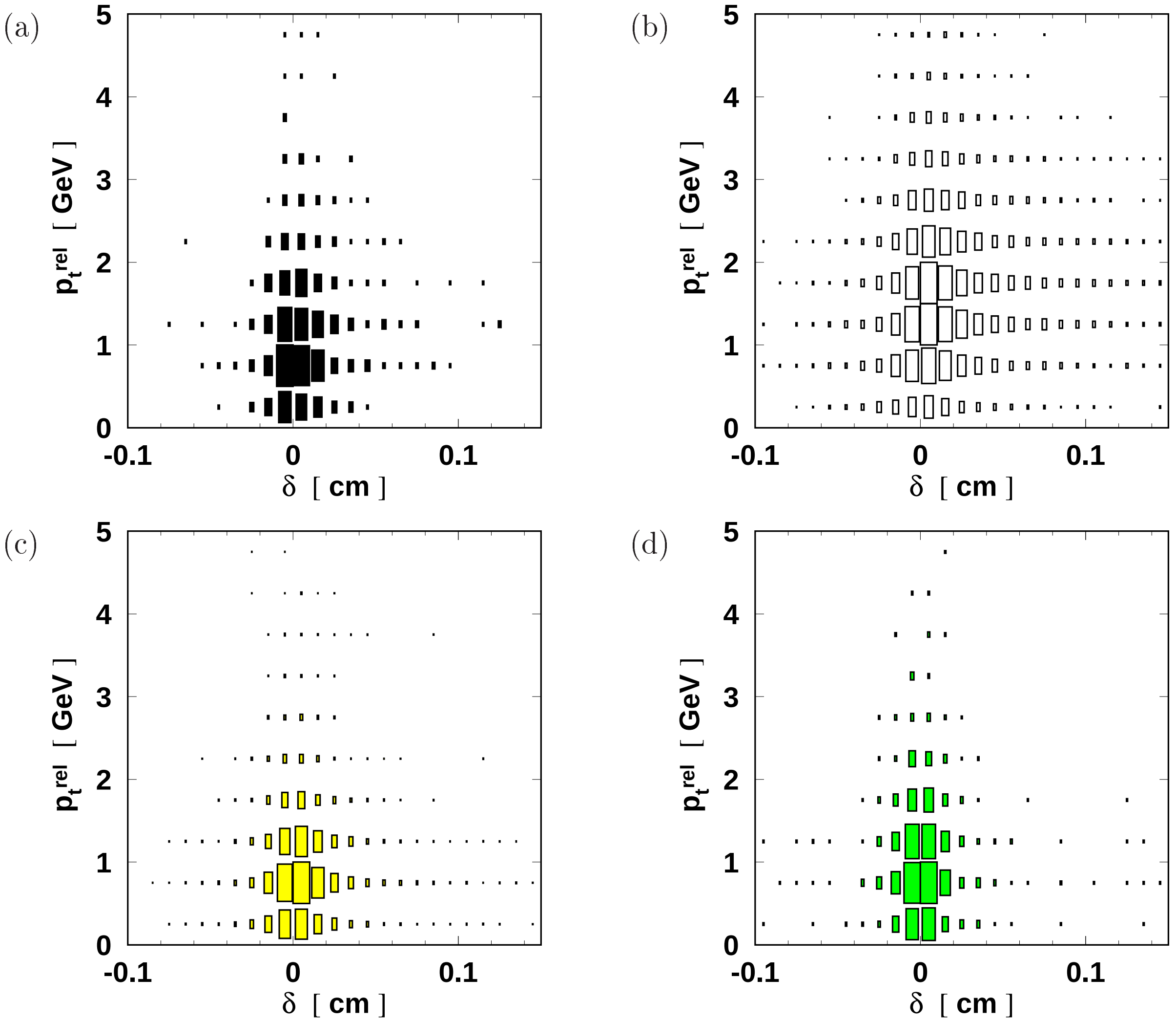

Figure 5.6: *Input distributions to the two–dimensional $(\delta\,,\,p_t^{\mathrm{rel}})$ fit from the the photoproduction samples for (a) H1 data, (b) beauty, (c) charm and (d) fake muons.*

The fit yields the following sample decomposition:

$$\begin{aligned} f_b &= [25.4 \pm 3.0]\,\% \\ f_c &= [31.8 \pm 7.2]\,\% \\ f_f &= [42.9 \pm 7.7]\,\% \end{aligned} \tag{5.8}$$

with correlation coefficients $\rho_{b,c} = -0.02$, $\rho_{b,f} = -0.27$ and $\rho_{c,f} = -0.87$ and a good $\chi^2/n.d.o.f.$ of 0.82. The quality of the fit is also illustrated in Figure 5.7, where a two–dimensional pull distribution is shown. The size of the entry in a particular bin corresponds to the difference between the fit result and the data divided by the statistical error for that bin. Shaded regions denote a positive deviation of the fit result from the data, negative deviations are represented by open squares. For the bulk of the data, neither the size nor the sign of the pull distribution indicates a significant structure, suggesting that a good overall description of the H1 data is given by the fit result. Only in the region where both δ and $p_t^{\rm rel}$ are large the fit tends to be systematically above the data, which has already been observed for the impact parameter fit (see Figure 5.5). Again, however, the overshoot is moderate (well below one standard deviation) for all bins within this phase space region.

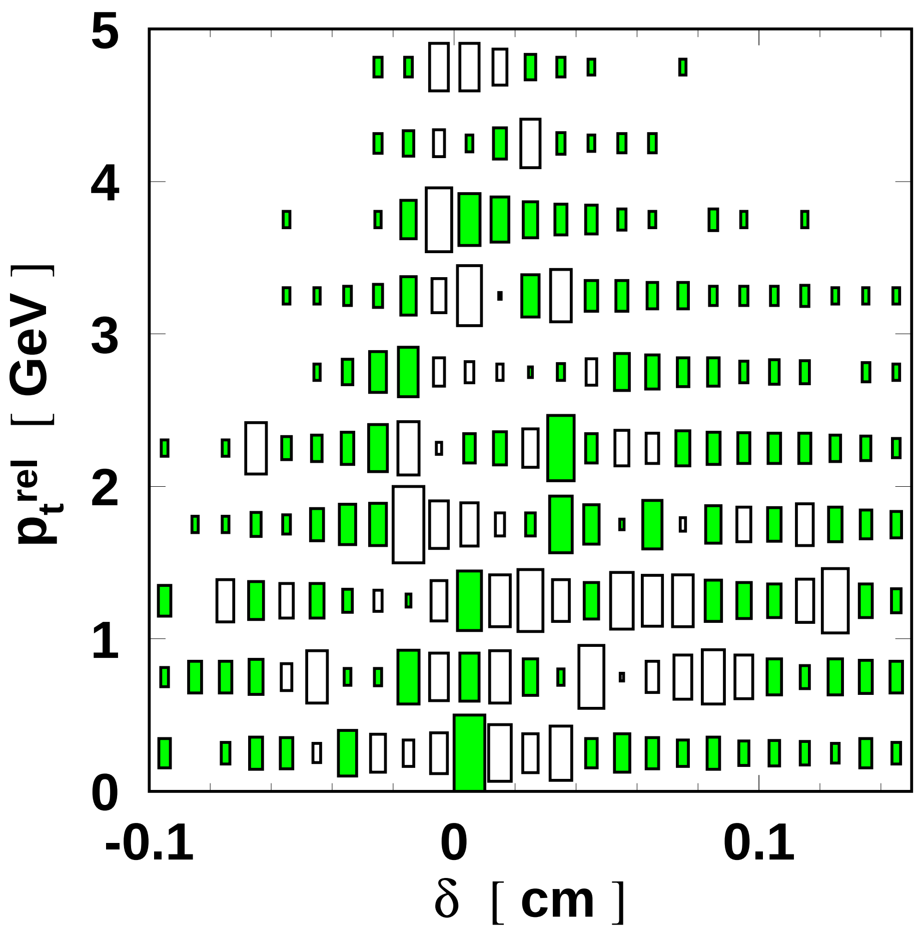

Figure 5.7: *Pull distribution for the two–dimensional (δ , $p_t^{\rm rel}$) fit.*

The agreement of f_f with the independent estimate of the fake contribution found for the δ analysis also holds for the statistically more significant result of the two–dimensional fit.

The signal fraction determined by the fit translates into a visible cross section of

$$\sigma_{\gamma p}^{vis} = [132 \pm 16(stat.)] \text{ pb} \quad . \tag{5.9}$$

This agrees with the impact parameter result (5.9) and is also compatible with the earlier H1 measurement. Compared to the impact parameter measurement, the statistical error is considerably smaller (by a factor 1.7), which illustrates the increased separation power of the fit with the combination of the two observables.

5.3 DIS Analysis

Having established the new method in the photoproduction regime, it can now be used to measure beauty production in deep inelastic ep scattering. For the smaller DIS sample, only the two–dimensional distribution in δ and p_t^{rel} is used for a cross section measurement. The fits to the one–dimensional distributions are performed as cross checks only.

This part of the analysis is based on similar data samples as in the photoproduction case but this time a DIS selection is applied as described in Section 4.6.2. For the H1 data ($\mathcal{L} = 10.5 \text{ pb}^{-1}$) this results in a sample of 187 muon candidates found in 183 different events. Again, AROMA is used to model beauty and charm production processes. The fake muon background is obtained from DJANGO. More details on these event samples can be found in Section 4.8.

The two–dimensional distributions in δ and p_t^{rel} for the different fit input samples are shown in Figure 5.8. In spite of the reduced statistics, the characteristic features which have been discussed above for the photoproduction case are also clearly visible here.

The fit ($\chi^2/n.d.o.f. = 0.9$) results in

$$\begin{aligned} f_b &= [24.7 \pm 7.8]\,\% \\ f_c &= [49.3 \pm 14.0]\,\% \\ f_f &= [26.0 \pm 15.8]\,\% \quad . \end{aligned} \tag{5.10}$$

The correlation coefficients are $\rho_{b,c} = 0.10$, $\rho_{b,f} = -0.46$ and $\rho_{c,f} = -0.81$.

As shown in Figure 5.9, the fit result gives a good description in both projections. The need for a significant signal component is evident from the lifetime based signature as well as from the p_t^{rel} spectrum.

Likelihood fits to the individual observable spectra can be used to cross check the combined analysis of both observables. The δ and p_t^{rel} analysis yield a beauty contribution of $f_b = [23.9 \pm 13.8]\,\%$ and $f_b = [22.0 \pm 7.1 \pm 1.3]\,\%$ respectively. Within the statistical uncertainty, this is consistent with the result of the two–dimensional fit. For the one–dimensional p_t^{rel} fit, again the fake muon fraction f_f had to be fixed externally. Using the parametrised mis–identification probabilities in combination with tracks selected from H1 DIS data yields an estimate for the relative fake muon contribution of $f_f^{ext} = (36 \pm 5)\%$, which is considerably above but within the large errors consistent with the f_f value obtained from the fit.

The fit result (5.10) corresponds to a visible beauty production cross section of

$$\sigma_{DIS}^{vis} = [24.7 \pm 7.8(stat.)] \text{ pb} \quad . \tag{5.11}$$

As in the γp case, only the statistical uncertainty is given here. The systematic error contributions are discussed in the following section.

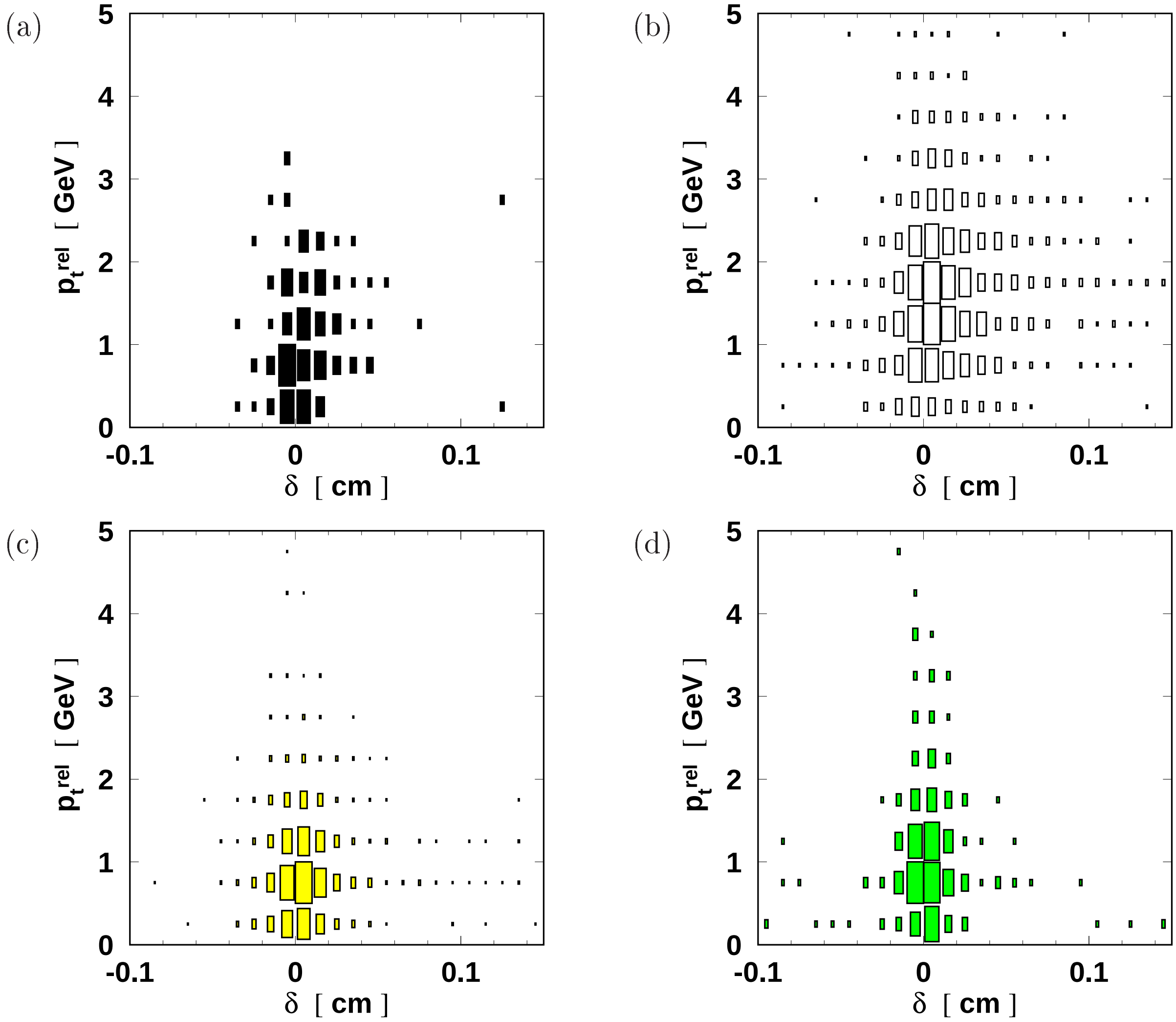

Figure 5.8: *Input distributions to the two–dimensional $(\delta\,,\,p_t^{\rm rel})$ fit from the DIS samples for (a) H1 data, (b) beauty, (c) charm and (d) fake muons.*

(a)

(b)

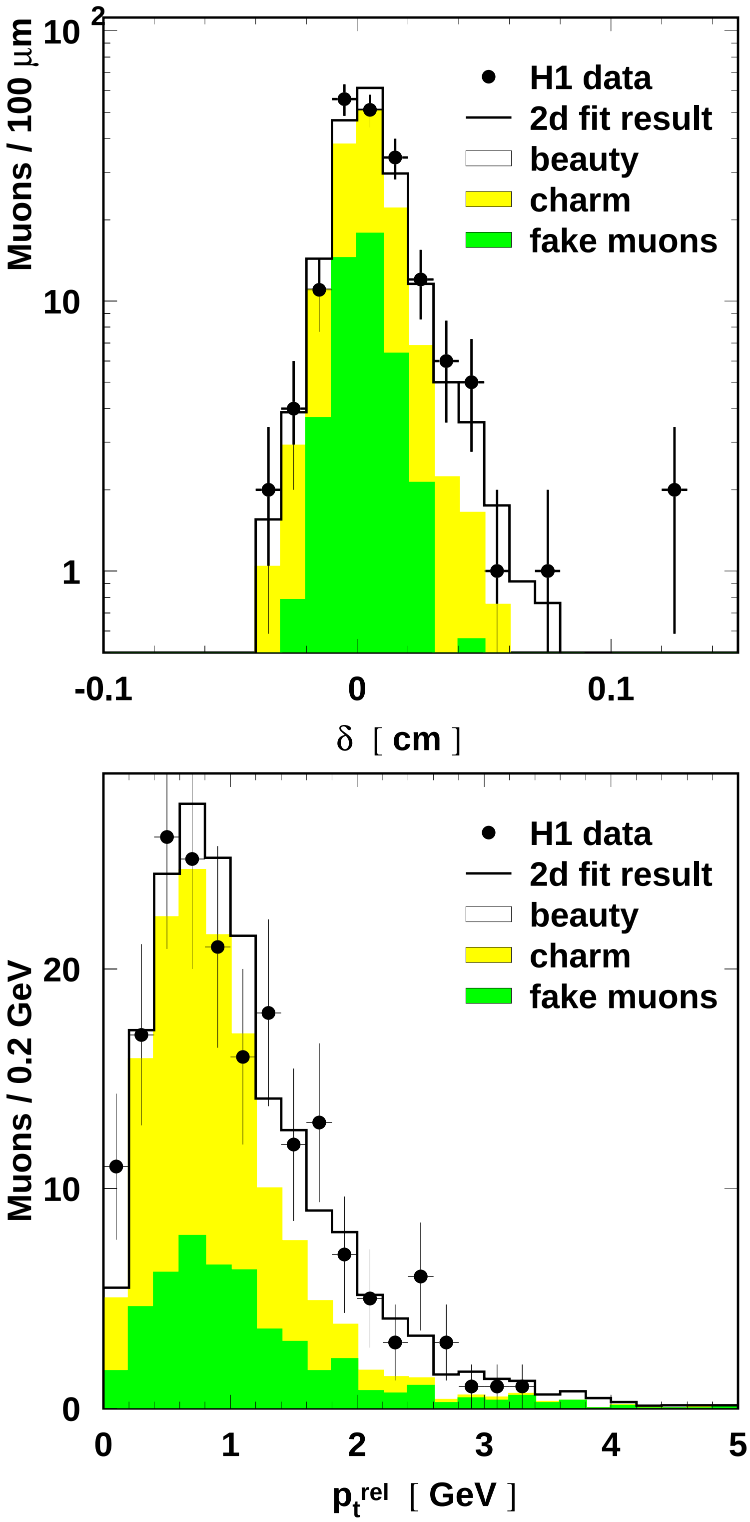

Figure 5.9: *Distributions of (a) the impact parameter and (b) p_t^{rel} for the DIS sample with the decomposition from the combined fit.*

5.4 Systematic Errors

Various aspects in the analysis have been varied in order to evaluate the systematic errors associated with the measured cross sections. Most of the error contributions have been determined using the larger photoproduction sample and are adopted for the DIS cross section after having checked that the DIS result remains stable within the statistical error. Table 5.1 summarises the relevant effects. More details are given below.

MC Model

Two alternative MC event generators, CASCADE and RAPGAP, have been used to simulate beauty production event samples. Unlike AROMA, CASCADE is not based on DGLAP parton evolution but implements the CCFM approach (see Section 1.3.1). RAPGAP includes contributions from resolved photon processes (cf. Section 1.3.2), which are not considered in AROMA.

The γp signal acceptance changes by 8% and 3% with respect to AROMA for CASCADE and RAPGAP respectively. The systematic error associated with the choice of a particular MC model is, consequently, taken to be 8%.

<table>
<tr><th rowspan="3"></th><th colspan="3">relative systematic error</th></tr>
<tr><th colspan="2">γp</th><th>DIS</th></tr>
<tr><th>δ</th><th>$(\delta\,,\, p_t^{\mathrm{rel}})$</th><th>$(\delta\,,\, p_t^{\mathrm{rel}})$</th></tr>
<tr><td>MC model</td><td colspan="3">$\pm 8\%$</td></tr>
<tr><td>μ reconstruction</td><td colspan="3">$\pm 8\%$</td></tr>
<tr><td>δ reconstruction</td><td>$\pm 10\%$</td><td colspan="2">$\pm 6\%$</td></tr>
<tr><td>hadronic energy scale</td><td colspan="3">$\pm 8\%$</td></tr>
<tr><td>jet reconstruction</td><td>$\pm 5\%$</td><td colspan="2">$(+5\ /-10)\%$</td></tr>
<tr><td>fake muon model</td><td colspan="3">$\pm 10\%$</td></tr>
<tr><td>trigger efficiency</td><td colspan="2">$\pm 6\%$</td><td>$\pm 4\%$</td></tr>
<tr><td>kinematic reconstruction</td><td colspan="2">$\pm 2\%$</td><td>$\pm 3\%$</td></tr>
<tr><td>Luminosity</td><td colspan="3">$\pm 1.5\%$</td></tr>
<tr><td>$\sum$</td><td>$\pm 21.4\%$</td><td>$+19.9\%$
-21.7%</td><td>$+19.5\%$
-21.3%</td></tr>
</table>

Table 5.1: *Contributions to the systematic error.*

Muon Reconstruction Efficiency

In the determination of the cross section, imperfections in the description of the CJC and CST tracking efficiency are accounted for by global correction factors. 50% of these corrections are included in the systematic error. In addition, a 5% error is associated with the efficiency of the muon identification in the instrumented iron. This results in a total error on the muon reconstruction efficiency of $\pm 8\%$.

Impact Parameter Reconstruction

Various technical studies have been performed in order to investigate systematic effects associated with the reconstruction of the muon impact parameter. For example, the analysis has been restricted to positively and negatively charged muon candidates respectively or to different regions of the muon azimuthal angle, the latter study being motivated by the different size of the HERA beam spot in the horizontal and the vertical direction and variations of the track reconstruction efficiency with φ. The effect of the manipulation of the CST and drift chamber resolution in the simulation (see Section 4.3) has also been studied as well as changes in the δ fit result following a variation of the beauty hadron lifetimes used in the simulation.

For the impact parameter measurement, all cross section variations seen in this procedure are smaller than 10%. The combination with the second observable p_t^{rel}, which is not affected by the details of the precision tracking and vertexing, reduces the systematic error contribution from this source to 6%.

Hadronic Energy Scale

The systematic uncertainty on the hadronic energy measurement in the LArC has been determined in inclusive analyses to be $\pm 4\%$ and the hadronic energy scale used in the MC simulation is varied accordingly. The observed effects on the cross section are compatible with being exclusively due to a changed acceptance with respect to the cut on the minimum jet E_t and translate into a systematic error contribution of $\pm 8\%$, which is relevant for all measurements.

Jet Reconstruction

As stated in Section 4.5, several indications of imperfections in modelling the jet axis resolution in the H1 data by the MC simulation have been seen. Comparing the p_t^{rel} distributions for measured and simulated inclusive track samples suggests to enlarge the jet $\eta\varphi$ resolution by 15%, cf. Figure 4.17. In order to translate this observation into a systematic error, the analysis is repeated after having applied this jet direction smearing to one or all of the MC samples. The cross section obtained from the impact parameter measurement remains unchanged, but systematically lower results are found for the two–dimensional fit. The largest effect of -9%, which is seen for a simultaneous manipulation of all MC sources, is included in the systematic error for the combined $(\delta\,,\,p_t^{\rm rel})$ measurement.

In Appendix B, two different ways to treat calorimeter energy depositions close to the muon candidate track are discussed. Exchanging one method for the other, which influences both the energy and the direction of the reconstructed muon jet, yields changes in all measured cross sections of about 10%. It should be noted that this reflects the effect of an optimisation procedure rather than a systematic comparison of equally performing methods. There is also some redundancy with the variation of the jet resolution in the MC and of the fake muon model (see below). Therefore, only half of the observed change in the cross section, i. e. $\pm 5\%$, is considered in the systematic error.

In summary, a symmetric error of $\pm 5\%$ is associated with both the impact parameter analysis and the combined $(\delta\,,\,p_t^{\rm rel})$ measurement accounting for the uncertainty arising from the variation of the treatment of calorimetric energy depositions close to the muon. The possible underestimation of the jet axis resolution by the simulation is considered as an independent and purely $p_t^{\rm rel}$–related error contribution, resulting in a total jet reconstruction error for the combined $(\delta\,,\,p_t^{\rm rel})$ cross section of $(\pm 5 \oplus -9)\% \approx (+5\;\;/-10)\%$.

Fake Muon Model

For all measured cross sections a systematic error of $\pm 10\%$ accounts for the choice of a particular approach to model the fake muon background (see Appendix B). This effect has been quantified via a variation of the relative contribution from in–flight decays of light mesons in the simulation by $\pm 50\%$ and by modelling the punch–through contribution with inclusive track samples from data and MC respectively instead of using the fake muon MC sample.

Trigger Efficiency

The statistical uncertainties in the determination of the trigger efficiencies translate into systematic errors of 6% and 4% for the photoproduction and DIS measurements respectively. The photoproduction error includes a contribution from the inefficiency of the muon trigger L4 verification (see Section 4.7.2), which is not an issue for the SpaCal–based DIS trigger.

Other Contributions

Additional small contributions to the systematic error arise from the uncertainty associated with the luminosity measurement (1.5% [68]), the y determination in the γp regime (2%) and the reconstruction of the scattered positron in DIS (3%).

Additional studies

Further systematic studies and cross checks, which did not result in additional contributions to the systematic error, are listed below.

- A variation of some technical aspects in the fit procedure, e.g. the bin sizes in the input distributions, does not reveal any significant effects on the fit results.
- Replacing $\vec{A}_{jet} = \vec{p}_{jet} - \vec{p}_{\mu}$ by the jet momentum $\vec{p}_{jet}$ changes the cross section results by less than 2%.
- As stated in Chapter 4, there are some imperfections in the MC description of the θ distribution for both the muon and the muon jet, the simulation being somewhat below the data in the forward region (cf. Figures 4.2 and 4.18). For this reason, an additional cross section measurement is performed with the jet and muon polar angles restricted to values $> 50°$. This changes the ratio of the measured cross section and the corresponding AROMA prediction by 3% and 11% for the impact parameter analysis and the combined (δ , p_t^{rel}) measurement respectively, which is considered to be sufficiently stable.
- In order to study the dependence of the measured cross sections on the choice of a particular jet algorithm, the analysis is redone using two different implementations of *cone algorithms* (CDFCONE [69] and QJCONE [70, 71] respectively) instead of the inclusive k_t cluster algorithm. In both cases this results in a strongly increased jet E_t acceptance, which in the signal MC amounts to 43% and 34% for CDF-CONE and QJCONE respectively. The size of the H1 data sample increases by 31% (CDFCONE) and 23% (QJCONE). While the impact parameter result changes by less than 4%, the γp cross section from the combined (δ , p_t^{rel}) analysis decreases significantly (by about 20%) in both cases. Even combining all of the above systematic effects which might enter here, this cannot account for the large changes in the cross sections from the combined (δ , p_t^{rel}) analysis, which are of the same order as the total systematic error.

  The increased jet E_t acceptance implies that, compared to the k_t algorithm, the cone algorithms yield broader jets with correspondingly increased energy. The changes in the jet shape obviously destroy the consistency of the two observables. The f_b results obtained from the δ and the two–dimensional fit respectively differ by almost 30% for both cone algorithms. This indicates, that the jets in the additionally opened phase space region are not well modelled. A re–evaluation of the quality of the MC description, possibly including additional tuning, would be needed here. This, however, goes beyond the scope of the systematic variation of this analysis.

  In conclusion, the observed effects are considered to reflect mostly internal inconsistencies in the cone algorithm analysis, which do not compromise the stability of the k_t algorithm–based measurement. In view of the above findings one might, however, want to include the jet kinematics (arising from the choice of a particular jet algorithm) in the definition of the visible cross section.

5.5 Summary of Cross Section Results

In summary, the following cross section results have been obtained:

- The photoproduction analysis using the impact parameter as the only observable yields a visible beauty production cross section of

$$\sigma_{\gamma p}^{vis} = [142 \pm 30(stat.) \pm 30(syst.)] \text{ pb} \quad . \tag{5.12}$$

  The previously published H1 result of $\left[176 \pm 16(stat.)^{+26}_{-17}(syst.)\right]$ pb is thus confirmed, using an independent signature and data set.

- Combining the two observables δ and p_t^{rel} in a two–dimensional fit results in an improved measurement giving

$$\sigma_{\gamma p}^{vis} = \left[132 \pm 16(stat.)^{+26}_{-29}(syst.)\right] \text{ pb} \quad . \tag{5.13}$$

- From a combined $(\delta\,,\, p_t^{\mathrm{rel}})$ analysis the visible cross section for beauty production in DIS is found to be

$$\sigma_{DIS}^{vis} = \left[24.7 \pm 7.8(stat.)^{+4.8}_{-5.3}(syst.)\right] pb \quad . \tag{5.14}$$

In all cases the visible kinematic range is defined by Q^2, y, p_t^{μ} and θ^{μ} according to Equations (5.2) and (5.3).

Chapter 6

Discussion of the Results

In the previous chapter, the discussion of the measured beauty production cross sections has been restricted to the internal consistency of the analysis and a comparison with the earlier H1 measurement. In the following, the results are placed in a more general context.

6.1 Comparison with QCD Predictions

The measured cross sections can be compared directly with results of NLO QCD calculations. For this purpose Monte Carlo integration programs are used, which have been discussed already in Section 1.6. The beauty hadron momenta are obtained from the b quark momenta according to the Peterson fragmentation function (1.30). The fragmentation parameter is set to $\epsilon = 0.0033$ according to a fixed order (α_s^2) QCD fit [28] to beauty spectra measured in e^+e^- annihilation [72] (see also Section 1.5.2). As the muon kinematics enter the definition of the visible cross section (cf. section 5.1), the beauty hadron distributions need to be folded with the muon momentum spectrum, which is extracted from AROMA. Throughout the calculation the b quark mass is set to 4.75 GeV.

Photoproduction

In the γp regime the calculation is performed with the FMNR program. The MRSG [73] and GRV [74] parton densities are used for the proton and the photon respectively. The renormalisation and factorisation scales are set to $\mu^2 = \mu_F^2 = p_{t,b}^2 + m_b^2$. The cross section result for the visible range given by Equations (5.2) and (5.3) is

$$\sigma_{\mathrm{FMNR}}^{vis} = (54 \pm 9) \text{ pb} \quad . \tag{6.1}$$

The error is estimated by varying the scale by factors of two, ϵ between 0.0016 and 0.0069 and m_b between 4.5 GeV and 5 GeV. Here, the dominant contribution ($\pm 11\%$) arises from the b quark mass variation.

The prediction (6.1) undershoots significantly the results of both the impact parameter analysis and the combined (δ , p_t^{rel}) measurement, $\left[142 \pm 30(stat.) \pm 30(syst.)\right]$ pb and $\left[132 \pm 16(stat.)^{+26}_{-29}(syst.)\right]$ pb respectively. This holds also for the AROMA prediction of 38 pb.

DIS

For DIS, a NLO QCD prediction is obtained from the HVQDIS program using the GRV98 parton densities [75] and choosing $\mu^2 = \mu_F^2 = Q^2 + 4m_b^2$. The resulting visible cross section, as defined in Chapter 5, is

$$\sigma^{vis}_{\mathrm{HVQDIS}} = (11 \pm 2)\ \mathrm{pb}\ \ , \tag{6.2}$$

where the error is obtained in the same way as in the photoproduction case. The corresponding AROMA prediction is 9 pb, the CASCADE program yields a visible cross section of 15 pb. All predictions are somewhat below the measured cross section of $\left[24.7 \pm 7.8(stat.)^{+4.8}_{-5.3}(syst.)\right]$ pb.

The HVQDIS result is a factor of ~ 2.2 lower than the measurement. Considering, however, the large experimental error and the uncertainty on the theoretical prediction, this difference corresponds only to about 1.4 standard deviations.

6.2 Comparison with other Measurements

There are two published results of beauty production in ep collisions at HERA. The first measurement, which was based on a muon p_t^{rel} analysis using H1 data taken in 1996, has already been discussed above. In parallel to the work presented in this thesis, the ZEUS collaboration published a beauty photoproduction measurement (based on 1996/97 data) using also the p_t^{rel} method but analysing the electron decay channel.

In addition to the preliminary H1 $ep \to b\bar{b} \to \mu X$ cross sections resulting from the work on this thesis, there are preliminary ZEUS results, also based on inclusive muon data and very recently covering also the DIS regime and differential cross sections.

Recently, also preliminary results on $D^\star$–muon correlations have become available from both H1 and ZEUS, which include measured beauty production cross sections.

ZEUS Electron Analysis

ZEUS has measured beauty production in an electron p_t^{rel} analysis [76] based on data recorded in 1996 and 1997, which correspond to an integrated luminosity of $\mathcal{L} = 38.5\ \mathrm{pb}^{-1}$. In contrast to the H1 analyses, the visible range is not defined by the lepton kinematics but by the two leading jets in the event. A further extrapolation to the region of b quark transverse momenta $p_t^b > 5$ GeV, pseudorapidities $|\eta^b| < 2$, $Q^2 < 1\ \mathrm{GeV}^2$ and $0.2 < y < 0.8$ yields a parton–level cross section of

$$\sigma^{\mathrm{ext}}_{\gamma p} = [1.6 \pm 0.4(stat.)^{+0.3}_{-0.5}(syst.)^{+0.2}_{-0.4}(extrapolation)]\ \mathrm{nb}\ \ , \tag{6.3}$$

which is somewhat above the FMNR result (0.64 nb).

(a)

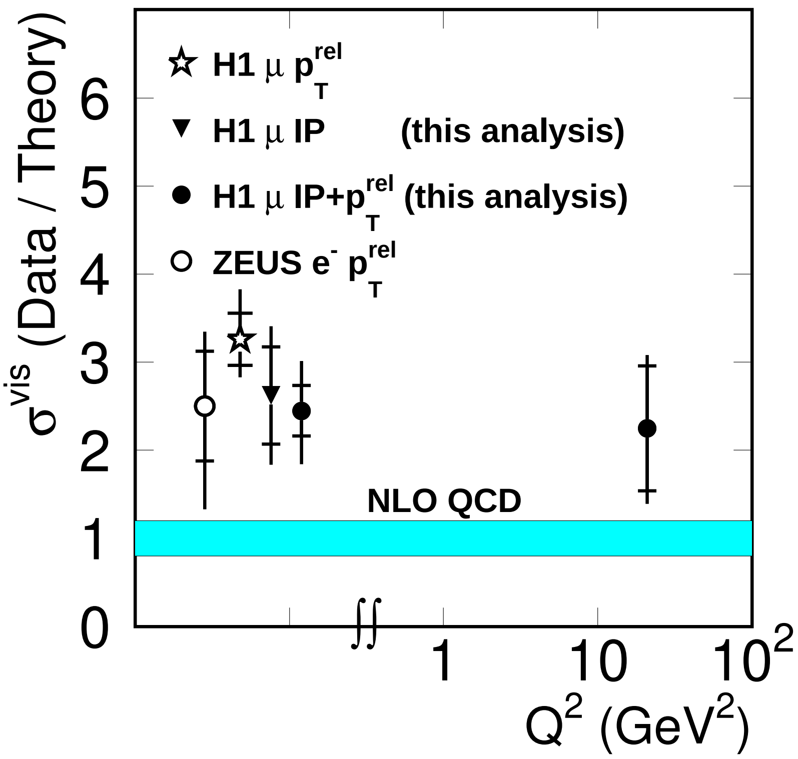

(b)

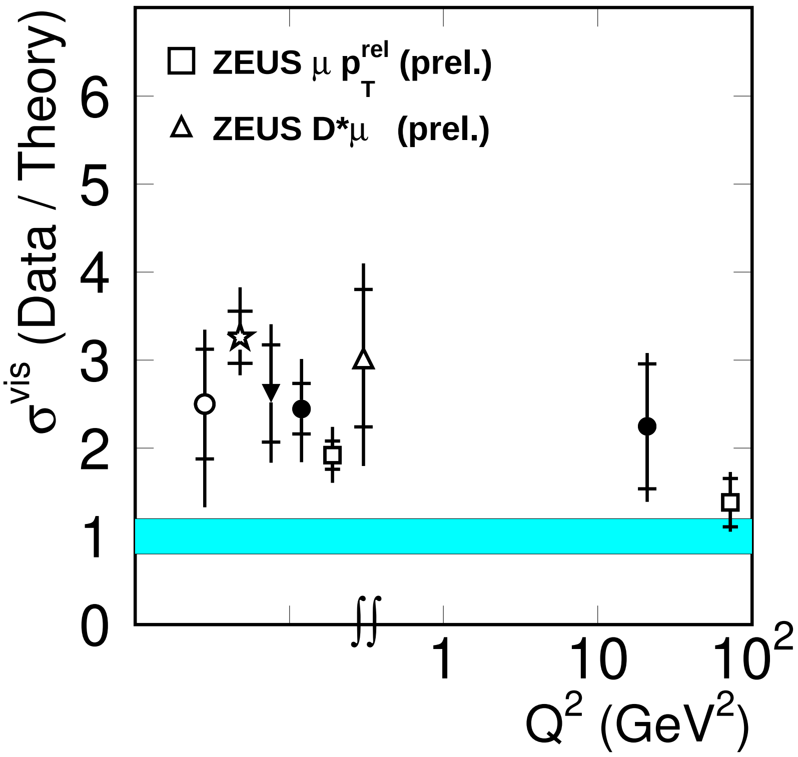

Figure 6.1: *Ratio of measured visible beauty production cross sections at HERA over theoretical expectation as a function of Q^2. Figure (a) shows the results of this analysis together with the earlier published measurements. In (b) the recent preliminary ZEUS results are included in addition.*

ZEUS Muon Analyses

The new preliminary ZEUS results [77, 78] on beauty production have been obtained from $p_t^{\rm rel}$–based measurements in the muonic decay channel using, compared to previous analyses, considerably larger data sets ($\mathcal{L} = 98$ pb^{-1} and $\mathcal{L} = 60$ pb^{-1} for the photoproduction and DIS measurements respectively).

The photoproduction cross section for the process $ep \to b\bar{b} \to 2$ jets $+ X$ is measured for $Q^2 < 1$ GeV^2, $0.2 < y < 0.8$, $p_t^{jet1(2)} > 7(6)$ GeV and $|\eta^{jet1(2)}| < 2.5$. The result,

$$\sigma_{\gamma p}^{ep \to b\bar{b} \to 2jets+X} = [733 \pm 61(stat.) \pm 104(syst.)] \text{ pb} \quad , \tag{6.4}$$

is significantly higher than the NLO QCD prediction of 381^{+117}_{-78} pb, where the parton–level cross section was obtained from FMNR and PYTHIA was used for the parton–to–hadron corrections.

In DIS ($Q^2 >$ GeV^2, $0.05 < y < 0.7$), events containing a muon with $p^\mu > 2$ GeV and $30° < \theta^\mu < 160°$ and at least one jet are selected. Jets are reconstructed in the Breit frame, where a minimum transverse energy of 6 GeV is required. In the laboratory frame, the jet pseudorapidity is restricted to $-2.0 < \eta^{jet} < 2.5$. Both jet and muon kinematics enter the definition of the visible range for the cross section, which is measured to be

$$\sigma_{\gamma p}^{ep \to b\bar{b} \to jet+\mu X} = [38.7 \pm 7.7(stat.)^{+6.1}_{-5.0}(syst.)] \text{ pb} \quad . \tag{6.5}$$

A HVQDIS–based NLO QCD calculation yields $28^{+5.3}_{-3.5}$ pb, which is below but within errors consistent with the measured value.

H1 and ZEUS $D^\star$–Muon Correlation Analyses

Both H1 and ZEUS have recently measured beauty production using the $D^\star\mu$ decay mode. In these analyses, the signal is extracted using the charge correlations and angular distributions of the muon with respect to the $D^\star$ meson. The details can be found in [79] and [80].

Summary

The different cross section results cannot be compared directly because different definitions of the visible range have been used. The ratio of measured cross sections to the corresponding QCD predictions, however, is expected to be unaffected by these differences. Figure 6.1 compares the different HERA results on beauty production in terms of this ratio, which yields the following picture:

- The cross sections from this analysis agree within errors with the other corresponding measurements at HERA.

- In photoproduction, all experimental results exceed the theoretical expectations significantly, the central values being higher by factors between 1.9 and 3.2. This discrepancy is now observed by two different experiments using three largely independent methods and several independent data sets and is thus very well established.

- In the DIS regime the situation is not so clear. The result from this analysis is somewhat above the NLO QCD prediction, thus indicating that the discrepancy between data and NLO QCD is not restricted to the photoproduction regime. The very recent second measurement yields a cross section which agrees within errors with the first analysis but is, however, compatible also with the theoretical expectation. More data is needed here.

Already before the measurements at HERA, NLO QCD had been found to fail in the description of beauty production in $p\bar{p}$ collisions [81, 82, 83, 84]. This has now also been observed in $\gamma\gamma$ scattering [85, 86]. In both cases the direction and level of the discrepancy between data and theory is similar to these observed for ep processes. Considering that for beauty production perturbative QCD is expected to work particularly well, it is rather surprising to consistently find pQCD calculations underestimating the measured cross sections. Identifying the source of the discrepancy is still an open issue, the discussion of which is beyond the scope of this thesis. Recent ideas concern, for example, fragmentation issues [87], the parton evolution model [88] or processes beyond the Standard Model [89, 90].

Chapter 7

Summary and Outlook

Measurements of open beauty production in positron–proton scattering at a centre–of–mass energy of 300 GeV have been presented. In data corresponding to an integrated luminosity of $\mathcal{L} \approx 11\ \text{pb}^{-1}$, which were recorded with the H1 detector at the HERA collider in 1997, beauty–flavoured hadrons were observed through their semi–muonic decay. Cross sections were extracted for two different kinematic regions, photoproduction and deep inelastic scattering respectively, from the distributions of the muon impact parameter δ and of the transverse momentum p_t^{rel} of the muon relative to an associated jet.

Prior to this analysis, all available experimental information on open beauty production in ep collisions had been provided by p_t^{rel}–based inclusive lepton measurements in the photoproduction regime. This measurement was the first at HERA to apply in addition an impact parameter technique to determine the signal contribution in the data, thus making use of the beauty lifetime signature. The new method was successfully established in a photoproduction measurement and was then used to extend the analysis to a different kinematic region, resulting in the first cross section measurement of open beauty production in deep inelastic ep scattering. Preliminary results from these measurements have already been shown in [91] and [92]. This thesis has presented an updated status of the analysis, including additional systematic studies.

The most important experimental device for the impact parameter analysis was the H1 central silicon tracker CST. This measurement was one of the first to use the CST and demonstrated that this detector component is sufficiently well understood to provide track and vertex information with the necessary precision to resolve beauty lifetime effects. An improved method for combining CST signals and drift chamber tracks was found to be vital to perform lifetime studies with the CST and was also developed in the course of this analysis.

The measured beauty production cross sections are summarised in Table 7.1, together with corresponding QCD predictions obtained from NLO calculations in the massive scheme. In a first measurement, the beauty photoproduction cross section was determined using the impact parameter as the only observable. The result agrees within errors with a previously published H1 measurement, which is thus confirmed using an independent signature and data set. Combining the two observables, δ and p_t^{rel}, in a second

	$\sigma^{vis}(ep \to bX \to \mu X')$ [pb]	
	Photoproduction $Q^2 < 1$ GeV^2 $0.1 < y < 0.8$	DIS 2 GeV$^2 < Q^2 < 100$ GeV^2 $0.05 < y < 0.7$
	$p_t^\mu > 2$ GeV, $35° < \theta^\mu < 130°$	
δ analysis	$142 \pm 30(stat.) \pm 30(syst.)$	—
$(\delta\, ,\, p_t^{\mathrm{rel}})$ analysis	$132 \pm 16(stat.)\ ^{+\,26}_{-\,29}\ (syst.)$	$24.7 \pm 7.8(stat.)^{+4.8}_{-5.3}(syst.)$
NLO QCD	54 ± 9	11 ± 2

Table 7.1: *Measured beauty production cross sections and corresponding NLO QCD predictions.*

measurement yielded a cross section consistent with the impact parameter result, the statistical uncertainty being considerably reduced. The measured cross sections were found to be a factor of ~ 2.5 above the NLO QCD prediction. This significant excess of the experimental results over the theoretical expectation is consistently seen for all HERA measurements of beauty photoproduction.

The DIS analysis was based on an event sample about six times smaller than in the photoproduction case. Nevertheless, the combined $(\delta\, ,\, p_t^{\mathrm{rel}})$ analysis yielded a statistically significant observation of beauty production in this previously unaccessed kinematic region. The measured cross section exceeds the QCD expectation by a factor of ~ 2.2. Considering the uncertainty on the theoretical prediction and the large experimental error, this difference corresponds to about 1.4 standard deviations. Within errors, this is compatible with the preliminary result of a very recent measurement by the ZEUS collaboration, which was based on a considerably larger data set. This second measurement is, within errors, compatible with the theoretical prediction.

In conclusion, the analysis presented in this thesis has made relevant contributions to the experimental information on beauty production in high–energy ep scattering. In photoproduction, the discrepancy between measured cross sections and corresponding QCD predictions has been further established. The DIS measurement has provided a first indication that this discrepancy is not restricted to the γp regime. In view of the large experimental uncertainty this, however, needs to be further investigated by future analyses of beauty production in deep inelastic scattering.

Outlook

Perturbative QCD is expected to give a reliable description of beauty production processes. It is, therefore, surprising to find present calculations to significantly underestimate the measured γp cross sections. Similar discrepancies have been seen in corresponding analyses of $p\bar{p}$ and $\gamma\gamma$ data, but a conclusive explanation has until now not been found. Considering also that in deep inelastic ep scattering the conclusion on the agreement between data and theory is presently not clear, there is a strong motivation for further improved measurements of beauty production with H1.

While this analysis is based on data corresponding to an integrated luminosity of 11 pb^{-1}, the total available H1 data set is of the order of 100 pb^{-1}. A further substantial increase is expected in the near future from the upgraded HERA collider and H1 detector, which are presently being commissioned. The most obvious step to improve this measurement is, therefore, to increase the amount of data used in the analysis. With a reduced statistical uncertainty, the systematic error can also be expected to decrease due to a better sensitivity in the evaluation of systematic effects. This way also the combined (δ , p_t^{rel}) photoproduction analysis, which already now is dominated by systematics, will benefit from the increased statistics. A larger data set will also make it possible to perform various differential cross section measurements in order to test the theoretical description of beauty production in more detail. Recent preliminary ZEUS results including differential beauty cross sections can be found in [77, 78].

In future measurements one might also want to improve the signal purity, which would decrease the sensitivity to the modelling of the background. The cross section measurement presented in this thesis is based on an inclusive muon sample which is dominated by background processes, the beauty contribution being at the level of 25%. The large background from mis–identified light hadrons could probably be reduced by tightening the muon identification criteria. Another approach would be to use one of the beauty–sensitive observables to enrich the signal, e.g. by applying a cut on the minimum p_t^{rel}, and determine the signal content in the resulting sample from the distribution of the other observable (δ). With increasing size of the data sample, beauty decays with lower branching ratios gain in relevance, for example the channels $B \to J/\Psi X$ or $B \to D^{\star} X$, which have been studied in [94] and [52] respectively and provide event samples almost free of light flavour–induced background. These channels also extend the accessible phase space towards lower p_t because a jet requirement is, in principle, not necessary. Additional information can be obtained by tagging both heavy hadrons in the event, e.g. in a $D^{\star}\mu$ correlation analysis (see Section 6.2).

The muon impact parameter is only one of several possibilities to exploit the beauty lifetime signature. A possible extension is a multiple impact parameter analysis using the δ information from more than one track in the event and is in principle not restricted to a particular decay channel (see [93]). Alternatively, the decay length can be measured directly if the secondary event vertex is reconstructed explicitly. This approach has been followed up in [94].

The combination of several different decay channels and observables should form the basis of an inclusive beauty tag which, in combination with the high–statistics data to come, will make it possible to fully exploit the valuable testing ground provided by beauty production processes at HERA.

Appendix A

Fit Method

The crucial step in the beauty cross section measurement is the determination of the relative signal contribution f_b to the selected H1 event sample from a fit to the shape of beauty–sensitive observable spectra. A brief overview on the fit method is given below, the details are described in [67].

The analysis observable spectra are not available in analytic form but as binned distributions. Using m different (e.g. MC)[1] event samples to model all relevant signal and background processes, a prediction n_i^P for the number of muon candidates contributing to bin i can be obtained via

$$n_i^P = \sum_{j=1}^{m} f_j A_{ji} \quad , \tag{A.1}$$

which is to be compared to the corresponding number n_i^D seen in the H1 data. Here, the f_j are the proportions of the different sources in the data, which are to be determined. A_{ji} denotes the number of muon candidates expected from the MC source j in bin i. For each source and bin, the corresponding number a_{ji} of MC muon candidates actually observed is related to A_{ji} by a binomial distribution, which can be taken as a Poisson distribution if A_{ji} is much smaller than the total size N_j of the MC sample. This will in general be true if the number of bins r is sufficiently large.

The combined probability to observe particular spectra $\{n_i^D\}$ and $\{a_{ij}\}$ in data and MC respectively can be described by a likelihood $\mathfrak{L}$ with

$$\ln \mathfrak{L} = \sum_{i=1}^{r} \left[n_i^D \ln \left(n_i^P \right) - n_i^P \right] + \sum_{i=1}^{r} \sum_{j=1}^{m} \left[a_{ji} \ln \left(A_{ji} \right) - A_{ji} \right] \quad . \tag{A.2}$$

By maximising this likelihood estimates for the f_j are obtained. In particular, this provides the signal fraction f_b and thus the basis for the cross section determination. The procedure necessarily includes estimating the A_{ji}, which, however, are not further used in the measurement. The (statistical) errors of the fit results are estimated by varying

[1]Although in the following those samples are denoted *MC* sources in order to simplify the wording, obviously also suitably selected real data events could be used for this purpose.

the f_j around the solution and determining the maximum variation for which $\ln \mathfrak{L}$ stays within given bounds depending on the required confidence level.

The first term in equation (A.2) corresponds to a determination of the f_j in a standard *binned maximum likelihood fit* considering fluctuations in the n_i^D but neglecting fluctuations in the a_{ji}. Even for large MC samples, however, the number of entries in a particular bin might well be small. For this reason the second term is added accounting for the finite MC statistics.

It can be shown that, at local maxima or minima of $\ln \mathfrak{L}$, exchanging the observed MC distribution $\{a_{ij}\}$ for a given source j with the corresponding estimates $\{A_{ij}\}$ might change the shape of the distribution but not the total number of muon candidates from that source:

$$\sum_{i=1}^{r} A_{ij} = \sum_{i=1}^{r} a_{ij} \quad \forall j. \tag{A.3}$$

There is also an automatic normalisation to the total number N^D of muon candidates in the real data, i. e.

$$N^D = \sum_{i=1}^{r} n_i^D = \sum_{i=1}^{r} \sum_{j=1}^{m} f_j n_i^P = \sum_{j=1}^{m} f_j N_j \quad . \tag{A.4}$$

Further details of the fit method and its technical implementation can be found in [67], including special considerations for bins with no contribution from a MC source and the treatment of weighted distributions.

Appendix B

Fake Muon Background

In this appendix some aspects related to the background to semi–muonic beauty decays arising from the mis–identification or decay of light hadrons (*fake muons*, see section 3.2) are discussed.

B.1 Classification

For the following discussion it is useful to distinguish two classes of light hadron background to the muon sample:

- **In–flight decays of light mesons**
  Most of the hadronic activity in positron–proton final states is due to long–lived but unstable light hadrons. The largest contribution arises from charged pions and kaons, both decaying predominantly into a muon and a muon neutrino. As in both cases the decay length $c\tau$ is large (≈ 7.8 m and ≈ 3.7 m for $\pi^{\pm}$ and $K^{\pm}$ respectively), these mesons are typically absorbed within the calorimeter before decaying. There is, however, a non–vanishing probability for a decay within the inner detector region resulting in a detectable final state muon with the associated neutrino escaping unseen. The meson and muon trajectories might be reconstructed as a single drift chamber track and, therefore, interpreted as a muon coming from the ep interaction point. In general, the pions and kaons are accompanied by further hadronic activity such that the decay muon is likely to be found within a reconstructed jet. Thus, such *in–flight decays* of light mesons give rise to a possibly non–negligible background to semi–muonic beauty decays.

- **Punch–through**
  In general, central final state hadrons are stopped in the LArC with their energy fully contained within the calorimeter volume. In some cases, however, energy leaks out of the calorimeter and reaches the instrumented iron. This effect is referred to as *punch–through*. Punch–through background arises, for example, from muonic kaon and pion decays within the calorimeter. Further contributions are expected due to high–energy hadrons showering late or close to an acceptance hole. As the particle interaction with the detector material is a probabilistic process, there is is also a non–zero probability for a hadron to traverse the inner detector region, including the calorimeter, without any strong interaction.[1] Although filter algorithms are applied during the muon reconstruction procedure to reject hadronic showers, it is not always possible to distinguish those from single penetrating muons.

B.2 Modelling Approaches

For this analysis two approaches to model the fake muon background are considered:

(I) By simulating the detector response for Monte Carlo generated events, fake muons can be selected explicitly. As the mis–identification probability for individual hadrons is small, large MC event samples are needed. The MC has to be fully inclusive in the sense that no process present in the H1 data and relevant for the analysis is missing in the simulation. Also, one has to be sure that all relevant hadronic final state properties are modelled correctly. For example, as the mis–identification probability is not independent of the hadron type, the hadron composition of the final state, in particular the kaon–to–pion ratio, is of relevance.

(II) The second approach is based on the assumption that the probability $\mathcal{P}_{\rm fake}$ to see a fake muon can be described on a single track basis and factorises into three parts:

$$\mathcal{P}_{\rm fake} = \sum_h \mathcal{P}_{\rm kin}(p_t, \theta) \otimes \mathcal{P}^h_{\rm type}(p_t, \theta) \otimes \mathcal{P}^h_{\rm misID}(p_t, \theta) \quad . \tag{B.1}$$

$\mathcal{P}_{\rm kin}(p_t, \theta)$ is the probability to reconstruct a charged particle track with transverse momentum p_t and polar angle θ, which with probability $\mathcal{P}^h_{\rm type}$ is due to a hadron of type h. $\mathcal{P}^h_{\rm misID}(p_t, \theta)$ parametrises the probability that a hadron h with a given p_t and θ is mis–identified as a muon. In order to obtain $\mathcal{P}^h_{\rm misID}(p_t, \theta)$, again a MC simulation has to be used. In contrast to method (I), however, for which the simulation of full event topologies is needed, this can be done on a single track basis. Taking also $\mathcal{P}^h_{\rm type}(p_t, \theta)$ from MC, inclusive track samples selected from the H1 data can be used to obtain $\mathcal{P}_{\rm kin}(p_t, \theta)$ and thus to model the fake muon background. This approach has been used in the first measurement of open beauty production at HERA [50]. A detailed description can be found in [51].

[1] These processes are sometimes referred to as *sail–through* background.

In order to implement and test the two methods, three different event samples are needed:

- `MC_fake`: The fake modelling approach (I) is realised by applying the γp signal selection to an inclusive, high–statistics PYTHIA MC event sample. Here, all identified muons fulfilling the selection cuts described in Chapter 4 are taken into account except for muons from charm and beauty decays.
- `DATA_track`: Repeating the selection for tagged photoproduction events in data but omitting the muon identification and rejecting explicitly events containing identified muons results in a light flavour–dominated sample which can be used to model the fake muon background following approach (II). Here, the hadron composition $\mathcal{P}^h_{\text{type}}$ as well as the parametrised mis–identification probabilities $\mathcal{P}^h_{\text{misID}}(p_t, \theta)$ are adopted from [50, 51].
- `MC_track`: This sample is constructed in the same way as the `DATA_track` sample, except for using PYTHIA MC instead of H1 data.

Figure B.1 illustrates schematically how these samples can be used in two different ways to model a not directly available '`DATA_fake`' sample containing the fake muons entering the H1 signal data set. Translating the distributions obtained from a '`track`' sample into the corresponding '`fake`' spectra relies on the validity of the ansatz (B.1), which in the following will be referred to as *fake probability factorisation*. Moving from a '`MC`' sample to the corresponding '`DATA`' sample rests on a Monte Carlo simulation describing all relevant aspects of the H1 data. If both assumptions are correct, the shape of the analysis observable spectra are the same for all samples.

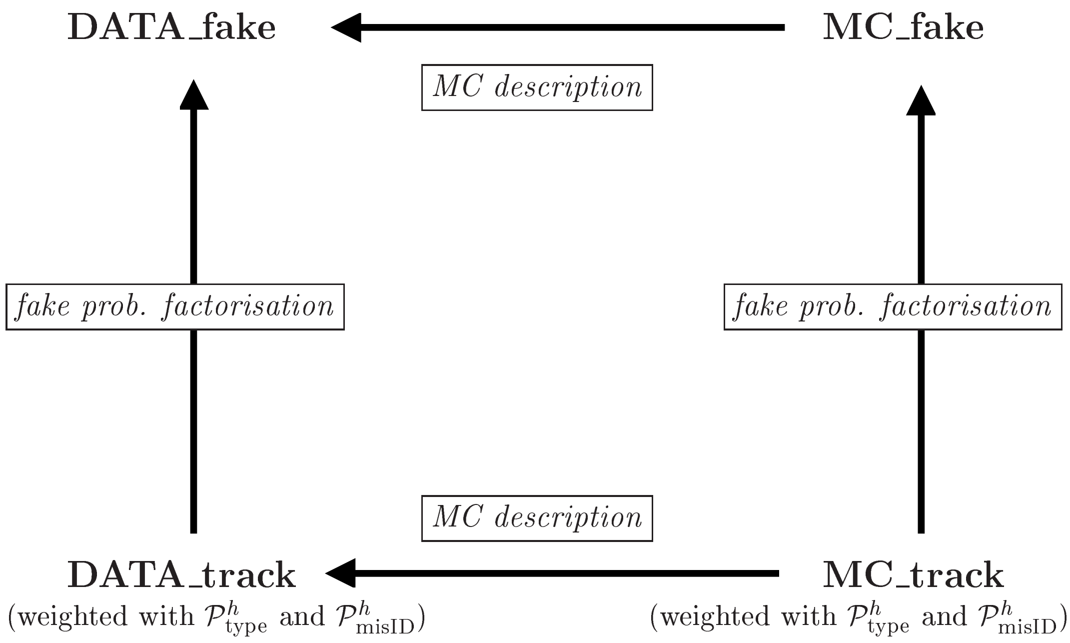

Figure B.1: *Schematic overview of data samples and fake modelling approaches.*

B.3 Test of the Fake Probability Factorisation Ansatz

The validity of the factorisation ansatz (B.1) can be checked by comparing the observable distributions obtained from the MC_fake and MC_track samples. The result is shown in Figure B.2. The agreement is far from perfect. The impact parameter distribution is broader for fake muons compared to tracks and the p_t^{rel} distribution is shifted to higher values. These differences turn out to be non–negligible for the analysis. Exchanging the MC_fake sample for the MC_track sample in the extraction of the beauty contribution yields a relative decrease of f_b by 21%, 13% and 22% using both observables, δ and p_t^{rel} respectively.[2]

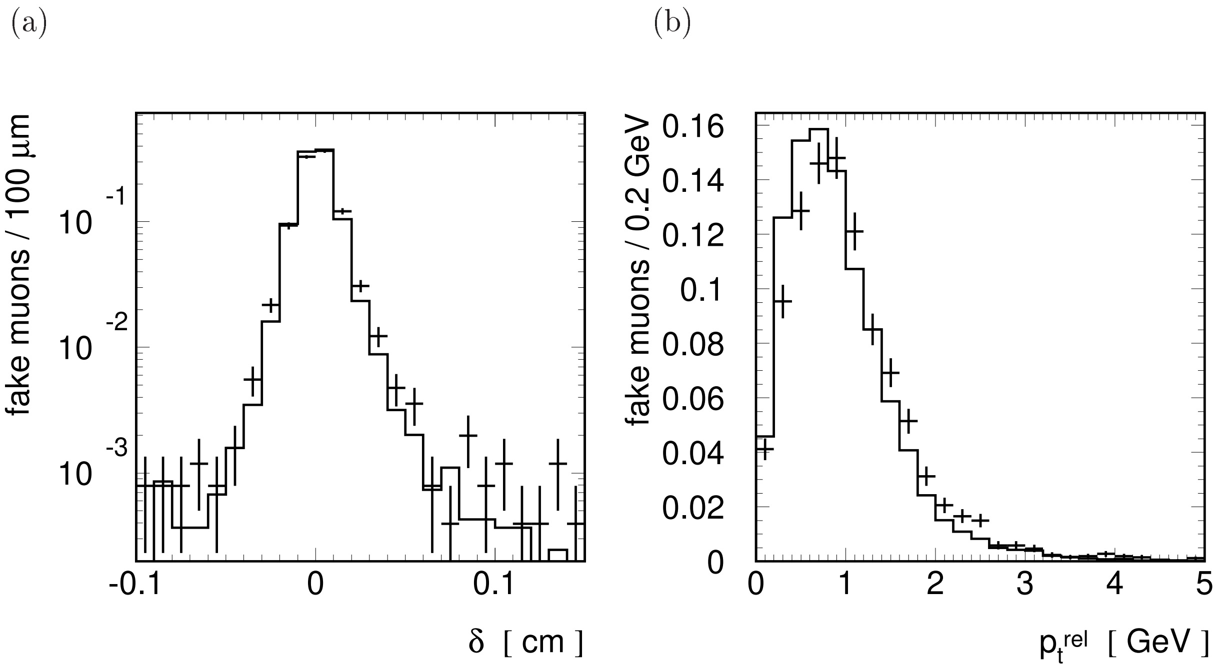

Figure B.2: *Reconstructed distributions of (a) the impact parameter δ and (b) p_t^{rel} as obtained from the* MC_fake *sample (points) and the* MC_track *sample (histograms).*

In order to further study these discrepancies, it is instructive to divide the MC_fake sample into two parts, one of them containing only in–flight decays and the other only punch–through hadrons. Comparing the observable spectra obtained from these subsamples separately to the corresponding MC_track distributions (cf. Figure B.3)[3] reveals significant deviations in the δ–shape for the in–flight decays and in the p_t^{rel} shape for fake μ from other sources, while for the other observable agreement within errors is found in both cases. Thus, the two classes of fake μ background seem to violate the fake probability factorisation in different ways and are hence discussed separately in the following.

[2]Here, the fake muon contribution is fixed to 45% in all cases.

[3]It should be noted that the parametrised mis–identification probabilities have not been determined separately for in–flight decays and punch–through particles and, therefore, MC_track samples corresponding to these two background classes are, strictly speaking, not available. Using the inclusive MC_track sample instead for the following comparisons, however, does not affect the (qualitative) conclusions.

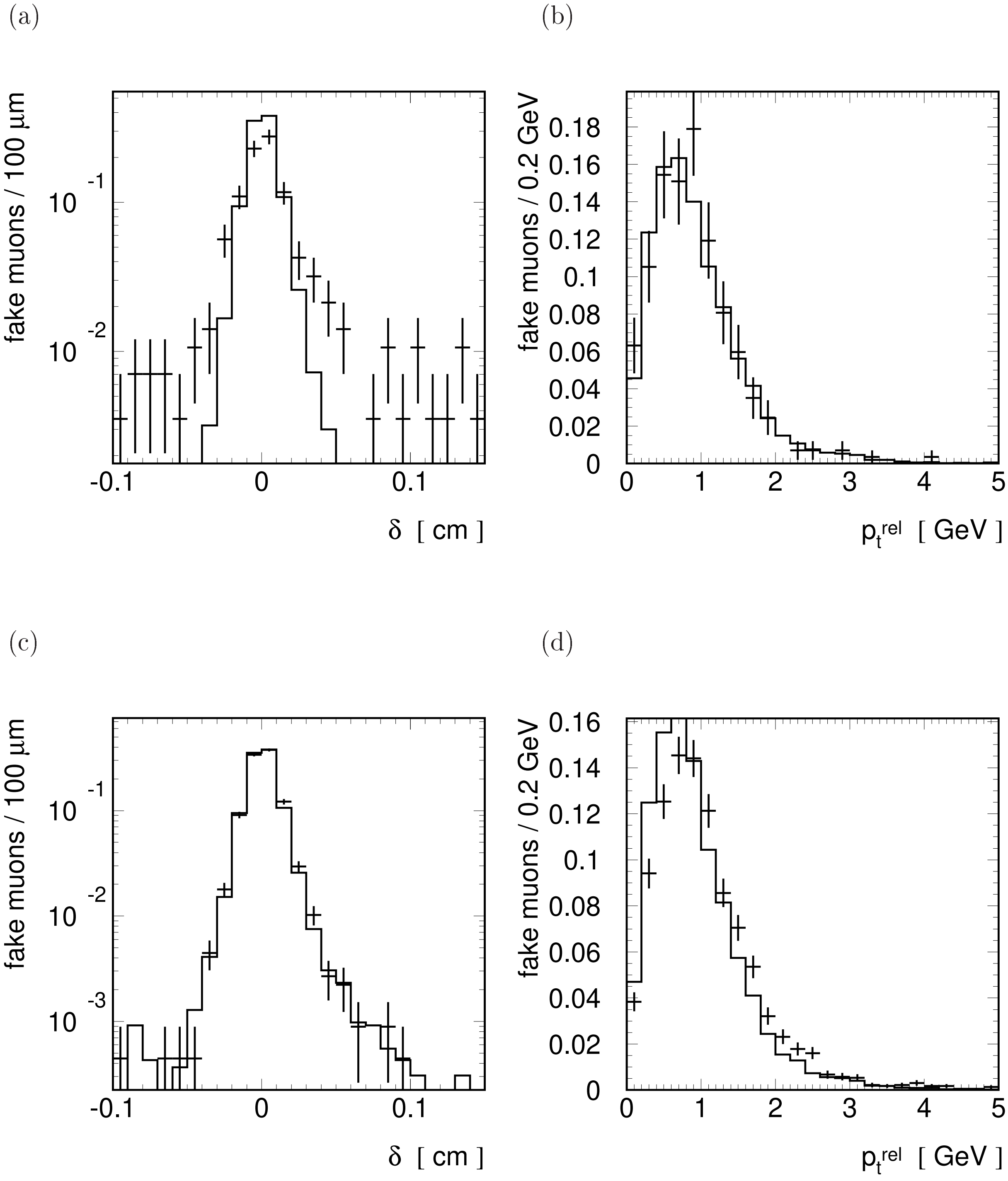

Figure B.3: *Top: Reconstructed distributions of (a) the impact parameter δ and (b) p_t^{rel} as obtained from the* `MC_fake` *in–flight decay sample (points) and the* `MC_track` *sample (histograms). Bottom: Reconstructed distributions of (c) the impact parameter δ and (d) p_t^{rel} as obtained from the* `MC_fake` *punch–through sample (points) and the* `MC_track` *sample (histograms).*

In–flight Decays

In order to understand and possibly solve the problems of using the fake probability factorisation ansatz in the impact parameter analysis, muons originating from kaon and pion decays are selected from the `MC_fake` sample.

As shown in Figure B.4, large impact parameters arise almost exclusively from kaon decays at radii smaller than the radius of the inner CST layer of 5.7 cm. In the muon candidate selection procedure associated CST hits in both layers are required. For decay radii larger than 5.7 cm, the inner CST hit does not arise from the muon itself but from its parent meson and will in general only be used successfully in the track fit if the decay angle is small. As the parent particle is produced at the primary event vertex and, therefore, has no intrinsic δ, large muon impact parameter values are not likely in these cases. For pion decays, the small pion mass restricts the phase space to small decay angles forcing also the muon impact parameter to be small.

The δ spectrum from kaon decays at small radii is governed by the decay kinematics. A factorisation ansatz using mis–identification probabilities depending exclusively on the transverse momentum and the polar angle of the resulting muon is, therefore, expected to fail here.

It should also be noted that in–flight decays at very small radii constitute a background which is irreducible in the sense that a further suppression by refining the muon reconstruction and selection procedure is impossible. There is no detector information on the parent meson and the signal in the instrumented iron is indeed produced by a muon rather than a mis–identified hadron.

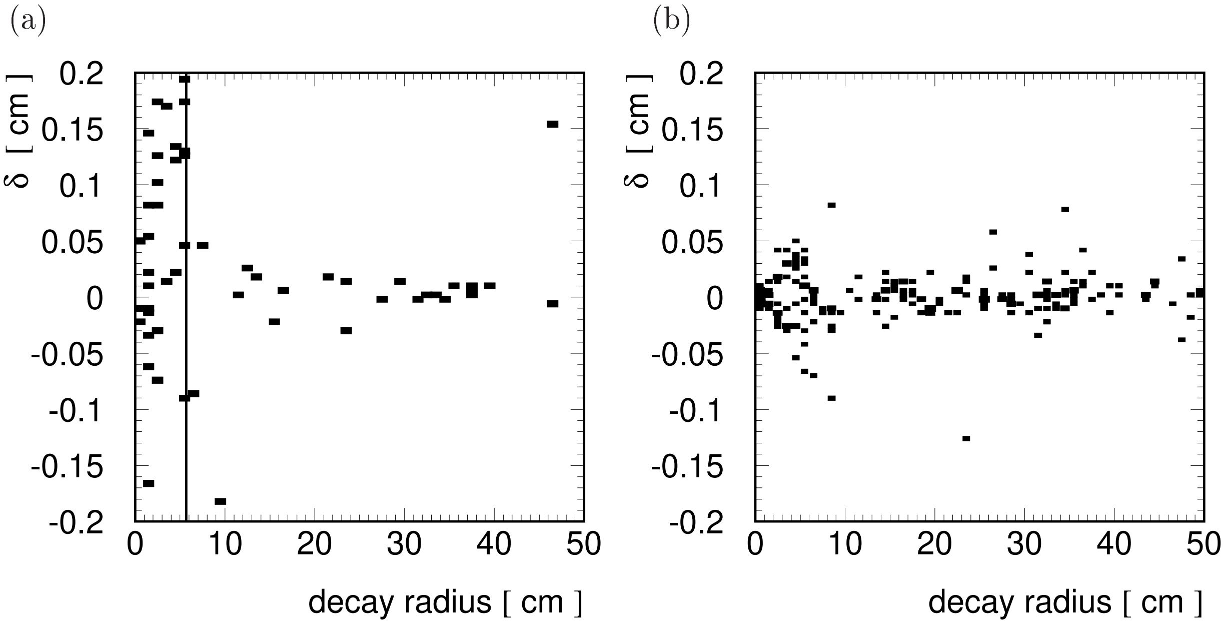

Figure B.4: *Reconstructed muon impact parameter as a function of the true decay radius of the parent meson for in–flight decays of (a) kaons and (b) pions, which have been selected from the* `MC_fake` *sample. The vertical line in (a) marks the radius of the inner CST layer.*

Punch–Through Background

A promising starting point for an explanation of the differences in the p_t^{rel} spectra obtained from the `MC_track` and the `MC_fake` samples respectively is the energy flow around the muon candidate. Inclusive hadrons and fake muons are expected to behave differently in the calorimeter. Ideally, this should be irrelevant, because the calorimeter energy associated with the candidate track is not used in the final state reconstruction, see Section 4.5.1. Imperfections in the reconstruction, in particular in the cluster–track association, however, could lead to systematic differences in the reconstructed energy flow in the vicinity of hadron and fake muon candidate tracks respectively, which might well translate into different p_t^{rel} spectra.

Figure B.5 compares the calorimeter energy deposition behind the candidate track for the `MC_track` sample, punch–through particles and semi–muonic beauty decays. All electromagnetic (hadronic) calorimeter clusters within a maximum distance of $R_c^{had} =$ 25 cm ($R_c^{elm} = 50$ cm) from the track are taken into account. Energy depositions which have been associated to other tracks in the cluster–track combination procedure are not considered. The left–hand–side plots show the summed cluster energies E_{calo} divided by the track energy E_{track}. On the right hand side, energy–weighted distributions of the track–cluster distance are shown, which in the following are denoted *calorimeter energy flow* plots.

As expected, the relative energy deposition is considerably larger for inclusive hadrons compared to muons with mean E_{calo}/E_{track} values of about 90% and 50% respectively. For punch–through particles, the shape of the E_{calo}/E_{track} distribution is closer to muonic beauty decays than to inclusive tracks. This is also not surprising because a significant fraction of the particle energy is needed to produce a signal in the muon system. In the standard final state reconstruction procedure, clusters behind the track are rejected until the total rejected energy exceeds E_{track} (see Section 4.5.1). As can be seen from the E_{calo}/E_{track} distributions, this cut–off condition is most relevant for the inclusive hadron sample.

The calorimeter energy flow plots for the beauty MC and the `MC_track` sample look similar. In both cases the associated clusters are typically found within distances of about 10 cm or less with a flattish tail towards higher values. The shape of the calorimeter energy flow distributions obtained from the simulated punch–through background and the `MC_track` sample differ considerably, the tail at cluster–track distances $\gtrsim 10$ cm being more pronounced for punch–through particles.

Assuming only the clusters within distances of about 10 cm to be directly related to the candidate track, the calorimeter depositions in the tail of the calorimeter energy flow distributions reflect the underlying event but are, nevertheless, associated to the candidate in the final state reconstruction and thus rejected. This artificially decreases the energy flow around the candidate leading to an over–estimation of p_t^{rel}. As compared to inclusive hadrons the tail in the calorimeter energy flow is more pronounced for punch–through particles, the punch–through p_t^{rel} spectrum is expected to be harder. This is indeed observed, see Figure B.2(d).

(a)

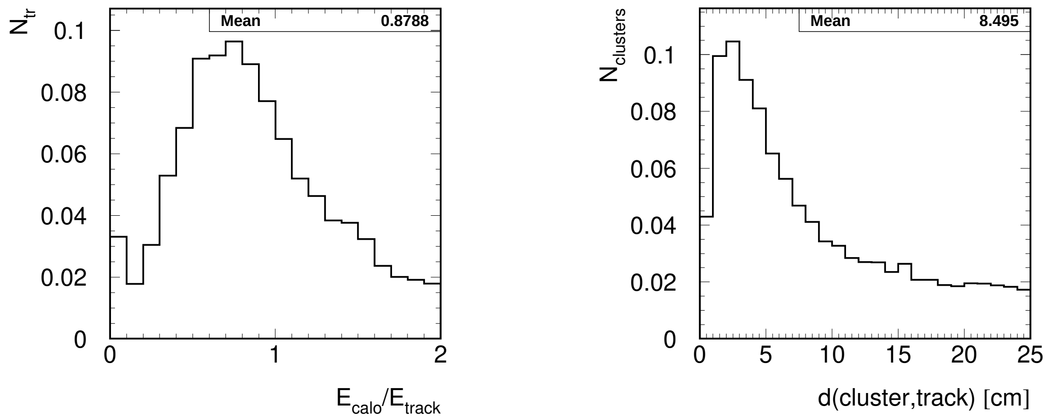

(b)

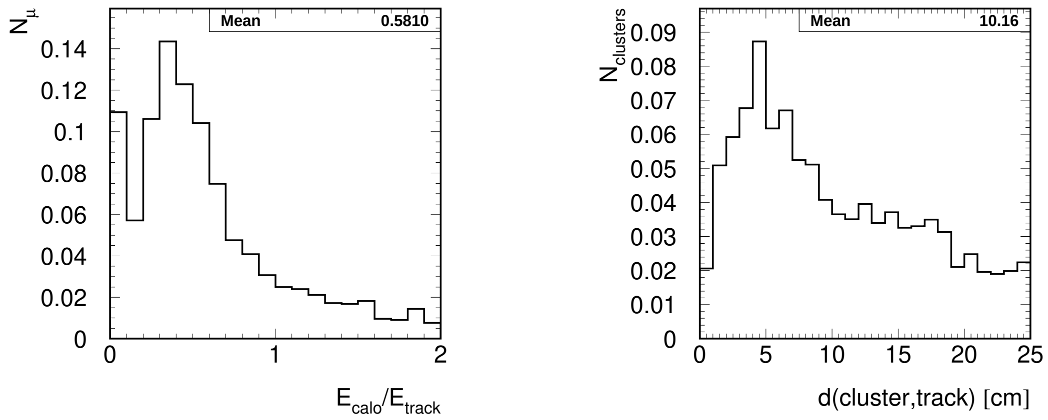

(c)

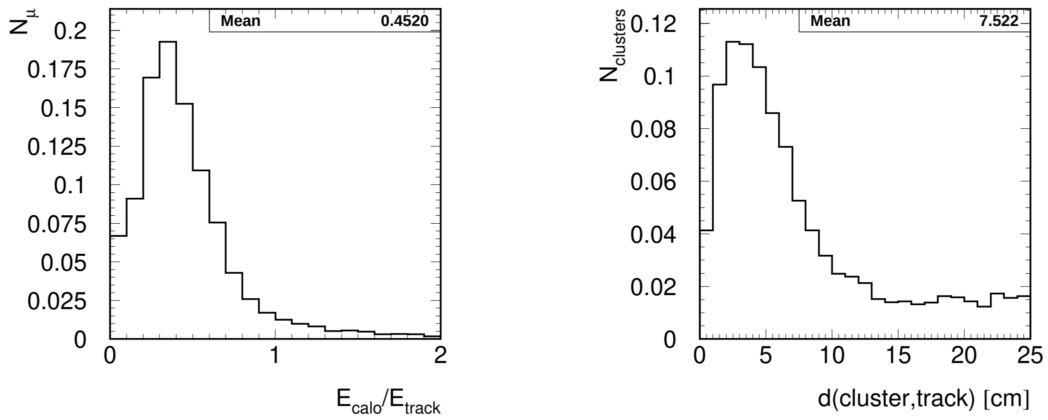

Figure B.5: *Calorimeter energy depositions behind a muon candidate tracks for different MC samples: (a) inclusive tracks, (b) fake muons (punch–through hadrons) and (c) semi–muonic beauty decays. The left–hand side plots show the summed cluster energy E_{calo} behind the track divided by the track energy E_{track}. On the right–hand side, energy–weighted distributions of the track–cluster distance are shown. All distribution are normalised to unit area.*

Also without a fundamental understanding of the effect, the situation can be improved based on the above findings by changing the candidate track–cluster combination procedure in the following way:

- Following the above interpretation of the calorimeter energy flow plots, the cone radii R_c^{elm} and R_c^{had} are reduced to 12.5 cm and 25 cm respectively.
- All clusters within the cone are rejected, i. e. E_{track} is no longer used as an upper limit to the total rejected calorimeter energy. This turns out to further reduce the sensitivity of $p_t^{\rm rel}$ to the underlying event.

The $p_t^{\rm rel}$ spectra for punch–through particles and inclusive tracks after these changes are given in Figure B.6, showing an improved agreement compared to Figure B.3(d).

After re–including the in–flight decays, exchanging the `MC_fake` sample for the `MC_track` sample changes the $p_t^{\rm rel}$ fit result for f_b by 10%, i. e. the different treatment of the calorimeter cluster reduces this systematic effect to less than half its original size.

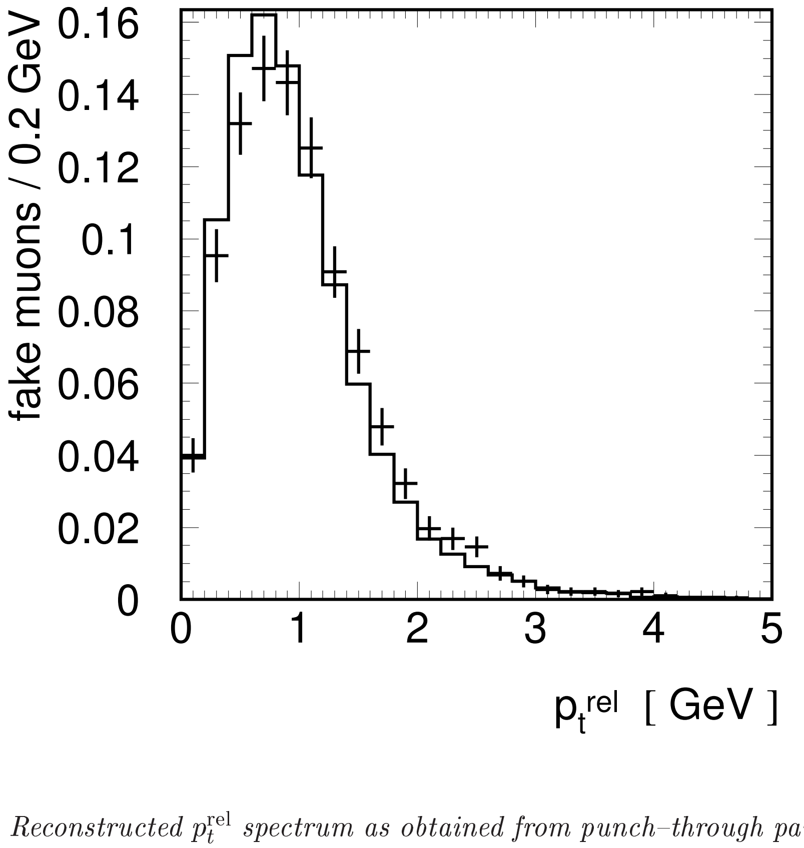

Figure B.6: *Reconstructed $p_t^{\rm rel}$ spectrum as obtained from punch–through particles (points) and the* `MC_track` *sample (histograms) after changing the candidate–cluster combination procedure.*

B.4 Comparison of Data and MC

Figure B.7 shows a comparison of the analysis observable spectra for the `DATA_track` and the `MC_track` samples. Again, regions of poorer agreement are found in both cases. The MC prediction tends to be below the data in the tails of the impact parameter distribution and the MC p_t^{rel} spectrum is slightly shifted towards lower values.

The effect on the measurement is, however, found to be moderate. Exchanging the `DATA_track` sample for the `MC_track` sample in the δ, p_t^{rel} and combined fit results in a relative change of the beauty contribution by -3%, -8% and -6% respectively.[4]

(a) (b)

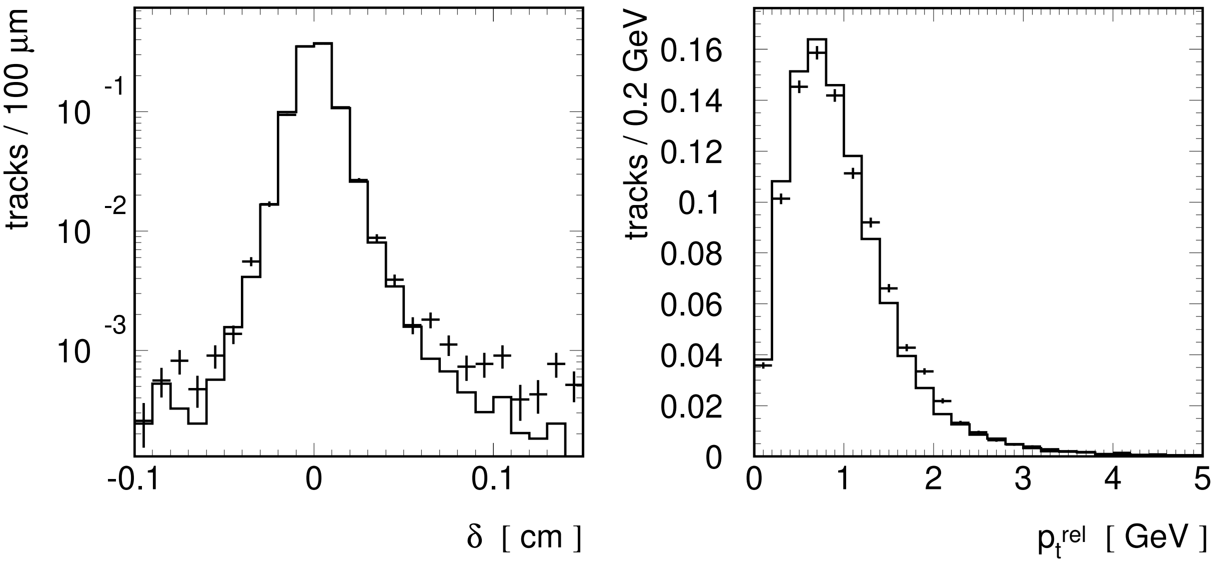

Figure B.7: *Reconstructed distributions of (a) the impact parameter δ and (b) p_t^{rel} as obtained from the* `DATA_track` *sample (points) and the* `MC_track` *sample (histograms).*

B.5 Summary and Conclusion

Using approach (II), i. e. the fake probability factorisation ansatz (B.1), to model the fake muon background results in a systematic overestimation of the beauty contribution f_b to the signal data. In the δ analysis, this effect is due to in–flight decays of light mesons and can be eliminated by modelling this background explicitly using MC simulation. For p_t^{rel}, no such specific physics process could be identified and the source of the problem is more likely to be found in the final state reconstruction procedure. By changing the treatment of calorimetric energy depositions close to the candidate track, the systematic effect on f_b can be reduced to an acceptable but still non–negligible level.

[4]Again, a fixed fake contribution 45% is used here.

In this analysis, the first modelling approach (I), where fake muons are selected from an inclusive, high–statistics MC event sample, is chosen as the default procedure for the following reasons:

- In–flight decays of light mesons have a significant impact on the δ analysis. For this background the fake probability factorisation ansatz is not valid and, therefore, MC simulation has to be used.
- In order to use approach (II) for punch–through particles only, an exclusive mis–identification probability parametrisation for this type of background (excluding in–flight decays) is needed, which is presently not available.
- For the purposes of this analysis, the spectra of the measurement observables from inclusive tracks in H1 data and MC simulation agree sufficiently well.

It should be noted that also in the chosen approach the modelling of the fake muon background introduces non–negligible systematic effects which have to be considered in the evaluation of the uncertainty on the measured cross section.

List of Figures

List of Tables

Bibliography

[1] S.L. Glashow, *Partial Symmetries of Weak Interactions*, Nucl. Phys. 22 (1961) 579.

[2] S. Weinberg, *A Model of Leptons*, Phys. Rev. Lett. 19 (1967) 1264.

[3] A. Salam, *Weak and Electromagnetic Interactions*, in: N. Svartholm (ed.), *Elementary Particle Theory*, Proceedings of the Nobel Symposium, Lerum 1968, Stockholm (1968) 367.

[4] K. Hagiwara et al. (Particle Data Group), *Review of Particle Physics*, Phys. Rev. D 66 (2002) 010001.

[5] R.K. Ellis, W.J. Stirling and B.R. Webber, *QCD and Collider Physics*, Cambridge University Press, Cambridge (1996).

[6] F. Jacquet, A. Blondel, *Detectors for Charged Current Events*, in: U. Amaldi (ed.), *ECFA Study of an ep Facility for Europe*, Proceedings, DESY, Hamburg (1979) 377.

[7] M. Born, *Optik*, Springer, Berlin (1933).

[8] R.P. Feynman, *Very High Energy Collisions of Hadrons*, Phys. Rev. Lett. 23 (1969) 1415.

[9] J.D. Bjorken, *Asymptotic Sum Rules at Infinite Momentum*, Phys. Rev. 179 (1969) 1547.

[10] V.N. Gribov, L.N. Lipatov, *Deep Inelastic ep Scattering in Perturbation Theory*, Sov. J. Nucl. Phys. 15 (1972) 438;
V.N. Gribov, L.N. Lipatov, *e^+e^-–Pair Annihilation and Deep Inelastic ep Scattering in Perturbation Theory*, Sov. J. Nucl. Phys. 15 (1972) 675.

[11] G. Altarelli, G. Paresi, *Asymptotic Freedom in Parton Language*, Nucl. Phys. B 126 (1977) 298.

[12] Y.L. Dokshitzer, *Calculation of the Structure Functions of Deep Inelastic Scattering and e^+e^- Annihilation by Perturbation Theory in Quantum Chromodynamics*, Sov. Phys. JETP 46 (1977) 641.

[13] M. Ciafaloni, *Coherence Effects in Initial Jets at Small Q^2*, Nucl. Phys. B 296 (1988) 49.

[14] S. Catani, F. Fiorani and G. Marchesini, *QCD Coherence in Initial State Radiation*, Phys. Lett. B 234 (1990) 339;
S. Catani, F. Fiorani and G. Marchesini, *Small x Behavior of Initial State Radiation in Perturbative QCD*, Nucl. Phys. B 336 (1990) 18.

[15] G. Marchesini, *QCD Coherence in the Structure Function and Associated Distributions at Small x*, Nucl. Phys. B 445 (1995) 49.

[16] V.V. Sudakov, *Vertex Parts at Very High-Energies in Quantum Electrodynamics*, Sov. Phys. JETP 3 (1956) 65.

[17] B. Reisert, *Elektron–Proton–Streuung bei hohen Impulsüberträgen am H1-Experiment*, Dissertation LMU München (2000).

[18] C.F. von Weizsäcker, *Ausstrahlung bei Stößen sehr schneller Elektronen*, Z. Phys. 88 (1934) 612.

[19] E.J. Williams, *Nature of the High–Energy Particles of Penetrating Radiation and Status of Ionisation and Radiation Formulae*, Phys. Rev. 45 (1934) 729.

[20] S. Frixione, M.L. Mangano, P. Nason and G. Ridolfi, *Improving the Weizsacker-Williams Approximation in Electron–Proton Collisions*, Phys. Lett. B 319 (1993) 339.

[21] J.J. Sakurai, *Vector Meson Dominance and High–Energy Electron–Proton Inelastic Scattering*, Phys. Rev. Lett. 22 (1969) 981.

[22] J.J. Sakurai and D. Schildknecht, *Generalized Vector Dominance and Inelastic Electron–Proton Scattering*, Phys. Lett. B 40 (1972) 121.

[23] T.H. Bauer, R.D. Spital, D.R. Yennie and F.M. Pipkin, *The Hadronic Properties of the Photon in High–Energy Interactions*, Rev. Mod. Phys. 50 (1978) 261; Erratum ibid. 51 (1979) 407.

[24] S. Catani, Y.L. Dokshitzer, M.H. Seymour and B.R. Webber, *Longitudinally Invariant K(t) Clustering Algorithms for Hadron–Hadron Collisions*, Nucl. Phys. B 406 (1993) 187.

[25] L.M. Jones and H.W. Wyld, *Charmed Particle Production By Photon Gluon Fusion*, Phys. Rev. D 17 (1978) 759.

[26] G. Kramer, *Open Heavy Flavour Photoproduction at NLO*, in: G. Grindhammer, B.A. Kniehl, G. Kramer (eds.), *New Trends in HERA Physics*, Proceedings of the Workshop, Tegernsee 1999, Springer, Berlin (2000) 275.

[27] C. Peterson, D. Schlatter, I. Schmitt, and P.M. Zerwas, *Scaling Violations in Inclusive e^+e^- Annihilation Spectra*, Phys. Rev. D 27 (1983) 105.

[28] P. Nason and C. Oleari, *A Phenomenological Study of Heavy–Quark Fragmentation Functions in e^+e^- Annihilation*, Nucl. Phys. B 565 (2000) 245.

[29] B. Andersson, G. Gustafson, G. Ingelman and T. Sjöstrand, *Parton Fragmentation and String Dynamics*, Phys. Rept. 97 (1983) 31.

[30] S. Frixione, M.L. Mangano, P. Nason and G. Ridolfi, *Heavy Quark Correlations in Photon–Hadron Collisions*, Nucl. Phys. B 412 (1994) 225.

[31] S. Frixione, M.L. Mangano, P. Nason, and G. Ridolfi, *Total Cross Sections for Heavy Flavor Production at HERA*, Phys. Lett. B 348 (1995) 633.

[32] B.W. Harris and J. Smith, *Heavy Quark Correlations in Deep Inelastic Electroproduction*, Nucl. Phys. B 452 (1995) 109;
B.W. Harris and J. Smith, *Invariant Mass Distributions for Heavy Quark–Anti-Quark Pairs in Deep Inelastic Electroproduction*, Phys. Lett. B 353 (1995) 535.

[33] B.W. Harris and J. Smith, *Charm Quark and $D^{*\pm}$ Cross Sections in Deeply Inelastic Scattering at HERA*, Phys. Rev. D 57 (1998) 2806.

[34] T. Sjöstrand, *High–Energy Physics Event Generation with PYTHIA 5.7 and JETSET 7.4*, Comput. Phys. Commun. 82 (1994) 74.

[35] G. Ingelman, J. Rathsman and G.A. Schuler, *AROMA 2.2 - A Monte Carlo Generator for Heavy Flavour Events in ep Collisions*, Comput. Phys. Commun. 101 (1997) 135.

[36] G.A. Schuler and H. Spiesberger, *DJANGO: The Interface for the Event Generators HERACLES and LEPTO,* in: W. Buchmüller, G. Ingelmann (eds.), *Physics at HERA*, Proceedings of the Workshop, Vol. 3, DESY, Hamburg (1992) 1419.

[37] H. Jung, *Hard Diffractive Scattering in High–Energy ep Collisions and the Monte Carlo Generator RAPGAP*, Comput. Phys. Commun. 86 (1995) 147.

[38] H. Jung, *The CCFM Monte Carlo Generator CASCADE*,
Comput. Phys. Commun. 143 (2002) 100.

[39] I. Abt et al. [H1 Collaboration], *The H1 Detector at HERA*, Nucl. Instr. and Meth. A386 (1997) 310 and 348.

[40] W. Erdmann, *Untersuchung der Photoproduktion von $D^\star$–Mesonen am ep–Speichering HERA*, Dissertation ETH Zürich (1996).

[41] J. Steinhart, *Die Messung des totalen $c\bar{c}$–Photoproduktions–Wirkungsquerschnittes durch die Rekonstruktion von Λ_c–Baryonen unter Verwendung der verbesserten dE/dx–Teilchenidentifikation am H1 Experiment bei HERA*, Dissertation Univ. Hamburg (1999).

[42] D. Pitzl et al., *The H1 Silicon Vertex Detector*, Nucl. Instr. and Meth. A454 (2000) 334.

[43] J. Gassner, *Messung der Ortsauflösung des H1–Siliziumvertexdetektors*, Diploma, ETH Zürich (1996).

[44] M. Kausch–Blecken von Schmeling, *The Silicon Microvertex Detector of the H1 Experiment: Readout, Event Reconstruction, and Studies on Heavy Quark Decays*, Dissertation Univ. Hamburg (1998).

[45] C. Kleinwort and U.-P. Krüger, *Track Reconstruction in the Iron*, H1 Internal Software Note 35–08/92 (1992).

[46] D. Müller, *A Measurement of the Gluon Density in the Proton Based on Charm Production at HERA*, Dissertation Univ. Zürich (1998).

[47] V. Blobel, *BOS and Related Packages*, in: R. Brun, P. Kunz and P. Palazzi (eds.), *Data Structures for Particle Physics Experiments: Evolution or Revolution*, Proceedings of the 14. Workshop of the INFN Eloisatron Project, Erice 1990, World Scientific, Singapore (1991) 1;
V. Blobel, *The BOS System*, H1 internal document (2001).

[48] R. Brun et al., *GEANT3 Users Guide*, CERN–DD/EE/84–1, 1987.

[49] I. Negri, *A Minimal Comprehensive Set of Muon Background Topological Finders for High p_t Physics Analyses*, Internal Note H1–10/96–498.

[50] C. Adloff et al. [H1 Collaboration], *Measurement of Open Beauty Production at HERA*, Phys. Lett. B 467 (1999) 156; Erratum ibid. B 518 (2001) 331.

[51] U. Langenegger, *A Measurement of the Beauty and Charm Production Cross Sections at the ep Collider HERA*, Dissertation ETH Zürich (1998).

[52] T. Kuhr, *Messung des Wirkungsquerschnittes von b–Quark–Produktion in tiefunelastischer Elektron–Proton–Streuung bei H1*, Dissertation Univ. Hamburg (2002).

[53] L. West, *Heavy Flavour Working Group Track, Muon and Electron Selection Code*, H1 internal document (1996),
https://www-h1.desy.de/h1/iww/iwork/ihq/sw-doc/track_doc30000.ps.gz.

[54] K. Krüger, *Photoproduction of J/ψ Mesons at Medium and Low Elasticities at HERA*, Dissertation Univ. Hamburg (2001).

[55] O. Behrendt, *Improved Track Linking between Central Jet Chamber and Central Silicon Tracker*, DESY summer student project report, unpublished (1999).

[56] H1 Collaboration, *Measurement of Inclusive D–Meson Production in Deep Inelastic Scattering at HERA*, ICHEP2002, Amsterdam, contributed paper 1015 (2002).

[57] J. Gassner, *A Measurement of D–Meson Production at HERA by Decay Vertex Identification*, Dissertation ETH Zürich (2002).

[58] O. Behnke and J. Kroseberg, *CSTLIN: Combined CJC–CST Track Fit*, H1 internal document, in preparation.

[59] Tracking Task Force, *Calibration and Alignment for Precision Tracking*, http://www-h1.desy.de/h1det/tracker/tracktaskforce/welcome_ttf1.html.

[60] T. Kuhr and M. Kausch–Blecken von Schmeling, *CSPRIM: Primary Vertex Determination using CST Measurements*, H1 internal document (2000).

[61] J. Marks et al., *A Software Package to Cope with the Hadronic Final State*, H1 internal document (2001), https://www-h1.desy.de/iwork/iescale/hfs/hfs.html.

[62] C. Adloff et al. [H1 Collaboration], *Diffractive Dissociation in Photoproduction at HERA*, Z. Phys. C 74 (1997) 221.

[63] S. Hengstmann, *A Measurement of Diffractive Charm Production at HERA*, Dissertation Univ. Zürich (2000).

[64] C. Adloff et al. [H1 Collaboration], *Measurement of D^* Meson Cross Sections at HERA and Determination of the Gluon Density in the Proton*, Nucl. Phys. B 545 (1999) 21.

[65] J. Marks et al., *QESCAT: e Identification Software in H1PHAN*, H1 internal document (1996), https://www-h1.desy.de/iwork/iescale/qescat/qescat.html.

[66] V.V. Arkadov, *Measurement of the Deep–Inelastic ep Scattering Cross Section using the Backward Silicon tracker at the H1 Detector at HERA*, Dissertation Humboldt–Univ. Berlin (2000).

[67] R. Barlow and C. Beeston, *Fitting Using Finite Monte Carlo Samples*, Comput. Phys. Commun. 77 (1993) 219.

[68] N. Gogitidze and S. Levonian, *An offline Luminosity Determination fot the 1995 e^+p Data*, Internal Note H1–02/96–471.

[69] F. Abe et al. [CDF Collaboration], *The Topology of Three Jet Events in $\bar{p}p$ Collisions at $\sqrt{s} = 1.8$ TeV*, Phys. Rev. D 45 (1992) 1448.

[70] J.E. Huth et al., *Toward a Standardization of Jet Definitions*, in: E.L. Berger (ed.), *1990 DPF Summer Study on High Energy Physics, Research Directions for the Decade (Snowmass '90)*, World Scientific (1992) 134.

[71] J. Kurzhöfer, *The QJCONE jet algorithm and its implementation in H1PHAN*, Internal Note H1–09/94–375.

[72] D. Buskulic et al. [ALEPH Collaboration], *Measurement of the Effective b Quark Fragmentation Function at the Z Resonance*, Phys. Lett. B 357 (1995) 699.

[73] A.D. Martin, W.J. Stirling and R.G. Roberts, *Pinning Down the Glue in the Proton*, Phys. Lett. B 354 (1995) 155.

[74] M. Gluck, E. Reya and A. Vogt, *Photonic Parton Distributions*, Phys. Rev. D 46 (1992) 1973.

[75] M. Gluck, E. Reya and A. Vogt, *Dynamical Parton Distributions Revisited*, Eur. Phys. J. C5 (1998) 461.

[76] J. Breitweg et al. [ZEUS Collaboration], *Measurement of Open Beauty Production in Photoproduction at HERA*, Eur. Phys. J. C18 (2001) 625.

[77] ZEUS Collaboration, *Measurement of Beauty Photoproduction at HERA*, ICHEP2002, Amsterdam, contributed paper 785 (2002).

[78] ZEUS Collaboration, *Measurement of Beauty Production in Deep Inelastic Scattering at HERA*, ICHEP2002, Amsterdam, contributed paper 783 (2002).

[79] J. Wagner [on behalf of the H1 Collaboration], *$D^\star$-Muon Correlations and D–Meson Production in DIS*, presented at DIS2002, Cracow (2002);
H1 Collaboration, *$D^\star\mu$ Correlations in ep Scattering at HERA*, ICHEP2002, Amsterdam, contributed paper 1016 (2002).

[80] ZEUS Collaboration, *Measurement of Open Beauty Production at HERA Using a D^*+Muon Tag*, ICHEP2002, Amsterdam, contributed paper 784 (2002).

[81] F. Abe et al. [CDF Collaboration], *Inclusive J/ψ, $\psi(2S)$ and b Quark Production in $\bar{p}p$ Collisions at* $\sqrt{s} = 1.8$ TeV, Phys. Rev. Lett. 69 (1992) 3704.

[82] F. Abe et al. [CDF Collaboration], *J/ψ, $\psi(2S)$ Production in $\bar{p}p$ Collisions at* $\sqrt{s} = 1.8$ TeV, Phys. Rev. Lett. 79 (1997) 572.

[83] S. Abachi et al. [D0 Collaboration], *Inclusive μ and B Quark Production Cross Sections in $p\bar{p}$ Collisions at* $\sqrt{s} = 1.8$ TeV, Phys. Rev. Lett. 74 (1995) 3548.

[84] S. Abachi et al. [D0 Collaboration], *J/ψ Production in $p\bar{p}$ Collisions at* $\sqrt{s} = 1.8$ TeV, Phys. Lett. B 370 (1996) 239.

[85] M. Acciarri et al. [L3 Collaboration], *Measurements of the Cross Sections for Open Charm and Beauty Production in $\gamma\gamma$ Collisions at* $\sqrt{s} = 189$ GeV–202 GeV, Phys. Lett. B 503 (2001) 10.

[86] A. Csilling [on behalf of the OPAL Collaboration], *Charm and Bottom Production in Two-Photon Collisions with OPAL*, in: A.J. Finch (ed.), *PHOTON 2000*, Proceedings of the International Workshop on Structure and Interactions Of The Photon, Ambleside 2000, Melville, New York (2000) 276.

[87] M. Cacciari and P. Nason, *Is There a Significant Excess in Bottom Hadroproduction at the Tevatron?*, Phys. Rev. Lett. 89 (2002) 122003.

[88] H. Jung, *Heavy Quark Production at HERA in k(t) Factorization Supplemented with CCFM Evolution*, hep–ph/0110345.

[89] E.L. Berger, B.W. Harris, D.E. Kaplan, Z. Sullivan, T.M. Tait and C.E. Wagner, *Low Energy Supersymmetry and the Tevatron Bottom–Quark Cross Section*, Phys. Rev. Lett. 86 (2001) 4231.

[90] M. Hilgers, *Untersuchung von Beauty-Ereignissen bei HERA anhand ihres myonischen Zerfalls und strahlenharte Ausleseelektronik fuer den Silizium-Vertex-Detektor des H1-Experiments*, Dissertation ETH Zürich (2001).

[91] H1 Collaboration, *Measurement of the Beauty Production Cross Section at HERA Using Lifetime Information*, ICHEP2000, Osaka, contributed paper 979 (2000).

[92] T. Sloan [on behalf of the H1 Collaboration], *Heavy Flavour Production at HERA*, presented at the XXXVIth Rencontres de Moriond, Moriond (2001); H1 Collaboration, *Beauty Production in Deep Inelastic ep Scattering*, EPS2001, Budapest, contributed paper 807 (2001).

[93] I. Foresti, *PhD thesis work*, Univ. Zürich, in progress.

[94] S. Lüders, *A Measurement of the Beauty Production Cross Section via* $B \to J/\psi X$ *at HERA*, Dissertation ETH Zürich (2001).

Acknowledgments

I thank Professor Peter Truöl for giving me the opportunity to work in his group and the freedom to pursue the analysis of my choice.

I am much indebted to Felix Sefkow for his strong and continuous support throughout my time as a Ph.D. student. He never failed to give good advice whenever it was needed. The analysis was performed in close collaboration with Olaf Behnke. Working with him was a most enjoyable experience for me and invaluable for the success of the measurement. Markus Kausch–Blecken von Schmeling's Ph.D. work first introduced me to the impact parameter method and provided me with a useful starting point.

During this work I got help and advice from many H1 colleagues, in particular from other members of the Heavy Flavour Working Group, who are too numerous to mention but whose contributions are hereby gratefully acknowledged. Thanks also to everyone whose comments helped to improve the presentation of the measurement in this thesis, especially to Duncan Brown and Florian Keil for carefully proof–reading earlier versions of the manuscript.

I also wish to thank David Müller and Martin zur Nedden who shared with me their knowledge of (and enthusiasm for) the H1 zVtx trigger, CIP and CIZ. It was a pleasure to have Stefan Hengstmann working with me on keeping these detector components up and running. Here, also the support from the hardware experts at the University of Zurich and at DESY was indispensable.

I extend my gratitude to all the colleagues at Hamburg and Zurich who made work at both places enjoyable and worthwhile.

Finally, I would like to thank my family and friends 'outside physics' for their support and for helping me trying to keep things in perspective even in times of absorbing work.

This work has been supported by the Swiss National Science Foundation.

Curriculum Vitae

Personalien:

Name:	Kroseberg
Vorname:	Jürgen
Geboren:	29. September 1971 in Ratingen, Deutschland
Staatsangehörigkeit:	deutsch

Bildungsgang:

1978 – 1982	Adolf–Reichwein–Grundschule in Hilden, Deutschland
1982 – 1991	Dietrich–Bonhoeffer–Gymnasium in Hilden
1991	Abitur
1992 – 1998	Studium der Physik an der Westfälischen Wilhelms-Universität in Münster, Deutschland; Wahlfächer: Angewandte Physik, Kern- und Teilchenphysik
1994	Vordiplom
1995 – 1996	Studienaufenthalt (*non–graduating student*) an der University of Edinburgh, GB/Schottland
1997 – 1998	Diplomarbeit unter der Leitung von Prof. Dr. D. Frekers; Titel: Untersuchungen zum experimentellen Nachweis von W–Produktion mit dem H1–Detektor am Beispiel des Zerfalls $W \to \mu\nu_\mu$
1998	Hochschulabschluss (Diplomphysiker), WWU Münster
1998 – 2002	Wissenschaftliche Mitarbeit am Physik–Institut der Universität Zürich beim H1–Experiment am *Deutschen Elektronen–Synchrotron* (DESY) in Hamburg; Dissertation bei Prof. Dr. P. Truöl; Titel: A Measurement of Beauty Production in High–Energy Positron–Proton Scattering